



UNIVERSIDADE D  
COIMBRA

David José Gaspar Marques

**NEGATIVE ION MOBILITY MEASUREMENT  
IN GASES OF INTEREST FOR NITPCs**

**Thesis submitted to the University of Coimbra in fulfillment of the  
requirements for the Master's Degree in Engineering Physics under the  
scientific supervision of Ph.D. André Filipe Ventura Cortez and Ph.D.  
Professor Filipa Isabel Gouveia de Melo Borges Belo Soares.**

October of 2020



UNIVERSITY OF COIMBRA

MASTER OF SCIENCE THESIS

INTEGRATED MASTER'S IN ENGINEERING PHYSICS

---

# Negative ion mobility measurement in gases of interest for NITPCs

---



LABORATÓRIO DE INSTRUMENTAÇÃO  
E FÍSICA EXPERIMENTAL DE PARTÍCULAS  
*partículas e tecnologia*

AUTHOR:

DAVID JOSÉ GASPAR MARQUES

SUPERVISORS:

PROF. FILIPA ISABEL BORGES BELO SOARES  
(UNIVERSITY OF COIMBRA)

DR. ANDRÉ FILIPE VENTURA CORTEZ  
(GRAN SASSO SCIENCE INSTITUTE)

October of 2020





Esta cópia da tese é fornecida na condição de que quem a consulta reconhece que os direitos de autor são pertença do autor da tese e que nenhuma citação ou informação obtida a partir dela pode ser publicada sem a referência apropriada.

This copy of the thesis has been supplied on condition that anyone who consults it is understood to recognise that its copyright rests with its author and that no quotation from the thesis and no information derived from it may be published without proper acknowledgement.

The research reported in this thesis was performed with financial support of the following institutions/programs:

- Scientific initiation scholarship granted through the project "Participation in the RD51 Collaboration" (CERN/FIS/INS/0025/2017) with the duration of 4 months, starting on the 4<sup>th</sup> of April, 2019.
- Scientific initiation scholarship granted through the project "Participation in the RD51 Collaboration" (CERN/FIS/INS/0025/2017) with the duration of 5 months, starting on the 18<sup>th</sup> of May, 2020.





À minha avó...



”The thing that doesn’t fit  
is the thing that’s the most  
interesting: the part that doesn’t go  
according to what you expected.”

Richard P. Feynman



## Acknowledgements

Firstly, I would like to express my deep gratitude to the LIP Gaseous Detectors group for accepting me as a student 4 years ago and for guiding me since then. Being able to work with such experienced researchers and professors allowed me to open my horizons within the research world and strengthen my expertise in the field of applied physics and gaseous detectors. Especially, I thank professors Filomena Santos and Filipa Borges for closely following my progress with utter interest and for all the motivation and suggestions provided throughout the years. To both professors, thank you for helping me growing as a person and as a researcher. I will carry my experience at LIP throughout all my life.

Secondly, I want to thank professor Elisabetta Baracchini for taking part in my formation during my last university year by supervising my work in my internship at GSSI and by helping in the writing and correction of this thesis.

To the LIP workshops, I thank for the availability shown regarding the filling of the gas bottles and the manufacture of essential components for this thesis.

To the LIBPhys group, namely professor Joaquim and Ph.D. student Pedro Costa e Silva, my full gratitude for the time spent in the process of making a CsI deposit on the GEM and expertise shared while doing so.

I also want to express my sincere gratitude to Dr. André Cortez. Starting as my supervisor, you quickly became one of the most important persons of my academic experience, guiding me in some of the most decisive decisions of my life, restlessly passing me all your knowledge on gaseous detectors and the research world, teaching me how to approach certain matters and people and, last but not least, for being an ever-present friend that I will never forget. Thank you for everything, André.

A great thanks also to the friends that accompanied me during these 5 years, Afonso Marques, João Brito, João Jordão and Gabriel Salgado, for all the lunches and philosophical theories discussed. A special thanks to my dear friend Miguel Gonçalves for being by my side and being part of my life since I can remember. I hope these friendships continue throughout our lives, no matter where we are.

I also thank to my parents, José and Isabel, and sister, Rita, for allowing and pushing me to follow my dreams and hopes, for being always there, and for teaching me how to be a better person.

Lastly, I thank to everyone that, by one way or another, influenced my academic and personal life making me the person I am today.





## Abstract

Gaseous detectors are widely used in many fields ranging from high energy physics to rare-event searches due to their high tracking and particle identification capabilities. To further improve these features, several efforts are being carried in order to improve or develop new position-sensitive electron amplification and readout systems. In gaseous detectors that resort to electron drift to track and measure the energy of ionizing particles, one of the biggest constraints is the electron diffusion. This is especially relevant in large volume gas radiation detectors. To surpass such limitation, Negative Ion Time Projection Chambers (NITPCs) were developed. Instead of making use of electrons, these detectors explore negative ions as charge carriers, exploiting their much smaller diffusion, when compared to electrons. With the recent discovery of minority charge carriers, these chambers are also expected to be able to determine the absolute position of the ionizing event along the drift direction by analysing the drift time differences between the several minority ion species created from the same electronegative gas.

To support the development of NITPCs, a new chamber capable of measuring the ion mobility of both positive and negative ions was developed at LIP: the Dual-Polarity Ion Drift Chamber (DP-IDC). The DP-IDC is an ion drift chamber that includes a Gas Electron Multiplier (GEM) with a CsI deposit in the middle of the chamber, two double grids in each endcap and a series of electric field rings that create a uniform electric field throughout the drift region. The GEM, in this setup, has a very low gain as its main objective is to create ions while the electrons drift through its holes. With a UV-lamp on the top, it is possible to produce photoelectrons near the GEM when the CsI photocathode (deposited on the top electrode of the GEM) is hit by the UV photons, while also providing a trigger for the measurement. Knowing the drift distance and after analysing the time of arrival spectra, it is possible to determine the ions' velocity and to calculate their reduced mobility for different gases, pressures, temperatures, amongst other parameters.

The first prototype of the DP-IDC has shown several important limitations. Thus, to improve this detector, several modifications were implemented, namely the development of a new central component capable of both supporting/holding the GEM and ensuring a uniform electric field through the whole drift region. After this modification, the chamber was tested with several preliminary studies. These allowed to better understand the influence of different variables in the drift spectra. Such studies were focused on the influence of the pressure and the presence of ion clusters and gas impurities on the mobilities obtained. Together with these, the influence of the electric field in the GEM's holes was also carefully studied. The voltage applied on the GEM proved to strongly affect the type of ions created within the chamber. Other studies concerning, for instance, the lamp induced signal were also carried to better understand the signal formation with this experimental setup.

In this work, the results obtained with pure  $\text{SF}_6$  and  $\text{SF}_6$  based mixtures are presented.  $\text{SF}_6$  was chosen as it is assumed to be a strong candidate for the next generation of NITPCs. The preference for  $\text{SF}_6$  relies on the fact that two distinct ion species are expected to

be present ( $\text{SF}_6^-$  and  $\text{SF}_5^-$ ) allowing therefore for the determination of the absolute  $z$  position of an ionization event in NITPCs. The mobility of  $\text{SF}_6$  ions ( $\text{SF}_6^-$ ,  $\text{SF}_5^-$  and, possibly,  $\text{SF}_4^-$ ) have been measured in this work for different pressures (up to 30 Torr) and different reduced electric fields (up to 40 Td). The mobilities obtained have shown to be in accordance with most of the published data. Similar studies with  $\text{SF}_6\text{-CF}_4$  and  $\text{SF}_6\text{-N}_2$  were also carried and the mobilities obtained are also within the expected, both comparing with the literature and theoretical values retrieved from Blanc's law.

The identification of the different ion species created for each set of parameters as well as the ratio among themselves has proven to be attainable with the DP-IDC using  $\text{SF}_6$ . This is a key feature for the development of negative ion drift detectors (such as NITPCs). Moreover, by verifying the initial great performance of the DP-IDC, further studies can be carried regarding negative ion drift in different gas mixtures and different conditions of pressure and reduced electric field as well as studies concerning ion diffusion and the presence of ion clusters.

**Keywords:** Gaseous Detectors; Negative Ion Drift (NID); Negative Ion Time Projection Chamber (NITPC); Ion Mobility;  $\text{SF}_6$ ; Dual-Polarity Ion Drift Chamber (DP-IDC).

## Resumo

Detetores gasosos são usados em diversas áreas desde física de altas energias até buscas de eventos raros devido às suas grandes capacidades de identificação e *tracking* de partículas. Para melhorar estas capacidades, vários esforços têm vindo a ser realizados para melhorar ou desenvolver novos sistemas de amplificação e leitura sensíveis à posição. Em detetores gasosos que recorrem à deriva de eletrões para fazer *track* e medir a energia de partículas ionizantes, uma das maiores restrições é a difusão dos eletrões. Isto é especialmente relevante em detetores gasosos de grande volume. Para ultrapassar esta limitação, as Câmaras de Projeção Temporal de Iões Negativos (em inglês, *Negative Ion Time Projection Chambers*, NITPCs) foram desenvolvidas. Em vez de fazerem uso de eletrões, estes detetores usam iões negativos como portadores de carga, explorando a sua menor difusão, comparando com a dos eletrões. Com a recente descoberta de portadores de carga minoritários, é esperado que nestas câmaras seja possível determinar a posição absoluta do evento ionizante ao longo da direção de deriva, analisando as diferenças no tempo de deriva das várias espécies de iões minoritários criados a partir do mesmo gás eletronegativo.

Para apoiar o desenvolvimento de NITPCs, uma nova câmara capaz de medir a mobilidade de iões positivos e negativos foi desenvolvida no LIP: a Câmara de Deriva de Iões de Dupla-Polaridade (em inglês, *Dual-Polarity Ion Drift Chamber*, DP-IDC). A DP-IDC é uma câmara de deriva de iões que inclui um multiplicador de eletrões gasoso (em inglês, *Gas Electron Multiplier*, GEM) com um depósito de CsI (Iodeto de Césio) no centro da câmara, duas grelhas duplas em cada extremidade e um conjunto de anéis de campo elétrico que criam um campo elétrico uniforme em toda a região de deriva. O GEM, neste sistema, tem um ganho muito baixo pois o seu objetivo principal é apenas criar iões enquanto os eletrões atravessam os seus orifícios. Com uma lâmpada UV no topo, é possível produzir fotoeletrões junto do GEM quando o fotocátodo de CsI (depositado no eletrodo superior do GEM) sofre o impacto dos fotões UV, criando também o ponto temporal inicial da medição (*trigger*). Sabendo a distância de deriva e depois de analisar os espetros dos tempos de chegada, é possível determinar a velocidade dos iões e calcular a sua mobilidade reduzida para diferentes gases, pressões, temperaturas, entre outros parâmetros.

O primeiro protótipo da DP-IDC mostrou algumas limitações importantes. Por esse motivo, para melhorar este detetor, várias modificações foram implementadas, nomeadamente o desenvolvimento de um novo componente central capaz de suportar o GEM e assegurar a uniformidade do campo elétrico em toda a região de deriva. Após esta modificação, a câmara foi testada através de vários estudos preliminares. Estes permitiram uma melhor compreensão da influência de diferentes variáveis no espetro de deriva. Estes estudos focaram-se na influência da pressão e na presença de aglomerados (*clusters*) de iões e impurezas do gás nas mobilidades obtidas. Para além destes tópicos, a influência do campo elétrico nos orifícios do GEM também foi cuidadosamente estudada. Provou-se que a diferença de potencial aplicada no GEM afeta fortemente o tipo de iões criados dentro da câmara. Outros estudos focados em, por exemplo, o sinal induzido pela lâmpada foram

também realizados para que fosse possível compreender melhor o processo de formação de sinal com este sistema.

Nesta tese, são apresentados os resultados obtidos com  $\text{SF}_6$  puro e misturas baseadas em  $\text{SF}_6$ . Escolheu-se  $\text{SF}_6$  pois este é assumido como sendo um forte candidato para as próximas gerações de NITPCs. A preferência por  $\text{SF}_6$  vem do facto de que é esperada a presença de duas espécies distintas de iões ( $\text{SF}_6^-$  e  $\text{SF}_5^-$ ) o que permite a determinação da posição  $z$  absoluta de um evento ionizante em NITPCs. Nesta dissertação, a mobilidade de iões de  $\text{SF}_6$  ( $\text{SF}_6^-$ ,  $\text{SF}_5^-$  e, possivelmente,  $\text{SF}_4^-$ ) foi medida para diferentes pressões (até 30 Torr) e para diferentes campos elétricos reduzidos (até 40 Td). As mobilidades obtidas mostraram-se em acordo com a informação publicada. Estudos similares com  $\text{SF}_6\text{-CF}_4$  e  $\text{SF}_6\text{-N}_2$  também foram realizados onde as mobilidades obtidas também se encontraram dentro do esperado, comparando tanto com a literatura disponível como com os valores teóricos obtidos com a lei de Blanc.

A identificação de diferentes espécies de iões criados e o rácio entre eles, para cada conjunto de parâmetros, mostrou-se possível de realizar com a DP-IDC, usando  $\text{SF}_6$ . Isto trata-se de uma característica fundamental para o desenvolvimento de detetores de deriva de iões negativos (tais como as NITPCs). Além disso, a verificação da boa performance da DP-IDC vai permitir que estudos ligados à deriva de iões negativos em diferentes misturas gasosas e diferentes condições de pressão e campo eléctrico reduzido possam ser realizados, tão bem como estudos focados na difusão de iões e na presença de aglomerados (*clusters*) de iões.

**Palavras-chave:** Detetores Gasosos; Deriva de Iões Negativos; Câmara de Projeção Temporal de Iões Negativos; Mobilidade de Iões;  $\text{SF}_6$ ; Câmara de Deriva de Iões de Dupla-Polaridade.

# Publications

## Scientific papers:

1. D. Marques, A. Cortez, J. Escada, R. Veenhof, P. Neves, C. Conde, F. Santos and F. Borges, [Experimental ion mobility measurements in Ne-CF<sub>4</sub>](#), Journal of Instrumentation 14 (2019) P04015-P04015

## Oral communications:

1. D. Marques, M. Santos, A. Cortez, J. Escada, A. Trindade, F. Santos and F. Borges, [Ion mobility in Ne-CF<sub>4</sub> mixtures](#), RD51 Mini-week at Geneva, Switzerland, 4-6 December, 2018
2. D. Marques, M. Santos, A. Cortez, J. Escada, A. Trindade, F. Santos and F. Borges, Development of a Dual-Polarity Ion Drift Chamber, DCE2019, 3<sup>rd</sup> Doctoral Congress in Engineering at Porto, Portugal, 27-28 June, 2019
3. D. Marques, M. Santos, A. Cortez, J. Escada, A. Trindade, F. Santos and F. Borges, [Measurements with the Dual-Polarity Ion Drift Chamber \(DP-IDC\)](#), RD51 Mini-week at Geneva, Switzerland, 22-26 June, 2020



# Contents

<b>Acknowledgements</b>	<b>i</b>
<b>Abstract</b>	<b>iii</b>
<b>Resumo</b>	<b>iv</b>
<b>Publications</b>	<b>vi</b>
<b>List of Figures</b>	<b>xiii</b>
<b>List of Tables</b>	<b>xvii</b>
<b>1 Introduction</b>	<b>1</b>
1.1 Negative Ion Drift . . . . .	1
1.2 Ion mobility . . . . .	2
1.3 Thesis' overview and objectives . . . . .	3
<b>2 Scientific Review on Gaseous Detectors</b>	<b>5</b>
2.1 Ionization chambers . . . . .	6
2.2 Proportional counters . . . . .	7
2.2.1 Gas Proportional Scintillation Counter . . . . .	7
2.2.2 Proportional ionization counters . . . . .	8
2.3 Geiger-Müller tubes . . . . .	9
2.4 Gaseous detector amplification techniques . . . . .	10
2.4.1 Charge multiplication . . . . .	10
2.4.2 Single wire proportional counter . . . . .	11
2.4.3 Multiwire proportional counter . . . . .	12
2.4.4 Microstrips . . . . .	13
2.4.5 Gas electron multiplier . . . . .	14
2.4.6 Micromegas . . . . .	15
2.5 Time projection chambers . . . . .	16

2.5.1	Different TPC approaches . . . . .	17
2.5.2	Negative Ion TPCs . . . . .	17
2.6	Choice of filling gas . . . . .	18
2.6.1	Pure noble gases . . . . .	18
2.6.2	Molecular mixtures . . . . .	19
2.6.3	Electronegative gases . . . . .	19
2.7	Transport of electrons and ions in gases . . . . .	20
2.7.1	Diffusion . . . . .	20
2.7.2	Ion mobility . . . . .	21
2.7.3	Models for Ion-neutral interaction . . . . .	25
2.7.4	Negative ion drift . . . . .	26
<b>3</b>	<b>Dual-Polarity Ion Drift Chamber</b>	<b>31</b>
3.1	Detector working principle . . . . .	31
3.2	Chamber description . . . . .	33
3.2.1	Electrical system . . . . .	34
3.3	Previous limitations . . . . .	35
3.3.1	Lamp signal . . . . .	35
3.3.2	Electric field . . . . .	36
3.4	Optimizations performed . . . . .	37
3.4.1	Development of a new GEM base . . . . .	37
3.4.2	GEM characterization . . . . .	38
3.4.3	Vacuum monitoring . . . . .	42
3.5	Preparatory studies . . . . .	43
3.5.1	Lamp signal . . . . .	44
3.5.2	Evolution of the spectra with time . . . . .	46
3.5.3	Pressure study . . . . .	48
3.5.4	GEM study . . . . .	50
3.5.5	Drift distance and error bars . . . . .	54
3.5.6	Conclusions of the preparatory studies . . . . .	55
<b>4</b>	<b>Experimental results</b>	<b>57</b>
4.1	Data analysis process . . . . .	57
4.2	Ne-CF <sub>4</sub> Mixture . . . . .	59
4.3	Pure SF <sub>6</sub> . . . . .	60
4.4	SF <sub>6</sub> -CF <sub>4</sub> Mixture . . . . .	63



## CONTENTS

---

4.5	SF <sub>6</sub> -N <sub>2</sub> Mixture . . . . .	65
4.6	Discussion . . . . .	67
<b>5</b>	<b>Conclusions</b>	<b>69</b>



# List of Figures

2.1	Operation regions of gas ionization chambers as a function of the relationship between the voltage applied on the detector's electrodes and the pulse size, for $\alpha$ and $\beta$ particles and gamma radiation. The several regions are: I - recombination region; II - simple ionization region; III - proportional ionization region; IV - limited proportionality region; V - Geiger-Müller region; VI - Continuous discharge region. Retrieved from [18]. . . . .	6
2.2	Schematic of the working principle of an ionization chamber. . . . .	7
2.3	Schematic of a typical gas proportional scintillation counter: 1. grid mesh with high electron transparency; 2. grid evaporated onto the PMT; 3. outlet to gas purifier; 4. Kapton window; 5. stainless-steel enclosure; 6. Cd conversion electron source; 7. Macor insulator. Retrieved from [23]. . . . .	8
2.4	Generic schematic of a proportional counter. . . . .	9
2.5	Schematic of a Geiger-Müller tube working principle showing the several avalanches created by the UV photons released in prior avalanches. Retrieved from [25]. . . . .	10
2.6	Schematic of a single wire proportional counter. Retrieved from [32]. . . . .	12
2.7	(Left) Working principle of Multiwire proportional counters where, depending on the position of the initial ionization, specific anode wires acquire a stronger or weaker signal thus allowing the reconstruction of the interaction position, and (right) electric field in each anode wire. Retrieved from [33]. . . . .	12
2.8	(Right) Structure of a Microstrip gas detector, and (left) electric field created between its cathode and anode strips. Images retrieved from [34]. . . . .	13
2.9	(Left) Electric field in the GEM's holes and the drift and induction regions and (right) a microscopic photography of a GEM showing its holes well distributed along the surface. Retrieved from [3]. . . . .	14
2.10	Schematic of a Micromegas detector using the micromesh to amplify the signal (electrons). Retrieved from [42]. . . . .	15
2.11	Typical schematic of a Time Projection Chamber, (by O. Schäfer). . . . .	16
2.12	Van 't Hoff diagrams for clustering reactions $\text{CO}_2^+(\text{CO}_2)_{n-1} + \text{CO}_2 \rightleftharpoons \text{CO}_2^+(\text{CO}_2)_n$ . Retrieved from [55]. . . . .	24

2.13	Suggested cross sections for the formation of $\text{SF}_6^-$ by electron attachment ( $\sigma_{a,\text{SF}_6^-}$ ) and the remaining species by electron dissociative attachment ( $\sigma_{da,\text{SF}_6^-}$ ). Retrieved from [68]. . . . .	30
3.1	Schematic of the detector's working principle with its main 4 steps represented.	32
3.2	Detector's inner and outer drawings. . . . .	33
3.3	Electrical system scheme of the chamber when working by modules (upper module, in this case). $R_1 = 22\text{M}\Omega$ and $V_{\text{GEM}} = V_{\text{GD}} - V_{\text{HV}}$ . . . . .	34
3.4	Measurement of an ion's time of arrival spectrum. It is visible that the initial peak caused by the lamp is as broad as, almost, $100\text{ }\mu\text{s}$ , when the expected width was $500\text{ ns}$ . Spectrum retrieved from [69]. . . . .	36
3.5	Simulations performed to analyse the electric field inside the chamber. It is presented the (a) vertical electric field when only half of the detector is biased and (b) when it is fully biased. Retrieved from [69]. . . . .	36
3.6	Electric field polarizing (a) the whole chamber and (b) only the bottom part of the chamber and with the top part with null electric field. . . . .	38
3.7	(a) Design of the central piece used to hold the GEM and to ensure the electric field's uniformity. (b) The manufactured component. (c) GEM's electrodes separated by the bigger Kapton foil. (d) The central part fully mounted, with the Kapton excess around the plates to prevent electrical discharges. Small holes along the Teflon ring were also foreseen for this component to ease the gas flowing within the chamber. . . . .	39
3.8	Example of a $1\text{x}1\text{ cm}^2$ GEM with (left) naked eye and (right) an electronic microscope. . . . .	40
3.9	GEM's leakage current when standing alone and when mounted in the central piece. These values have a reading error of 2 %. . . . .	40
3.10	Schematic of a thermal deposition. The <i>boat</i> , by the flowing of a strong electric current, is heated to a temperature where the materials melt and, consequently, evaporate. The materials then condensate and form a thin film deposit on the surface that they hit. Image from [75]. . . . .	41
3.11	Spectra of the lamp signal obtained when using either the (a) top or (b) bottom part of the detector. . . . .	44
3.12	Two generic spectra of an ions' time of arrival signal using the upper (for positive ions) and bottom (for negative ions) parts of the detector. . . . .	45
3.13	Two spectra of negative ions' time of arrival signals using pure $\text{SF}_6$ at two different pressures when these pressures were either the first or the last measurement of the run while, respectively, filling or evacuating the chamber. The grey series has a transparency factor so that the coincidence is more visible. . . . .	47

3.14	Two spectra of negative ions' time of arrival signals using the mixture $\text{SF}_6:\text{N}_2$ in the ratio 10:90 at 10 Torr and at different reduced electric fields when these values were either the first or the last measurement of the run. The grey series has a transparency factor so that the coincidence is more visible. . . . .	47
3.15	Spectra of negative ions' time of arrival signals using pure $\text{SF}_6$ at 20 Torr. The different series represent several signals taken at different instants (mm:ss) without evacuating the chamber and with $t = 0$ being the moment when the detector's filling was complete. . . . .	48
3.16	Time of arrival spectra obtained for (a) different pressures and (b) three specific pressures where a secondary peak (marked in red) appears. These measurements were performed within the same conditions - pure $\text{SF}_6$ and 10 Td. . . . .	49
3.17	Time of arrival spectra obtained for different voltages applied across the GEM and with 10 Torr of pure $\text{SF}_6$ at 20 Td. . . . .	50
3.18	Time of arrival spectra obtained for different voltages applied across the GEM and with 20 Torr of pure $\text{SF}_6$ at 20 Td. . . . .	51
3.19	Time of arrival spectra obtained for different voltages applied across the GEM with 20 Torr of pure $\text{SF}_6$ at 20 Td. . . . .	52
3.20	Evolution of the 3 ion peak's areas with the voltage applied on the GEM. .	52
3.21	Electron attachment and dissociative electron attachment cross sections for the formation of, respectively, $\text{SF}_6^-$ (a) and $\text{SF}_5^-$ (b), as a function of the electron's energy. Retrieved from [68]. . . . .	53
4.1	Example of the analysis performed in a raw acquired signal ( <i>Data</i> , in blue). The red line ( <i>Fits' sum</i> ) is the sum of the Gaussian fits performed (3 in this case). A good fit is achieved when the red line closely follows the blue dots. In this case, 3 Gaussian curves - corresponding to 3 different ion species - were found. . . . .	58
4.2	Reduced mobility of the positive ions observed in $\text{Ne-CF}_4$ in different ratios for 15 Td (black) and 20 Td (red) at pressure of 8 Torr, obtained with the IDC [80]. In blue, the results obtained with the DP-IDC for 10 Td and 20 Torr with the same gas. The dash lines represent the expected ions that can be formed within the mixture and their expected mobilities throughout Blanc's law. . . . .	59
4.3	Typical spectrum obtained when using pure $\text{SF}_6$ . The two main ions produced ( $\text{SF}_5^-$ and $\text{SF}_6^-$ ) are visible and identified. This spectrum was obtained at a pressure of 20 Torr and an E/N of 25 Td. . . . .	61
4.4	Ion mobility values obtained for several reduced electric fields and pressures: 6 Torr (■), 8 Torr (●) and 10 Torr (◆). The two colors (red and gray) represent the two separate time of arrival peaks identified in each spectrum and for which the ions $\text{SF}_5^-$ and $\text{SF}_6^-$ were attributed. The voltage applied on the GEM was of 22 V. . . . .	62

4.5	Ion mobility values obtained for several reduced electric fields and pressures: 20 Torr (■) and 30 Torr (●). As in figure 4.4, the two same ions ( $\text{SF}_5^-$ and $\text{SF}_6^-$ ) are represented. These values were obtained with a voltage across the GEM of 18 V. In blue, the new peak identified, possibly corresponding to $\text{SF}_4^-$ , is shown. The data for this ion was obtained using a higher voltage across the GEM (35 V). . . . .	62
4.6	Ion mobility of $\text{SF}_6^-$ obtained for several different percentages of $\text{SF}_6$ and reduced electric fields, at 20 Torr. The points (●, ■ and ▲) represent the data obtained. The dashed lines represent the data in the literature [88], with the colors corresponding to the same % $\text{SF}_6$ studied. . . . .	64
4.7	Ion mobility of $\text{SF}_6^-$ and $\text{SF}_5^-$ obtained for several different percentages of $\text{SF}_6$ at 20 Torr and a E/N of 20 Td. The points (◆ and ●) represent the data obtained. The dashed lines represent the Blanc's law prediction for the mobilities of $\text{SF}_6^-$ and $\text{SF}_5^-$ in the mixture $\text{SF}_6\text{-CF}_4$ . . . . .	64
4.8	Ion mobility of $\text{SF}_6^-$ obtained for several different percentages of $\text{SF}_6$ and reduced electric fields, at 10 Torr. The points (●, ■, ▲ and ◆) represent the data obtained. The dashed lines represent the data present in the literature [89], with the colors corresponding to the same % $\text{SF}_6$ studied. . . . .	65
4.9	Ion mobility of $\text{SF}_6^-$ and $\text{SF}_5^-$ obtained for several different percentages of $\text{SF}_6$ for 20 Td at 10 Torr. The points (◆ and ●) represent the data obtained. The dashed lines represent the Blanc's law prediction for the mobilities of $\text{SF}_6^-$ and $\text{SF}_5^-$ in the mixture $\text{SF}_6\text{-N}_2$ . . . . .	66

# List of Tables

3.1	Table of the first ion mobility values obtained with the DP-IDC. Results retrieved from <a href="#">[69]</a> . . . . .	35
4.1	Reactions involving the $\text{Ne}^+$ ion and the molecule $\text{CF}_4$ and their ionization product distribution and respective rate constants. Adapted from <a href="#">[81]</a> . . . .	60





# Chapter 1

## Introduction

Gaseous ionization detectors are radiation detector instruments used to detect the passage of ionizing particles and measure their properties. The main advantages of gaseous detectors are the tracking and particle identification capabilities through the measurement of the particle's energy deposition in the medium.

Applications of this type of detectors are related to, for instance, astrophysics, medicine imaging, nuclear physics, radiation protection, among others. Even though gaseous detectors might be out-performed by other types of detectors such as solid state detectors in particle vertexing at accelerators [1, 2], the use of a gas grants remarkable qualities to particle detectors with the most usual ones being presented and explained along this thesis.

As R&D (Research & Development) devices, gaseous detectors are also useful as they are usually easy to couple with a variety of different amplification and readout systems. Regarding this, a lot of development is being focused on position-sensitive electron amplification systems. Examples of these systems are the Gas Electron Multipliers (GEMs) [3], Micro-Mesh Gaseous Structures (Micromegas) [4], Multi-wire Proportional Chambers (MWPC) [5], among others. One specific characteristic that supports this easy connection is the fact that only gaseous detectors allow for the coverage of large areas with an adaptable geometry at a reasonable price. There is also a great variety of gases to be used allowing an optimized choice for a specific physics application.

### 1.1 Negative Ion Drift

The main constrain of position-sensitive large volume detectors is the electrons' diffusion during their drift, as the radial spread of electrons while drifting increases with the drift time, thus also increasing with the drift distance. A good solution for this issue is the use of ions as information carriers: ions offer much smaller diffusions (both transverse and longitudinal) since they are much heavier and lose their energy in collisions with the gas

molecules much faster, reaching thermal equilibrium rather quickly. With this in mind, the use of negative ions as information carriers immediately jumps in as these ions have the same charge polarity of electrons thus drifting in the same direction of electrons under an applied electric field, but at a slower velocity and suffering less diffusion due to their greater masses.

The shift from electron to negative ions drift has been gaining attention from the scientific community over the recent years. The potential application of this concept in the development of gaseous detectors, such as the so-called Negative Ion TPCs (NITPCs) introduced by C.J. Martoff [6], is being the focus of several experiments with low rate signal applications such as WIMP detection [7], neutrinoless double beta decays [8] and other fundamental studies that are focused on the general properties of these type of TPCs [9].

The use of NITPCs involves the addition of a highly electronegative dopant in the gas mixture. With this, when the ionizing particle interacts inside the detector active volume, the primary electrons released by the gas are captured by the electronegative molecules at very short distances originating negative ions. Just like electrons, these anions will drift towards the anode. Here, the electron in excess is stripped from the anion in order to start an electron avalanche (thus amplifying the signal). While drifting, anions have substantially less diffusion compared to electrons due to their much larger mass. This allows for considerable better spatial resolution on the ionization track with the main drawback being the reduced count rates achievable compared to detectors based on electron drift.

Recently, the DRIFT experiment [10] has observed the presence of several minority negative ion species in gas mixtures containing CS<sub>2</sub> and O<sub>2</sub>. Moreover, DRIFT has shown that, using these minority charge carriers, it is possible to determine the  $z$  coordinate of an ionization event in a gaseous detector [11]. This is possible by analysing the time difference between the drift time of these anions.

N. S. Phan *et al* have demonstrated that SF<sub>6</sub> is a worthwhile candidate for negative ion drift while also including the possibility of signal amplification with high gains and fiducialization through the presence of minority charge carriers [12]. Accounting for the easy access of SF<sub>6</sub> and the fact that this is a non-toxic and non-flammable gas compared to others gases used for negative ion drift (such as CS<sub>2</sub> and O<sub>2</sub> at DRIFT), SF<sub>6</sub> was chosen as object of study for this thesis.

## 1.2 Ion mobility

The measurement of ion mobilities in different gas mixtures has been substantially important in various scientific fields such as high energy physics with high count rates or rare event searches conducted, for example, at CERN [13] or in other international laboratories. Ion mobility spectroscopy is also present in other everyday applications such as military equipment, national security, environmental and food analysis, among others [14]. With the introduction of NITPCs, the measurement of the mobility and diffusion of negative

ions gain special relevance as these are the key attributes of NITPCs' performance.

The movement of the electrons and ions (either positive or negative) in the gas is of great importance in the detector performance namely in aspects such as the signal formation, rate capability, spatial resolution, aging, among others. For this reason, the study of the mobility of ions in their parent gases in several gases mixtures has been the subject of several studies performed at the Laboratory of Instrumentation and Experimental Particle Physics (LIP) [15], in Coimbra, Portugal. Besides this, LIP has also created a strong reputation in the field of gaseous detectors R&D. The work performed at this group allowed it to establish an involvement with several groups such as the NEXT collaboration [16] and the RD51 collaboration at CERN. At LIP, there are also precision mechanical workshops, internationally recognised as experts in the development of gas radiation detectors. This knowledge allowed, in the past, to construct flexible and practical solutions in terms of detectors used nowadays in important experiments such as the Pierre Auger Observatory [17].

Considering the great experience that this group has with positive ion transport in gases (over a decade of work and several articles published), it would only be natural, in order to provide a more detailed understanding of the charge transport properties in gases, to use all this previous knowledge and existing setup to continue the development and improvement of the Dual-Polarity Ion Drift Chamber (DP-IDC). This system was designed to measure both positive and negative ion mobilities and, eventually, other parameters such as diffusion and pressure effects thus making this detector an essential tool for the expansion of the existing knowledge on ion drift. The objective of the work carried in this thesis was to further improve the DP-IDC and test its performance with the study of different properties of negative ion drift with  $\text{SF}_6$ . The detection of different minority charge carriers originated from  $\text{SF}_6$  with this chamber and posterior measurement of their mobilities will further motivate and support studies with NITPCs and negative ion drift.

### 1.3 Thesis' overview and objectives

This thesis presents an experimental approach focused on the study and test of the Dual-Polarity Ion Drift Chamber. This work was performed at LIP at the University of Coimbra, Portugal. The excellent facilities granted at LIP along with the great scientific knowledge and experience provided by the group's researchers allowed me to perform thorough experimental studies and simulations with this chamber.

This thesis is divided in 3 chapters:

1. In **Chapter 1**, the introduction and motivation for the execution of this thesis is presented.
2. In **Chapter 2**, a scientific revision of gaseous detectors is presented, together with their working principles and major differences. The use of negative ion as the charge carriers in the gas is also explored, detailing the  $\text{SF}_6$  case, as well as the explanation of

relevant features of gas mixtures such as the ion mobility theory and which processes are behind the creation of negative ion species.

3. In **Chapter 3**, a thorough description of the DP-IDC is made along with the latest improvements implemented and preparatory studies performed to study several features of the system.
4. In **Chapter 4**, the first results of the Dual-Polarity Ion Drift Chamber with gas mixtures containing  $\text{SF}_6$  are discussed. In this chapter, the mobilities of several minority ion species obtained from  $\text{SF}_6$  are also featured.
5. In **Chapter 5**, a discussion concerning the performance of the DP-IDC is carried, together with the outcome of the several studies performed to better understand how different features of the system affect ion mobility measurements. In this chapter also features the possible future works that can be carried with the DP-IDC in the scope of negative ion drift studies.

## Chapter 2

# Scientific Review on Gaseous Detectors

When interacting with matter, particles lose their energy through different processes. In gaseous detectors, the most important processes are *excitation* and *ionization*, i.e., as a result of an interaction between an incoming particle and the gas, the medium's atoms are brought to a state of higher energy (excitation) or lose one electron therefore producing an electron-ion pair (ionization). Following this initial interaction, either the de-excitation photon or the ionized electron will further interact with the gas atoms/molecules, originating a trail of excited atoms and free electrons, commonly referred as *primary electrons*. With a suitable electric field, it is then possible to drift these primary electrons to the anode (that can be a wire rod, a grid or a plate) where they can also be amplified and then collected. From the collected signal and using an adequate readout, several characteristics such as the radiation's energy and topological signature (including the energy loss profile) can be obtained which allows to perform the particle's tracking and identification.

The suitability of a detector for a particular type of radiation (and its energy) depends on several aspects: the filling gas, the electrical field applied and the size, shape and geometry of the detector and of the amplification and readout structures.

Gaseous detectors can be categorized depending on the existence or not of amplification of the primary electrons formed by the initial particle interaction. They can also be classified depending on the methods employed to amplify the signal and to measure the total number of electrons collected [19]. Figure 2.1 shows the different established regions used to classify the operation of gaseous detectors whose readout is based on charge collection. These regions are defined by the relationship between the voltage applied on the detector's electrodes and the size of the pulse, i.e, number of electrons collected. Typically, these regions are associated to the working principle of 3 different types of gaseous radiation detectors: ionization chambers, proportional counters and Geiger-Müller tubes.

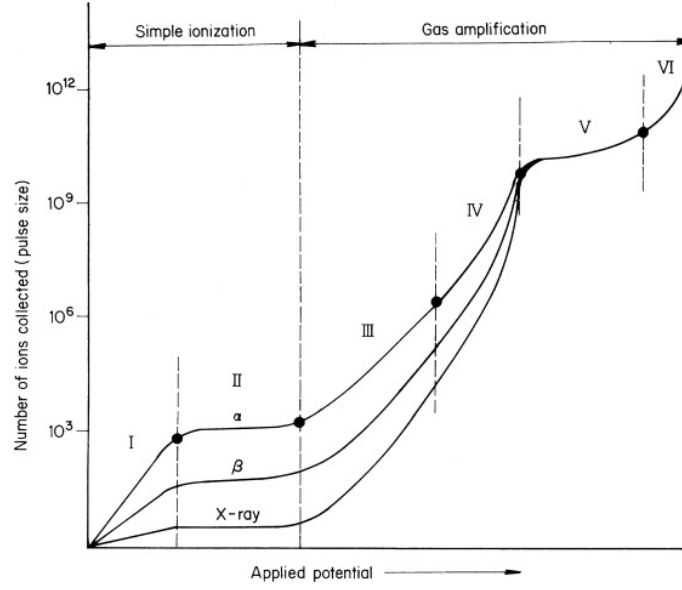


**Figure 2.1:** Operation regions of gas ionization chambers as a function of the relationship between the voltage applied on the detector’s electrodes and the pulse size, for  $\alpha$  and  $\beta$  particles and gamma radiation. The several regions are: I - recombination region; II - simple ionization region; III - proportional ionization region; IV - limited proportionality region; V - Geiger-Müller region; VI - Continuous discharge region. Retrieved from [18].

## 2.1 Ionization chambers

Ionization chambers fit in the initial region of figure 2.1, right after the recombination region (region I) where, after the ion pair is created, there is still a chance of recombination due to the very weak electric field and, as a consequence, leading to a loss in the total charge collected, even though a proportionality between the output signal and the incident radiation energy can still be observed.

In the simple ionization region, a plateau is reached meaning that the majority of the charge produced by the ionizing radiation is collected and recombination becomes negligible. Since there is no charge amplification, which inevitably introduce fluctuations, the energy resolution achieved with this type of detectors is superior to others, making ionization chambers ideal for radiation dosimetry. On the other hand, for some applications, the signal produced might not be large enough to be detected and so, to enhance the signal and reduce the noise, complicated solutions might be necessary.

Applications of ion chambers include, for example, the calibration of radioactive sources and charged particle spectroscopy. They are also useful to perform atmospheric monitoring: smoke detectors are small ionization chambers with a built-in alpha source which originates a constant ionization current. The presence of smoke particles destabilizes the ionization current which triggers an alarm [20].

A schematic of the working principle of ionization chambers is shown in figure 2.2.

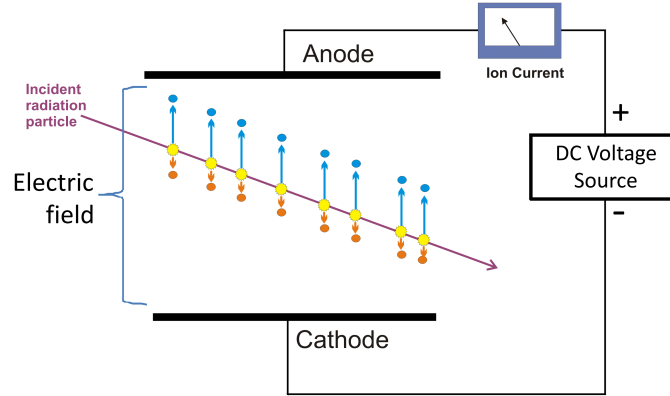


**Figure 2.2:** Schematic of the working principle of an ionization chamber.

## 2.2 Proportional counters

Further increasing the voltage applied between cathode and anode, we enter the region of proportionality. This operating region, that appears right after the simple ionization region, is used in the operation of proportional counters. At this point, amplification in charge or light takes place in different possible ways, depending mainly on the application (see section 2.4).

### 2.2.1 Gas Proportional Scintillation Counter

The Gas Proportional Scintillation Counter (GPSC) [21] is a specific type of detector that also fits in the proportionality region. This detector was introduced by Conde and Policarpio [22], that found that, by the applying an adequate electric field, it was possible to trigger the emission of light by the gas media, and that the light yield would be proportional to the number of primary electrons, and therefore to the incident radiation energy. This process would be known as *electroluminescence*. The intensity of the, also called, *secondary scintillation*, was found to proportionally increase with the electric field (light amplification).

In GPSCs, the primary electrons created by the ionizing particle are drifted until the scintillation region where they are accelerated only up to the energy where they excite the gas atoms/molecules. Following this excitation, de-excitation scintillation photons are emitted, which are then collected by a photosensor. Figure 2.3 shows the working principle of GPSCs.

While drifting in the scintillation region, where the electric field is kept above the scintillation threshold but below the ionization one, the electrons produced in the primary ionization will excite several atoms (assuming that they acquire enough energy from the electric field) and, therefore, this region works as an amplification stage. The production of secondary scintillation light has less statistical fluctuations than charge multiplication

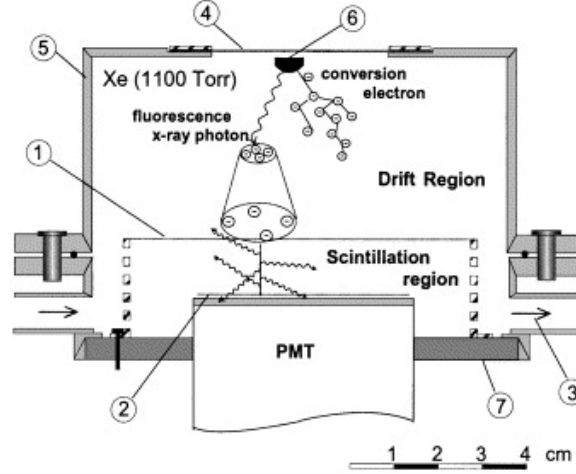


**Figure 2.3:** Schematic of a typical gas proportional scintillation counter: 1. grid mesh with high electron transparency; 2. grid evaporated onto the PMT; 3. outlet to gas purifier; 4. Kapton window; 5. stainless-steel enclosure; 6. Cd conversion electron source; 7. Macor insulator. Retrieved from [23].

since the only competing mechanism is, in the case of rare gases, elastic collisions between electrons and gas molecules. So, the energy resolution of detectors based in this amplification process have, usually, a better energy resolution than the traditional proportional ionization counters [22].

### 2.2.2 Proportional ionization counters

If the electric field in the amplification region is further increased, electrons accelerated between collisions acquire enough energy to ionize the gas atoms/molecules and the number of secondary ion pairs created is proportional to the number of primary pairs thus the name *proportional ionization counters*.

With these detectors, it is possible to record and identify particles with lower energies since the signal's amplitude can be greatly amplified by electron avalanches. The energy resolution is usually worse than in GPSCs since additional fluctuations are introduced in the amplification process. Nevertheless, these detectors are usually more robust than GPSCs since there is no need for a photosensor which, most of the times, is a fragile device.

Figure 2.4 shows a generic proportional ionization counter schematic. It is possible to see the incoming particle that ionizes the gas, the consequent drift of the electrons created and the later amplification (electron avalanche). The boundary of the avalanche region depends on the type of amplification system used (see section 2.4).

If the voltage across the detector's electrodes is further increased, a region of limited proportionality is reached: at this point, the reduced velocity of ions compared to electrons originates the accumulation of positive ions near the anode, distorting the electric field in



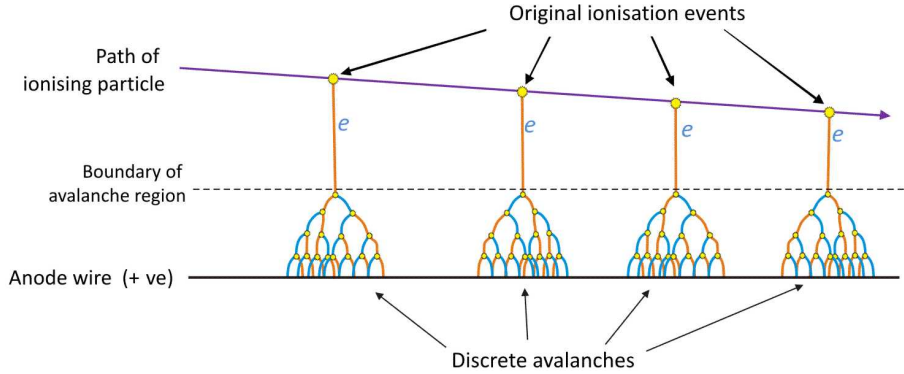


**Figure 2.4:** Generic schematic of a proportional counter.

this region and originating non-linear effects. This cloud of positive ions leads to the loss of proportionality between the output signal and the energy of the incoming particle.

Proportional counters, depending on the amplification system, can reach amplifications of  $10^4$  (up to  $10^6$ ) meaning that, for one initial primary electron,  $10^4$  electrons reach the readout system. Since electrons generate very fast pulses, this type of detectors can reach resolving times smaller than  $1 \mu\text{s}$ . Both these values (gain and resolving time) can be strongly moderated depending on the experiment's objectives by applying different voltages or designing the detector in specific ways.

## 2.3 Geiger-Müller tubes

If the voltage between the cathode and anode is further increased, the Geiger region is reached, as it can be seen in figure 2.1. This is the region exploited by Geiger-Müller tube detectors [24].

At these very strong electric fields, the charge multiplication is very high and the high energy de-excitation photons emitted during the relaxation process of the gas atoms/molecules can exponentially trigger additional avalanches. These processes are shown in figure 2.5.

In the Geiger region, the total amount of ion pairs created has no proportionality with the number of primary electrons. Therefore, all primary ionization signals produce approximately the same plateau response in the detector thus excluding the possibility of identifying the incoming particle's type and energy. Only a very rough determination of the radiation type and energy can be carried out by observing shielding effects related to the incoming radiation [26].

Since a single ion pair is able to trigger a Geiger discharge, Geiger detectors have very high counting efficiencies [27]. For this reason, these detectors are used most frequently for radiation monitoring and contamination control in everyday applications [28, 29].

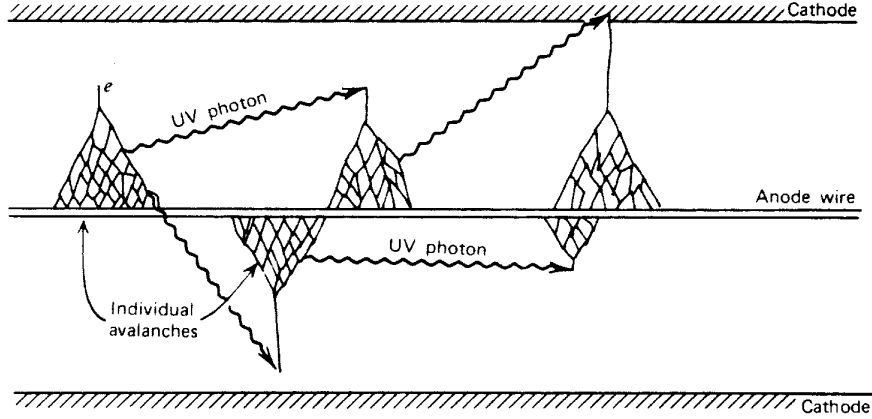


**Figure 2.5:** Schematic of a Geiger-Müller tube working principle showing the several avalanches created by the UV photons released in prior avalanches. Retrieved from [25].

## 2.4 Gaseous detector amplification techniques

The expansion and advance of several high precision mechanical techniques (such as photolithography and etching) supported the development of devices that allow the determination of the position of the spatial distribution of the ionization event created by the incident particle or radiation in the gas. Some of the most relevant ones will be discussed in this section.

### 2.4.1 Charge multiplication

When charge signals are explored, the signal acquired on the electrodes of the ionization device is formed by the induction due to the movement of free charges, electrons and ions, as they drift towards the anode and cathode, respectively.

In the most commonly used gas detectors, the amplification of the initial primary ionization electrons is performed via charge multiplication. Due to the sufficiently strong electric field in the amplification region of the detector, electrons are provided with enough energy to ionize the gas multiple times through collisions with the gas atoms thus creating secondary electron-ion pairs. These secondary electrons are also accelerated thus producing tertiary electrons and so on. This process of electron multiplication is designated *electron avalanche*.

If  $\lambda$  is the mean free path of an electron for secondary ionization, the ratio  $\alpha = 1/\lambda$ , where  $\alpha$  is the *first Townsend coefficient*, is the probability of the occurrence of a secondary ionization per unit path length. Considering  $n$  electrons travelling a distance  $dx$  through the amplification region, the number of electrons created,  $dn$ , is given by:

$$dn = n \alpha dx \quad (2.1)$$

By integrating equation 2.1, for an initial number on electrons,  $n_0$ , it is possible to obtain the total number of electrons created,  $n$ , in the path  $x$ :

$$n = n_0 e^{\alpha x} \quad (2.2)$$

Therefore, the multiplication factor,  $M$ , will be:

$$M = n/n_0 = e^{\alpha x} \quad (2.3)$$

In the case of non-uniform electric fields,  $\alpha$  is a function of the travelled distance  $x$ . Thus,  $M$  is obtained by:

$$M = \exp \left[ \int_{r_1}^{r_2} \alpha(x) dx \right] \quad (2.4)$$

Although equation 2.4 can increase without limit, the multiplication factor is physically limited to about  $M < 10^8$  or  $\alpha x < 20$  after which electrical breakdown occurs. This amplification upper-limit is known as the Raether limit [19].

The multiplication factor or *gas gain* is a fundamental characteristic in devices that use charge multiplication for signal amplification. For this reason, several theoretical models for the calculation of the first Townsend coefficient ( $\alpha$ ) have been developed. For example, a very early model [30] gives:

$$\frac{\alpha}{p} = A \exp \left( \frac{-Bp}{E} \right) \quad (2.5)$$

where  $A$  and  $B$  are constants specific for each gas,  $p$  is the gas pressure and  $E$  the electric field applied. Further studies in this matter are shortly reviewed in [31].

### 2.4.2 Single wire proportional counter

As discussed in section 2.2, the gas amplification can be obtained in very different ways. The most straightforward type of charge amplification can be achieved by using a thin anode wire in a cylindrical chamber. This wire is biased with a high voltage and the chamber's walls grounded, which creates a radial electric field capable of triggering an electron avalanche once the electron gets very close to the anode wire, where the electric field is much stronger.

This approach allows only for a very low position sensitivity but, with the use of multiple wires properly arranged, a more precise measurement can be obtained, as it is presented in the next subsection (2.4.3). Figure 2.6 shows a typical single wire proportional counter schematic.

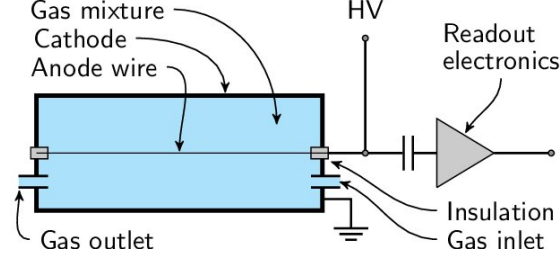


**Figure 2.6:** Schematic of a single wire proportional counter. Retrieved from [32].

### 2.4.3 Multiwire proportional counter

Multiwire proportional counters, introduced by G. Charpak *et al* in 1968 [5], are a natural upgrade of the single wire type. In this case, instead of one central anode wire, a grid of parallel anode wires is used to amplify and measure the signal produced in the drift region. When electrons reach this region, they are accelerated and guided by the electric field lines towards the nearest anode wire where an electron avalanche is created. Since each electron avalanche is captured by a single wire, the position of the interaction (primary ionizing event) can be inferred in the perpendicular direction of the anode wires. Figure 2.7 shows the working principle of these devices.

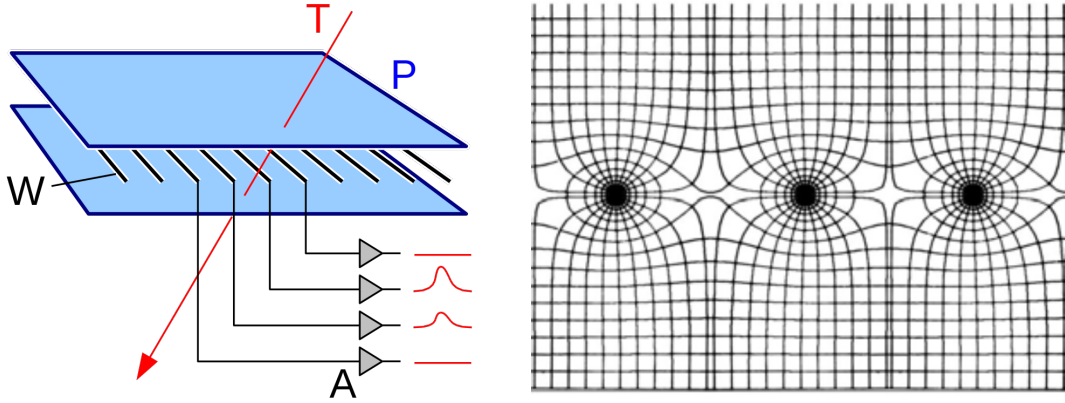


**Figure 2.7:** (Left) Working principle of Multiwire proportional counters where, depending on the position of the initial ionization, specific anode wires acquire a stronger or weaker signal thus allowing the reconstruction of the interaction position, and (right) electric field in each anode wire. Retrieved from [33].

### 2.4.4 Microstrips

Microstrip [34] emerge as an upgrade of multiwire devices, overcoming some of their major limitations: ion charge poisoning created by the accumulation of ions since these drift  $10^3$  times slower than electrons, leading to space charge effects which distort the electric field; lifetime of the anode wires as these can only withstand a limited total charge deposit (0.1-1 C/cm); and the maximum count rate per channel [35].

In this type of devices, the anode wires are replaced by the construction of micrometric metallic strips on a solid insulating support. These strips work as anode and the cathode is a wider metallic layer. This arrangement can be seen in figure 2.8 at the right. With this configuration, it is possible to surpass problems such as electrostatic instabilities and issues related to the mechanical stress exerted on the wires which, in return, improves the maximum flux of tracks that the detector can measure.

Figure 2.8, at the left, also shows the electric field lines created between the cathode and the anode strips. This arrangement works as the multiwire device where electrons create an avalanche while being accelerated towards one anode thus allowing signal amplification and position measurement. The difference is that, with this structure, it is possible to:

1. Collect ions faster which avoids space charge effects thus preventing electric field distortions.
2. Achieve better spatial resolutions as smaller pitches between anode and cathode are attainable when comparing to the necessary spacing between wires in multiwire devices.
3. Obtain greater strip lengths per unit surface than in wire chambers ( $>10x$ ) meaning that a larger area is available for amplification.

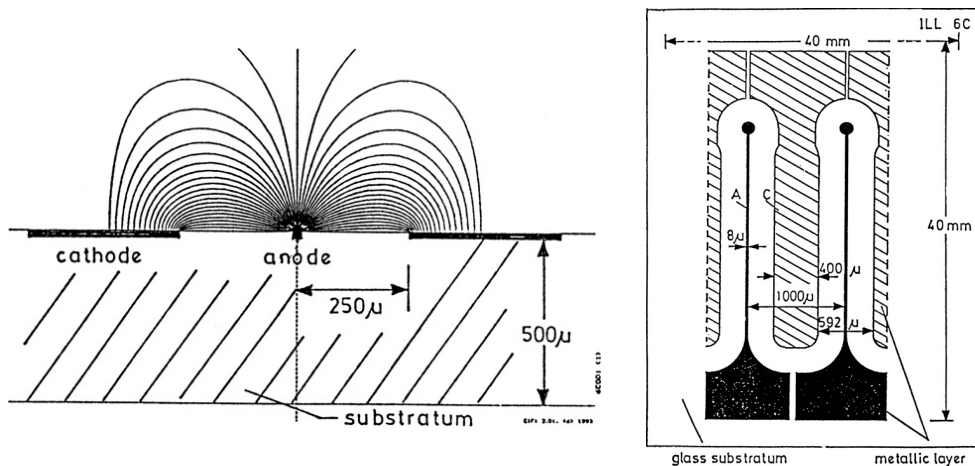


**Figure 2.8:** (Right) Structure of a Microstrip gas detector, and (left) electric field created between its cathode and anode strips. Images retrieved from [34].

A common practice employed with gas detectors that use this amplification technique is to arrange 2 planes of strips perpendicularly in order to achieve a two-dimensional reconstruction of the ionizing event [36].

### 2.4.5 Gas electron multiplier

The Gas Electron Multiplier (GEM) was introduced by Fabio Sauli in 1997 [37] as a detection and amplification device that competed with the microstrip device, already discussed in the previous section, allowing for a more stable operation for longer periods of time [3]. GEMs are composed by a 50-125  $\mu\text{m}$  thick Kapton foil, copper cladded on both sides. More recent developments have shown that GEM thicknesses up to the millimeter scale can also be used [38]. Through the photolithography and acid etching processes, geometrically distributed holes are created along the surface and through the Kapton (figure 2.9, right). If an electrical potential difference is applied between the two copper layers, a very strong electric field is created in the GEM holes (figure 2.9, left). This allows for the electrons crossing the holes to originate an avalanche which amplifies the initial signal. Figure 2.9 shows a schematic of the electric field inside the GEM's holes and a microscopic photograph of a GEM.

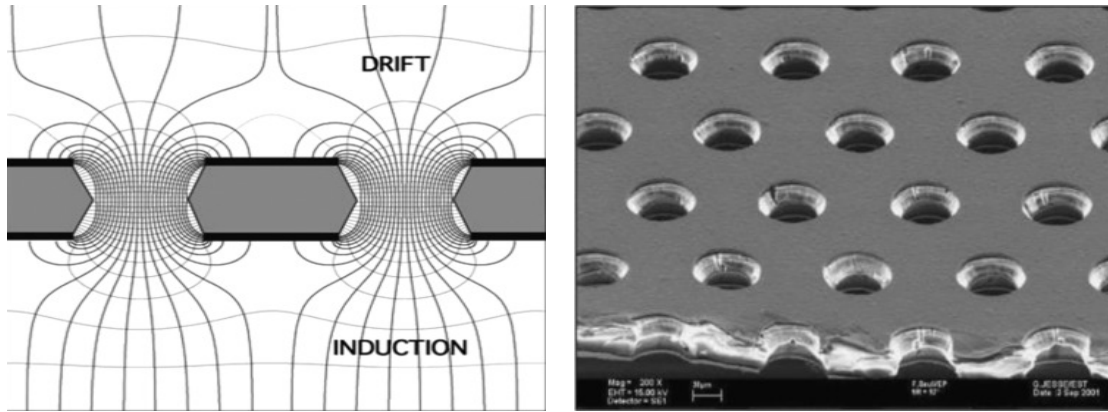


**Figure 2.9:** (Left) Electric field in the GEM's holes and the drift and induction regions and (right) a microscopic photograph of a GEM showing its holes well distributed along the surface. Retrieved from [3].

GEMs can also be stacked on top of each other creating multiple stages of amplification. With this, a much higher gain is possible and with higher stability since lower voltages are needed in each amplification stage. The possible drawback of multiple GEM stacking is the loss of spatial resolution: the very high electric fields between GEMs (denominated *transfer fields*) lead to very high electron diffusions as these become significantly non-thermal while drifting from one GEM to another [39]. Other parameters of GEM operation besides the transfer fields are also typically optimized for each application. Thorough studies on these subjects can be found in [39, 40, 41].

### 2.4.6 Micromegas

Micromegas, an acronym for Micro-Mesh Gaseous Structure, is a structure that arises as a new approach to the microstrip gas chambers in order to overcome issues such as electric field distortions caused by the accumulation of positive ions on the insulator [42]. The small dimensions involved in this device allow a higher granularity and a high gain for smaller dimensions of the chamber.

Inside a Micromegas based detector, a micromesh is used to create two different electric fields within the gas:

1. The drift field, between the mesh and the cathode, where the electrons created by the ionizing particle are drifted towards the micromesh.
2. The amplification field, between the mesh and the anode, where a much stronger electric field is applied, allowing for electron avalanches to occur thus amplifying the initial number of electrons created.

The induction signal created by the electron cloud is finally acquired by, for instance, a system of anode strips, while positive ions are drifted towards and partially collected by the micromesh. The signal formation and acquisition processes can be seen in figure 2.10.

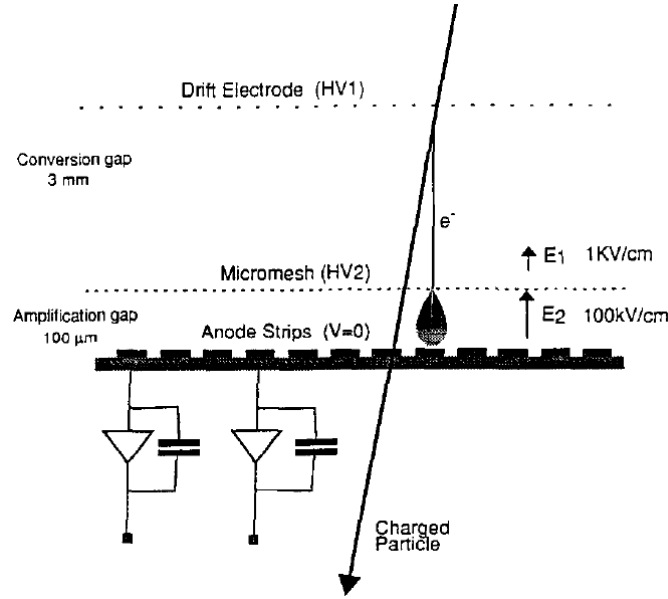


**Figure 2.10:** Schematic of a Micromegas detector using the micromesh to amplify the signal (electrons). Retrieved from [42].

This faster removal of the positive ions differentiate Micromegas from Microstrip and Multiwire chambers since the accumulation of positive ions near the anode is avoided thus enabling higher counting rates. Besides this feature that provides Micromegas the ability of recording much faster signals (hundreds of nanoseconds), another advantage of



Micromegas is its very good spatial resolution, which can reach values below one hundred micrometers [4], achieved due to the very small pitch between wires and between the mesh and the anode.

Micropattern gaseous detectors (MPGDs) [43] are gaseous detectors that use one or more of the referred amplification devices to obtain information of the ionization track of the detected particle. MPGDs were developed with the intent of enhancing the existing gaseous detectors by improving the amplification factor reached; spatial and time resolutions; count rate capability; signal to noise ratio; stability and radiation hardness. MPGDs can be used to only amplify or to also record and image the signals. One example of application of these devices in a gaseous detector is the Time Projection Chamber, that will be described in the following section.

## 2.5 Time projection chambers

The Time Projection Chambers (TPCs) were invented by D. Nygren [44] for the electron-positron (PEP4) collider experiment at SLAC. Their main characteristic is that they allow a 3D reconstruction of the particle track inside the detector. These devices are also ideal for momentum measurement and identification of charged particles.

The most conventional (original) TPC geometry is a cylinder filled with a gas and with an amplification and readout system, such as the ones referred above (in section 2.4), in one or both ends. Such as in other detectors, when a particle crosses the gas, it ionizes its atoms/molecules, leaving a trail of primary electrons. By applying an electric field, it is possible to drift these electrons to the chamber's endcaps where they can then be multiplied and recorded. This process is exemplified in figure 2.11.

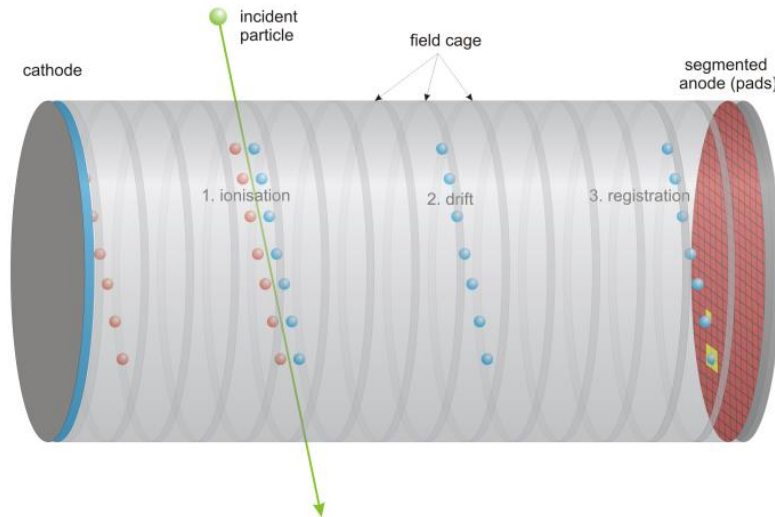


**Figure 2.11:** Typical schematic of a Time Projection Chamber, (by O. Schäfer).

The two-dimensional projection ( $x$  and  $y$ ) of the ionizing track is carried by position



sensitive tracking devices. The relative  $z$  coordinate (track's tilt) can also be obtained by analysing the signal's time development. Depending on the application, the longitudinal dimension (absolute  $z$ ) of the interaction can also be determined knowing the moment ( $t_0$ ) of the start of the event. This information can be obtained resorting to different methods such as, for instance, through the primary scintillation signal or faster subdetectors, when operating at a collider. As for the signal amplification (which can be included in the tracking devices), .

Independently of the type of readout and amplification exploited, one of the most valuable features of TPCs, along with the precise 3D track reconstruction, is the efficient particle identification deduced from the measurement of the particle's energy loss in the medium ( $dE/dx$ ). This tracking capability can also be enhanced by applying, for instance, a magnetic field or exploring different gas fillings, both with the aim of reducing electron diffusion in the medium.

### 2.5.1 Different TPC approaches

TPCs were designed to perform three dimensional reconstructions of ionizations tracks. This can be achieved by using either charge or light signals (the so-called Optical TPCs [45]) or both together and by using sophisticated readout systems with high granularities. For this reason, the geometry, medium and components used in a TPC can greatly differ from one experiment to another. This allows scientists to optimize the TPC in order to meet the experiment's physics case and expectations.

Within the new designs developed in the recent years, some Dark Matter experiments such as the XENON1T [46], DarkSide [47], LUX [48], among others, have decided to use a dual-phase medium meaning that in these experiments, instead of a gaseous TPC, a noble gas is used both in the liquid and gaseous state. In these cases, the higher scintillation feature and higher density provided by liquids are exploited.

TPCs are also used in other physics fields such as high energy physics with the most known experiment being the ALICE TPC [49] at CERN or other rare event searches such as the NEXT experiment [16] in which the physics case is the search of neutrinoless double-beta decays.

### 2.5.2 Negative Ion TPCs

Negative Ion Time Projection Chambers were introduced by J. Martoff [6] and are a peculiar modification of the traditional electron drift TPC. Instead of electrons, NITPCs resort to electronegative gases to generate negative ions that carry the ionization track information. With these anions, it is possible to greatly improve the spatial resolution of TPCs due to the much smaller diffusion conferred by ions when compared to electrons (see Negative Ion Drift in section 2.7.4), thus avoiding the need of resorting to magnetic fields to reduce electron diffusion.

NITPCs are expected to be especially useful at low pressures since diffusion increases with the decrease of pressure (see equation 2.12) or at underground experiments where scaleability is important and the use of magnetic fields is excluded by space and power constraints.

## 2.6 Choice of filling gas

The choice of the filling gas essentially depends on the detector application. Some of the features that characterize a gas are its ionization energy, electron and ion drift velocities, stopping power and light yield. There are also other important factors that should be accounted for when choosing a fill gas:

1. **Type of signal:** While an experiment's physics case might be focused in acquiring a specific type of signal (charge and/or light), the gas choice will also be influenced: if, for instance, light (photons) signals are explored, the gas emission spectrum and the photon detector sensitivity need to be matched, thus a specific gas is needed.
2. **Interaction probability:** The interaction cross-sections typically increase with the number of particles inside the detector. Thus, to increase this probability, denser gases and/or higher pressures are preferred.
3. **Range in gas:** If an experiment intends to observe longer ionization tracks, either with charge or light, low density density gases (He, Ne, etc.) and/or lower pressures are preferred.
4. **Charge drift:** If high count rates are expected, gases with higher charge drift velocities are preferred in order to minimize the resolving time. On the other hand, if high spatial resolutions are desired, slower drift velocities are required to minimize diffusion (see section 2.7.1).

### 2.6.1 Pure noble gases

Noble gases are among the most common choices for gas detectors, due to their high stopping power (namely Xe) and their low Fano factor, which indicates smaller fluctuations in the primary electron signal formation, i.e., in the initial number of electron-ion pairs formed [50]. Since these gases are monoatomic, with no vibration or rotation modes associated, the processes by which electrons lose their energy in collisions with the gas atoms are mainly excitation and ionization. For this reason, noble gases require the lowest electric field intensities (thus, lower working voltages) for the formation of electron avalanches [19]: since electrons barely lose any energy through processes besides excitation and ionization, the efficiency of this process is higher than in molecular gases where electrons can lose energy by other different processes.

The use of pure noble gases also has its drawbacks namely related to secondary avalanches created by the emission of high energy photons (such as in Geiger-Müller tubes, see section 2.3). These avalanches can quickly escalate and originate sparks and discharges within the detector that can permanently damage it or any of its internal components. To overcome this issue, polyatomic gases are typically introduced in the mixture.

### 2.6.2 Molecular mixtures

The addition of polyatomic gases (such as  $\text{CF}_4$ ,  $\text{CH}_4$ ,  $\text{C}_2\text{H}_6$ , among others) in small quantities is used to mitigate and avoid electric discharges within the detector associated with pure noble gases. These molecular dopants, due to their increased number of vibrational and rotational modes, work as *quenching gases* by absorbing the radiated photons and dissipating their energy in excited levels of these modes, in dissociations and/or elastic collisions, thus avoiding further avalanches [19].

Within all the possible gas choices, there are also technical issues that might occur due to the exposure of the detector's components to a specific gas for long periods of time. For instance, the use of organic quenchers (such as  $\text{CH}_4$ ), after high fluxes of radiation have been absorbed, can result in the formation of solid or liquid deposits on the detector's surfaces and electrodes. This often results in the accumulation of charge near the electrodes which then, results in electrical discharges [19]. Another example of technical issues that must be considered is, for instance, the contamination of photomultiplier tubes by the presence of Helium in the gas mixture [51, 52].

### 2.6.3 Electronegative gases

An electronegative gas is a gas whose molecules have the property of easily attaching electrons, producing more stable and long-lived negative molecular ions. With small quantities of these gases, it is possible to considerably change the gas mixture properties, with the most important being the change in the charge carrier. Since electrons easily attach to these gases, the charge/information carriers switch from electrons to anions thus improving the achievable spatial resolution due to the reduced diffusion of ions in the gas (see section 2.7.4). Such as other molecular gases, electronegative molecules (for instance,  $\text{SF}_6$  or  $\text{CF}_3\text{Br}$ ), also absorb photons preventing unwanted electron avalanches [19].

When exploiting negative ion drift, to amplify the charge signal "carried" by the anions, the additional electron has to be removed from the anion so that the electron avalanche can occur (see section 2.7.4). After the electron is stripped, if the electron would be re-captured by the gas molecules, this would momentarily halt the avalanche, preventing further multiplication thus also weakening the energy resolution and gas gain [12]. Furthermore, it was found that the energy resolution in electronegative gases depends on the reduced electric field in the amplification region which indicates that electron detachment and re-attachment are competing within the electron avalanche process [12].

## 2.7 Transport of electrons and ions in gases

As already mentioned in the previous sections, the information carried by the incoming and detected particles is, most of the times, converted into electrons and ions in the gas. These charged particles drift in the gas, usually under an applied electric field, until they enter a region where they are amplified and/or collected. The knowledge of the drifting properties of these charged particles is very important to optimize the detector's performance. In this section we introduce some concepts related with the drifting of these charged particles in the gas. Since this thesis is based on the study of negative ion drift with  $\text{SF}_6$ , a deeper discussion of the ions formed in this gas and how their mobilities are affected is presented in section [2.7.4.1](#).

### 2.7.1 Diffusion

Electrons and ions, after being liberated by the passage of ionizing radiation, and in the absence of an electric field, diffuse uniformly outward from their creation point. During the process, they suffer multiple collisions with the gas molecules and lose their energy thus reaching thermal equilibrium with the gas and eventually recombining. At thermal energies, the velocity of charges is described by the Maxwell distribution and, as a result, the average speed,  $v$ , of these electrons and ions can be expressed as follows:

$$v = \sqrt{\frac{8kT}{\pi m}} \quad (2.6)$$

where  $k$  is the Boltzmann's constant,  $T$  the temperature and  $m$  the mass of the particle. From the kinetic theory, the linear distribution of charges after diffusing during a time  $t$  can be shown to be a Gaussian, i.e.:

$$\frac{dN}{dx} = \frac{N_0}{\sqrt{4\pi Dt}} \exp\left(-\frac{x^2}{4Dt}\right) \quad (2.7)$$

where  $N_0$  is the total number of charges,  $x$  the distance travelled from the point of creation and  $D$  the *diffusion coefficient*. Thus, the root mean square spread,  $\sigma$ , in the  $x$  is:

$$\sigma(x) = \sqrt{2Dt} \quad (2.8)$$

and, if the three dimensions are considered, the spherical spread will be given by:

$$\sigma(r) = \sqrt{6Dt} \quad (2.9)$$

where  $r$  is the radial distance from the creation point of the charge. Also from the kinetic theory, it is possible to calculate the diffusion coefficient which is shown to be:

$$D = \frac{1}{3} v \lambda \quad (2.10)$$

where  $\lambda$  is the mean free path of the charge (electron or ion) in the gas. For an ideal gas,  $\lambda$  is related to the temperature,  $T$ , and pressure,  $p$ , by:

$$\lambda = \frac{1}{\sqrt{2}} \frac{kT}{\sigma_0 p} \quad (2.11)$$

where  $\sigma_0$  is the total cross section for a collision between the charge and the gas molecules. By substituting the velocity distribution and mean free path equations (2.6 and 2.11, respectively) into equation 2.10, it is possible to obtain the explicit expression of the diffusion coefficient, i.e.:

$$D = \frac{2}{3\sqrt{\pi}} \frac{1}{p\sigma_0} \sqrt{\frac{(kT)^3}{m}} \quad (2.12)$$

The dependence of  $D$  on the mass, subject of study in this thesis, is now evident, thus justifying the greater diffusion of electrons compared to ions due to their masses difference. It can also be seen that diffusion is inversely proportional to the pressure and scales with the square root of the cube of the temperature.

### 2.7.2 Ion mobility

Within a gas mixture and under a weak and uniform electric field, ions drift and collide with the gas' atoms or molecules losing their energy while, at the same time, gaining energy from the electric field. Eventually, when the balance between energy lost and gained is achieved, a steady (thermal) state is reached and, as a result, ions drift at an average constant velocity. In this case, the ions velocity,  $v_d$ , is proportional to the electric field's intensity,  $E$ , by the following relation:

$$v_d = K E \quad (2.13)$$

where  $K$  is the ion mobility expressed in units of  $\text{cm}^2 \text{V}^{-1} \text{s}^{-1}$ .

For ideal gases in which moving charges remain in thermal equilibrium, the charge mobility,  $K$ , is also related to the diffusion coefficient ( $D$ ), whose relationship can be expressed through the Einstein relation:

$$\frac{D}{K} = \frac{kT}{e} \quad (2.14)$$

In the thermal regime, electrons and ions diffusion is isotropic meaning that the longitudinal and transverse diffusion coefficients are approximately equal ( $D_T \cong D_L$ ). While being accelerated, the velocity gained by electrons can affect the diffusion rate if these leave the thermal regime. When this happens, the factor  $kT$  in equation 2.14 is replaced by the electrons mean energy. The diffusion then increases accordingly causing a greater spread of the electron cloud as given by equations 2.8 and 2.9. This effect greatly influences detectors that are intended to obtain the ionization track in the gas.

### Effect of gas density on ion motion

In the thermal regime and under a weak and uniform electric field, the drift of charges is characterized by their mean free path between collisions [53],  $\lambda$ , which is given by:

$$\lambda = \frac{1}{\sigma N} \quad (2.15)$$

where  $\sigma$  is the elastic scattering cross section and  $N$  is the gas number density, i.e., the total number of atoms/molecules inside the detector unitary volume. As a result, under the same electric field, it is possible to calculate the average energy gained between collisions by these charges,  $\varepsilon_i$ :

$$\varepsilon_i = q E \lambda \quad (2.16)$$

From classic mechanics, the average energy loss per collision is given by:

$$\Delta\varepsilon = \frac{2mM}{(m+M)} \varepsilon_i \quad (2.17)$$

where  $m$  and  $M$  are the masses of the colliding particles which in our case are the electron or ion mass and the gas molecules, respectively. From this equation, it is already visible that, when using ions as charge carriers, the energy loss is superior thus causing ions to reach the thermal regime - where the energy gained due to the electric field equals the energy loss in each collision ( $\varepsilon_i = \Delta\varepsilon$ ) - much faster than electrons.

### Reduced ion mobility

From the previous equations, it is possible to deduce that the mobility of ions will depend on both the electric field applied and the gas density. So, to facilitate the comparison

between mobility values obtained by different experiments, a normalized quantity called *reduced mobility*,  $K_0$ , is often used and can be obtained using the following expression:

$$K_0 = KN/N_0 = \frac{v_d}{E} \frac{N}{N_0} \quad (2.18)$$

where  $N_0$  is the Loschmidt constant ( $N_0 = 2.68678 \times 10^{19} \text{ cm}^{-3}$  at 0 °C and 1 atm).

The ions mobilities are typically presented as a function of the *reduced electric field*,  $E/N$ , in units of Townsend (1 Td =  $10^{-17} \text{ V cm}^2$ ). This representation intends to remove the dependency of the gas density from the ion mobility obtained as referred. The number  $N$  is related to the pressure so, a normalization of  $E$  to the pressure,  $p$ , can be performed by converting the ratio  $E/p$  to  $E/N$  using the following expression:

$$\frac{E}{N} = (1.0354 \times T \times 10^{-2}) \frac{E}{p} \quad (2.19)$$

where  $T$  is the temperature in Kelvin and  $p$  is the pressure in Torr.

### Effect of ion clusters and water contamination

A key factor to the understanding of ion mobility resides in the full knowledge of how the chemical reactions influence the mobility observed experimentally. Knowing the chemical reactions, we can retrieve the information on the reaction time and determine the ion concentration, which allows us to estimate how much certain ion species can be affected by the predecessor ion during their drift. The formation of ion clusters is an example of a process that can negatively affect ion mobility measurements.

Ion clusters [54] are composed by a central ion with one or more neutral molecules bounded together by charge induced dipoles. By aggregating several molecules, these charged and heavier ions, due to their increased mass, display a slower drift velocity. Since the presence of these ion clusters is expected at room temperature, even at low pressure, it is expected that the mobility experimentally observed might be affected by the formation of such complex ions. For this reason, it is expected that these clusters negatively impact gas detectors which make use of the information/knowledge of ion mobility obtained. In systems in which the mobility of ions is measured (such as the one presented in this thesis), such clusters can induce tails in the time of arrival spectra [12]. So, the confirmation of the presence of these clusters are also of great importance for this work.

To identify the presence of ion clusters, the van 't Hoff diagrams are typically used. These diagrams are especially relevant since they display the equilibrium constant,  $K_{eq}$ , as a function of the inverse temperature,  $T$ , and can be expressed as follows:

$$\ln K_{eq} = -\frac{\Delta H}{RT} + \frac{\Delta S}{R} \quad (2.20)$$

where  $\Delta H$  is the reaction enthalpy change,  $R$  is the ideal gas constant and  $\Delta S$  is the variation of the reaction's entropy. With equation 2.20, it is possible to determine if we are in the presence of an endothermic or exothermic reaction depending if the slope is negative or positive, respectively.

In figure 2.12 is displayed an example of the van 't Hoff diagrams for the  $\text{CO}_2$  cluster formation.

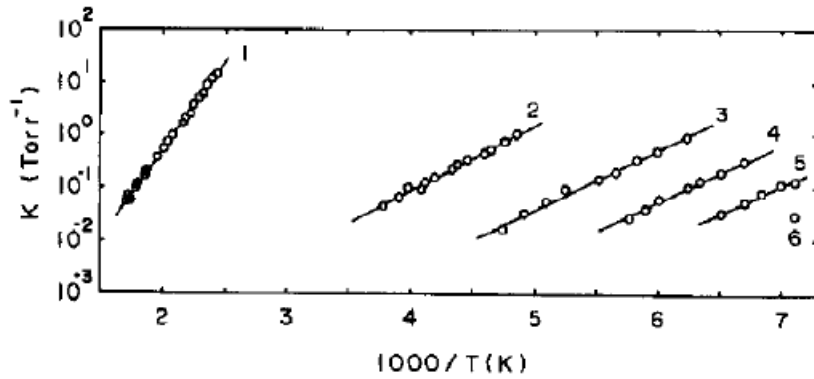


**Figure 2.12:** Van 't Hoff diagrams for clustering reactions  $\text{CO}_2^+(\text{CO}_2)_{n-1} + \text{CO}_2 \rightleftharpoons \text{CO}_2^+(\text{CO}_2)_n$ . Retrieved from [55].

Looking at figure 2.12, it is possible to deduce that the reaction behind the formation of  $\text{CO}_2^+$  based clusters is exothermic (since the slope is positive). For this reason, the appearance of ion clusters in this gas is very likely. Traditionally, cluster growth is expected to be favoured at high pressure and low temperatures, as can be seen from figure 2.12, even though in cases such as  $\text{CO}_2$ , cluster formation is also highly probable at low pressures for a wide range of temperatures. In the same figure, it is also visible that higher temperatures favor the creation of bigger (higher number of aggregated molecules) ion clusters, such as  $\text{CO}_2^+(\text{CO}_2)_6$ .

The presence of water in gaseous detectors can also greatly affect the mobility of ions: since water molecules are polar, these tend to create clusters with the drifting ions thus decreasing their mobility [56, 57]. The effects of water contamination below 50 ppm are negligible while, for higher values, considerable variations in ion mobility have been reported [58].

Another important observation made in [56] is that the effect of water content on ion mobility should be less pronounced with increasing molecular weight of the gas, something already expected from the observed limit for the ions mobility for high ion masses to which is added the difficulty to grow these clusters above a certain dimension because of the stability of the bonds between the molecules.



To avoid cluster formation, higher reduced electric fields are favored as these trigger the *declustering* process which effectively reduces the size (and mass) of ion clusters [58]. This phenomenon occurs due to the increasing of the effective temperature of the ions which leads to the dissociation of the water clusters.

### 2.7.3 Models for Ion-neutral interaction

#### Langevin theory

Depending on the gas density and electric field, the relevance of different ion-neutral mechanisms come into play. To describe them, the Langevin theory is commonly used. This theory has two limits that can be distinguished: the Langevin *polarization* and *elastic* limits.

The Langevin polarization limit represents the theoretical ion mobility limit,  $K_{pol}$ , that is reached when the neutral polarization effect dominates the electrostatic hard-core repulsion [59]. This limit is commonly considered as a reference for the theoretical low-field ion mobility at room temperature and can be calculated with the following expression:

$$K_{pol} = 13.88 \left( \frac{1}{\alpha\mu} \right)^{1/2} \quad (2.21)$$

where  $\alpha$  is the neutral polarizability in cubic angstroms ( $\text{\AA}^3$ ) of the parent gas, and  $\mu$  is the ion-neutral reduced mass. Although generally accepted, Langevin theory has known limitations namely, for instance, when ions transfer charge among them (see, for instance, equation 2.33). In the presence of such interactions, this limit fails to predict correct ion mobilities. This subject is further discussed along the thesis.

When neutral molecules are weakly polarized or very large, the collision between an ion and gas molecules is treated as a rigid sphere collision in which the ion scattering is isotropic. In this case, the Langevin hard-sphere elastic scattering limit,  $K_{elast}$ , is used:

$$K_{elast} = \left( \frac{3e}{16N} \right) \left[ \frac{2\pi}{(\mu k T_{eff})} \right]^{1/2} \left[ \frac{1}{(\pi d^2)} \right] \quad (2.22)$$

where  $d$  is the sum of radii of the ion and neutral molecule. The estimation of this limit is far from desirable since the parameter  $d$  is not known with precision. For this reason, in the studies presented in this thesis, we will only consider the Langevin polarization limit to address and compare the ion mobility values obtained with the dual-polarity ion drift chamber.

### Blanc's Law

In addition to the Langevin polarization limit, Blanc's empirical law [60] has proven to be very useful in the determination of ion mobilities in binary gas mixtures. This expression shows that the ion mobility values obtained are a combination of the ion's mobility in each separate gas. According to this law, the reduced mobility of an ion in a binary gas mixture,  $K_{mix}$ , can be obtained by:

$$\frac{1}{K_{mix}} = \frac{f_1}{K_{g1}} + \frac{f_2}{K_{g2}} \quad (2.23)$$

where  $K_{g1}$  and  $K_{g2}$  are the reduced mobilities of the ion in the pure gas  $g1$  and  $g2$ , respectively; and  $f_1$  and  $f_2$  are the fractions of each gas in the gas mixture. This empirical law is of great interest in the prediction of ion mobilities in gas mixtures and it will be used in this thesis for the identification of the drifting ions present in the detector.

#### 2.7.4 Negative ion drift

When an electronegative gas is added to the filling gas, the electrons originated by the interaction of the incoming particle with gas atoms/molecules are captured by the electronegative gas at very short distances (tens of microns). The anions formed drift to the anode just like electrons would but, in this case, anions reach the thermal regime much faster due to their much larger mass as the energy loss in each collision with the gas molecules is larger than for electrons (see equation 2.17). For this reason, and since diffusion also decreases with the increase of mass (see equation 2.12), the use of anions as charge carriers largely improves the spatial resolution of the ionization track. On the other hand, negative ions, due to their lower mobility compared to electrons, also limit the maximum count rate attainable as they take more time to travel from the ionization point to the readout plane.

When the anions reach the amplification region, in order to amplify the charge signal, it is necessary to strip the additional electrons from them. Since, apart from electron multiplication, there is the additional process of electron stripping, the amplification process typically requires higher electric fields than gases that use electrons as information carriers even though the electron affinities are usually lower than the ionization potentials [61]. For  $\text{CS}_2$ , it was experimentally demonstrated that reduced electric fields of one order of magnitude higher are needed to begin the avalanche process, comparing to the electron drifting gas P10 (10% methane in Argon) [61]. Nonetheless, gas gains greater than  $10^3$  with this type of mixtures have been reported using MWPCs [62], GEMs [63] and Micromegas [64].

While the anions formed in the gas are being drifted and/or accelerated, several processes can occur, namely auto-detachment, stabilization and dissociation, as explained later in section 2.7.4.1. These processes originate different ions from the same original anion, fre-

quently with lower masses, which are denominated *minority charge carriers*. The presence of these different anions species was first discovered by the DRIFT experiment [10] with the gases CS<sub>2</sub> and O<sub>2</sub> [11]. Minority charge carriers were found to be another powerful advantage of negative ions as charge carriers for possible event fiducialization: in experiments where the time ( $t_0$ ) of the initial ionization event is unknown and cannot be observed, the use of the drift time of minority charge carriers has proven to allow the extraction of the absolute  $z$  coordinate of an ionization event [11, 12].

Since the mobility depends on the mass, the difference in the time of arrival of different anions created from the same parent gas provides a measurement of the position of the event along the drift direction, i.e., the event's absolute  $z$  coordinate. In fact, and using the SF<sub>6</sub> gas as an example, by knowing both the primary ion (SF<sub>6</sub><sup>-</sup>) and secondary ion (SF<sub>5</sub><sup>-</sup>) drift velocities,  $v_p$  and  $v_s$ , respectively, and using the time separation between the drift of both anions,  $\Delta T$ , it is possible to deduce the initial interaction's absolute  $z$  coordinate of the event using equation 2.24 :

$$z = \frac{v_s \cdot v_p}{v_s - v_p} \Delta T \quad (2.24)$$

This new trigger-less approach used to determine the absolute  $z$  of the ionizing track enhances the fiducialization process and has already allowed DRIFT to obtain background-free limit from a directional dark matter experiment [65].

In sum, the use of electronegative dopants in the gas filling provides the capability of exploiting negative ion drift instead of electron drift which allow a smaller diffusion, enabling better track reconstruction and also allowing the determination of the initial ionization event position, i.e., its absolute  $z$  coordinate.

### 2.7.4.1 The SF<sub>6</sub> gas case

More recently, the presence of minority charge carriers in negative ion drift with SF<sub>6</sub> has been found [12]. Between the several electronegative gases that can be used as filling gases, as referred, there are three in which the presence of minority charge carriers has been found: SF<sub>6</sub> [12], CS<sub>2</sub> and O<sub>2</sub> [11]. Between these, SF<sub>6</sub> stands out due to being non-toxic and non-flammable whereas CS<sub>2</sub> is highly toxic and, if mixed with O<sub>2</sub>, it also becomes flammable and potentially explosive [66]. Combined with these constraints for the use of CS<sub>2</sub> and O<sub>2</sub>, the easy access to SF<sub>6</sub> makes this gas ideal for studies and applications with electronegative gases.

Our study of negative ion drift was focused on the use of SF<sub>6</sub> and, for that reason, a more detailed study concerning the processes behind the creation of several ion species in SF<sub>6</sub> will be presented. This will help to interpret the results obtained with the experimental setup.

### Electron capture and transport in SF<sub>6</sub>

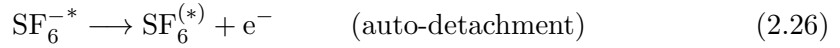
*Electron attachment* occurs when an electronegative atom/molecule collides with an electron and captures it. This process can be either dissociative or non-dissociative, depending if it breaks the molecule's chemical bonds [67].

Electron capture in SF<sub>6</sub> occurs rapidly with the electron attachment cross-section peaking at  $\sim 0.0001$  eV and with the product being a metastable excited state of the ion (equation 2.25). The probability of this process then rapidly decreases as the electron energy increases, with the cross-section reducing by a factor of  $10^3$  at 0.18 eV [68].

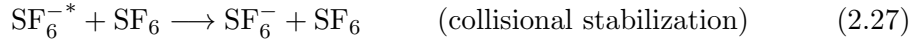


The anion SF<sub>6</sub><sup>−\*</sup>, since it is a metastable ion, is then converted into to others species depending on its lifetime:

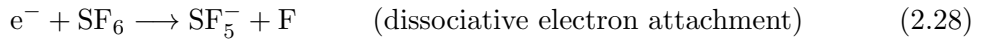
1. Although less likely, this metastable ion can return to its initial state by losing the excessive electron by *auto-detachment*:



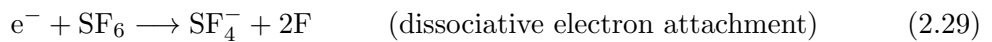
2. The mean lifetime of SF<sub>6</sub><sup>−\*</sup> is greater than 1  $\mu\text{s}$  and so, before losing its electron, the anion will, most likely, generate the stable ion SF<sub>6</sub><sup>−</sup> by either radiative stabilization of the excited state or by *collisional stabilization*, i.e.:



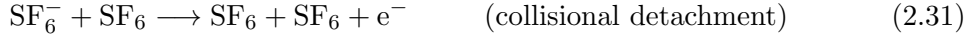
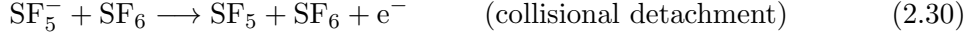
The most probable minority ion species originated from SF<sub>6</sub>, SF<sub>5</sub><sup>−</sup>, is originated through *dissociative electron attachment*, i.e., one electron is captured by a SF<sub>6</sub> molecule and, in this process, it breaks the molecule chemical bonds, ejecting one Fluorine atom from the molecule (equation 2.28). The cross section of this process peaks both at  $\sim 0.001$  and 0.38 eV, rapidly decreasing for higher electron energies [68].



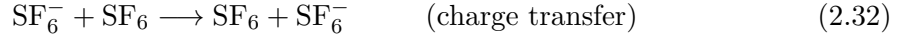
Other minority species such as SF<sub>4</sub><sup>−</sup>, SF<sub>3</sub><sup>−</sup>, SF<sub>2</sub><sup>−</sup>, F<sub>2</sub><sup>−</sup> and F<sup>−</sup> can also be produced following similar processes. For instance, SF<sub>4</sub><sup>−</sup> is expected to be created through the process in equation 2.29 :



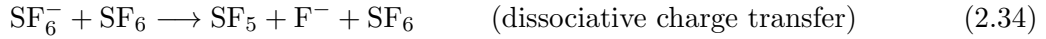
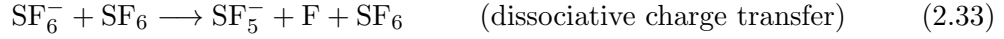
Other collisional processes can also produce neutral states of the  $\text{SF}_6$  molecule, by equations 2.30 and 2.31 :



It is also possible that *charge-transfer* reactions occur. In these, when an ion collides with a neutral molecule, it transfer its charge (electron) to the neutral molecule, such as in equation 2.32 :



It is also possible that this charge transfer is followed by a molecular dissociation, by equation 2.33 and 2.34 :



In sum, there are several possible atomic interactions between  $\text{SF}_6$  and its ions. A extensive collection of studies concerning these reactions can be found in [68], along with a representation of all these ion species suggested cross-sections, shown in figure 2.13. It is possible to see that the most probable anions to be formed will be  $\text{SF}_6^-$  and  $\text{SF}_5^-$  while the other species will only appear for higher electron energies.

The cross-sections for all these reactions, although measurable [68], mix together in a small range of energies which hardens the identification of the main processes behind the ions created. Furthermore, depending on the setup, gas and operating conditions used, particular processes might be favored over others. The occurrence of these processes will also affect the mobility values obtained with our system since different ions will have different mobilities and processes such as charge transfers can delay the ion drift.

Regardless of the intermediate atomic interactions, the presence of different ion species created from  $\text{SF}_6$  have been demonstrated and, within this thesis, the same subject is studied in order to have a better understanding of the processes behind the creation of such minority ion species and how their appearance can be moderated and/or enhanced. Also, the knowledge of these processes in  $\text{SF}_6$  will be very important to verify the performance of the DP-IDC which will support other studies and experiments focused on negative ion drift with  $\text{SF}_6$ .

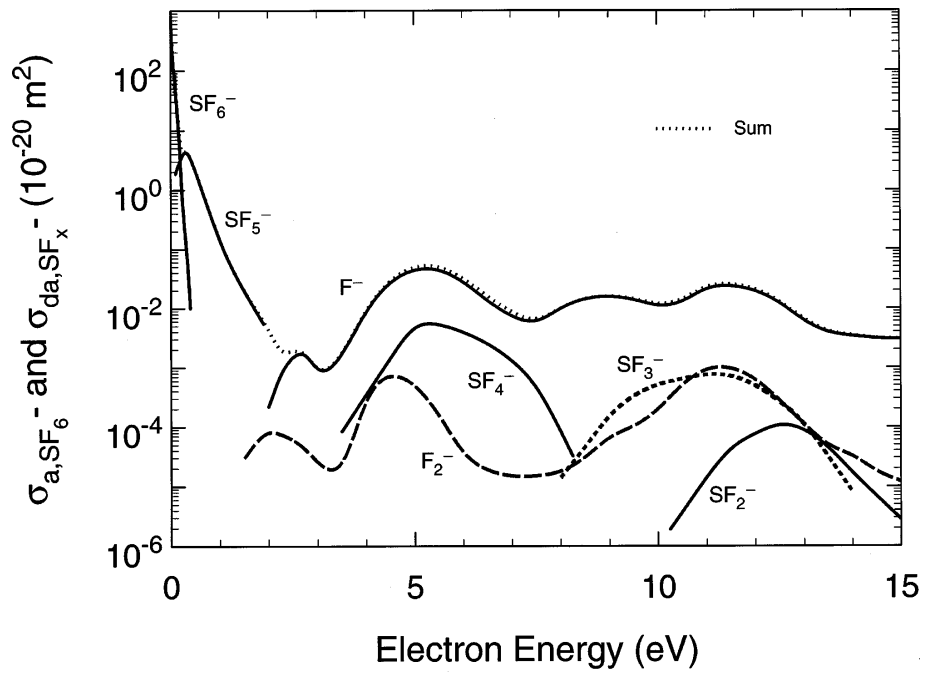


**Figure 2.13:** Suggested cross sections for the formation of  $\text{SF}_6^-$  by electron attachment ( $\sigma_{a,\text{SF}_6^-}$ ) and the remaining species by electron dissociative attachment ( $\sigma_{da,\text{SF}_x^-}$ ). Retrieved from [68].

## Chapter 3

# Dual-Polarity Ion Drift Chamber

For this thesis, since there was already an initial prototype of the Dual-Polarity Ion Drift Chamber (designed by Miguel Santos in his MSc Thesis [69]), several studies were conducted in order to identify its major limitations and understand their sources. After this, it was possible to proceed with several changes focused on reducing all the possible limitations and obtain the best performance that the DP-IDC can output.

This chapter presents the several modifications implemented on the setup, the midway simulations, the preliminary tests, and first studies performed and results obtained with the DP-IDC in the scope of negative ions drift.

### 3.1 Detector working principle

In several aspects, this detector works similarly to the previous prototype used for positive ion mobility measurement [70]. Nonetheless, it has a variety of distinctive features considering that it was built to retrieve information concerning several aspects of a gas mixture such both positive and negative ion mobilities and diffusion coefficients. To provide a clear understanding of such features, a list of them is presented right below. This list is directly linked to figure 3.1 which is a schematic of the working principle of this detector.

1. To start a measurement, a flash from the Xe Ultra-violet (UV) lamp [71] is emitted. This pulsed signal is sent with a frequency of 10 Hz and a pulse duration of less than 500 ns. Once the light hits the CsI photocathode deposited on top of the GEM, photoelectrons are released from it.
2. Due to the very intense electric field inside the GEM, these photoelectrons are guided to the GEM's holes where they are accelerated. The GEM, in this setup, is biased only to achieve a gain close to 2 as we do not require electron multiplication. The ions produced in this stage can be either positive or negative depending on the gas mixture used.

### 3.1. DETECTOR WORKING PRINCIPLE

- (a) Positive ions are produced by electron impact ionization thus generating electron-ion pairs. In this case, electrons have to be accelerated to acquire the minimum energy to ionize the gas atoms. The gain is purposely kept low to avoid a very high number of ions created by a single electron as this might originate space charge effects which would distort the electric field. Negative ions are initially produced by electron attachment so even lower electric fields across the GEM are needed since attachment is favoured for low electron energies (see  $\text{SF}_6$  case in section 2.7.4.1).
3. The ions generated are now pulled towards the double grids at the bottom and top of the chamber, depending on their charge polarity, due to the uniform electric field inside the chamber. During their drift, ions will suffer both longitudinal and transverse diffusion. Besides diffusion, ions will also suffer other processes such as collisions, dissociations and charge transfer (see section 2.7) that occur during their drift. These processes will affect the ion drift time, resulting in a Gaussian shaped time of arrival spectrum.
4. After crossing the Frisch grid, the movement of these ions induce an electrical signal in the collection grid which is later converted from charge to voltage by a pre-amplifier, being then fed to an oscilloscope for digital recording and originating a time spectrum from which the drift time of the different ions moving in the gas can be inferred. The Frisch grid is of great importance in this step as it prevents the collection grid to collect the induced signal caused by the moving charges along the whole drift region and improves the overall quality of the signal.

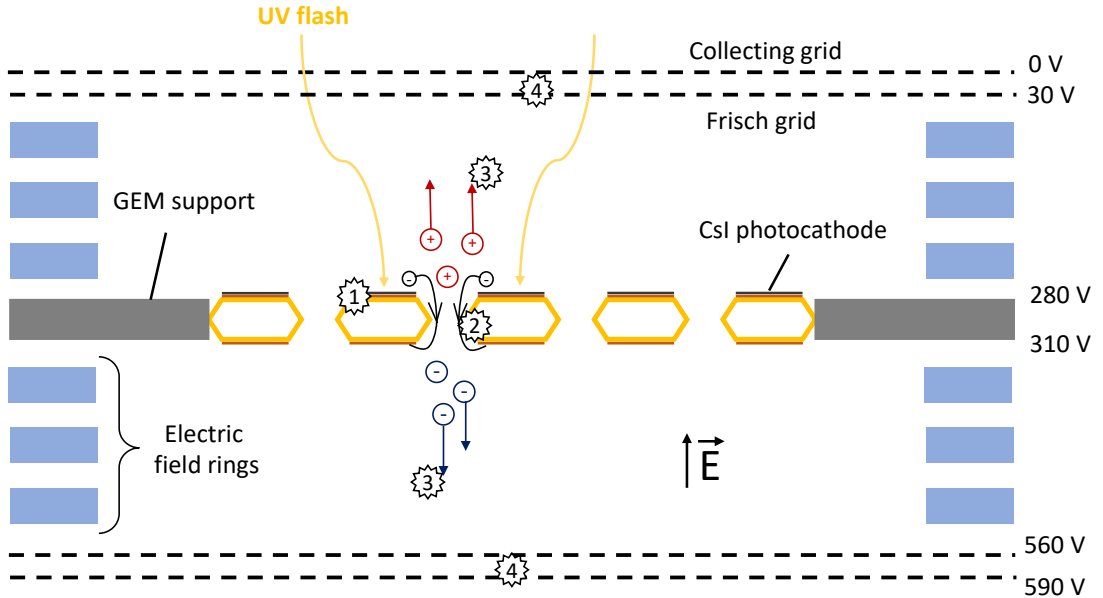


**Figure 3.1:** Schematic of the detector's working principle with its main 4 steps represented.



### 3.2. CHAMBER DESCRIPTION

5. The data treatment and analysis of the obtained time spectra is carried by a computer after the signal from the pre-amplifier is recorded by the oscilloscope (explained in detail in section 4.1). Values such as ion mobilities can be calculated by analysing the time of arrival spectra. Several studies can then be performed with different gases, pressures, electric fields, together with a variety of other changeable parameters.

### 3.2 Chamber description

This chamber consists on a vacuum sealed cylindrical vessel made of stainless steel. The inside of the chamber is symmetrical to the center, where the GEM is placed. The full description of the chamber is followed as well as a schematic of the chamber, shown in figure 3.2.

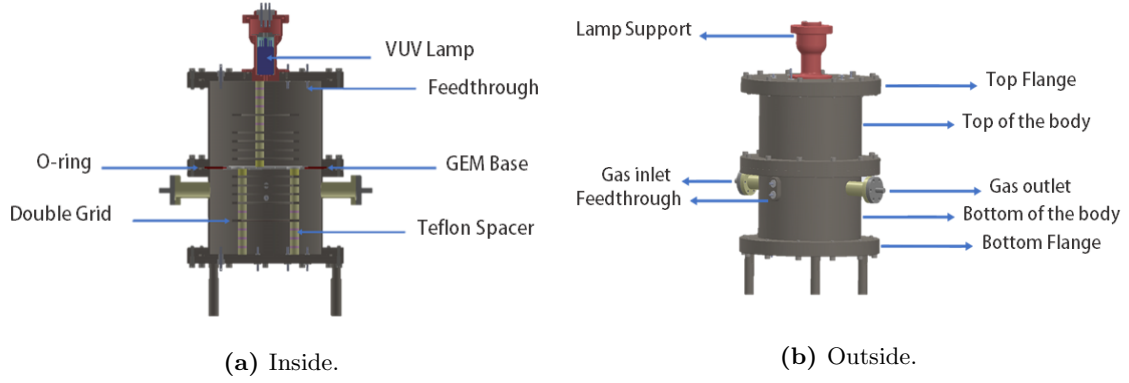


**Figure 3.2:** Detector's inner and outer drawings.

- At the middle, there is a support that holds a  $1 \times 1 \text{ cm}^2$  GEM used to produce ions.
- From the middle to the top and bottom, there are 4 metal rings (to each side) which are connected to a voltage divider system in order to provide different voltages to each ring thus maintaining a uniform electric field within the drift region. These *field rings* are also separated by equally sized Teflon spacers that provide proper isolation between them.
- On the top and bottom, there are 8 feedthroughs to allow electrical connection to the field rings from the outside. The electrical connection to the GEM's electrodes is made through two side feedthroughs. A better and more detailed explanation is given later in section 3.2.1.
- Closer to the top and bottom flanges, there is a pair of metal grids separated by a very thin ( $50 \text{ }\mu\text{m}$ ) Kapton foil. These double grids are of great importance for the performance of the detector as they work one as a Frisch grid and the other as the collection grid.

### 3.2. CHAMBER DESCRIPTION

- Frisch grids are used to improve the detector's time resolution as the signal's rise time becomes smaller and the main peak higher when they are used. This happens because the signal produced by the movement of charged particles towards the grids is "collected" on the Frisch grid thus making the rise time of the particles arriving at the collection grid (anode) smaller and, hence, improving the signal acquired. A detailed study proving the necessity of this grid in systems similar to the DP-IDC was conducted in [70].
- There are two gas inlets used to fill or evacuate the detector. The use of two inlets instead of just one considerably improves the gas out-flowing when evacuating the chamber or, in other words, producing vacuum.
- On the top, there is a support for the VUV lamp.

#### 3.2.1 Electrical system

As discussed, the chamber was built in order to work both entirely and by modules (either just with the upper or bottom part). Here, as an example, the electrical system for working with only the upper part is shown (figure 3.3) and explained.

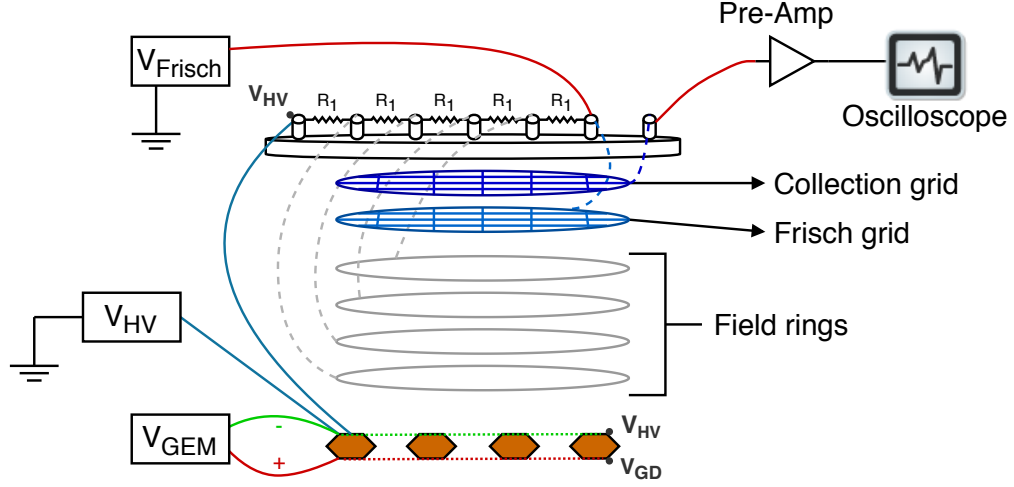


**Figure 3.3:** Electrical system scheme of the chamber when working by modules (upper module, in this case).  $R_1 = 22\text{M}\Omega$  and  $V_{\text{GEM}} = V_{\text{GD}} - V_{\text{HV}}$ .

Going from the higher potential to the lowest:

1. The higher voltage is connected to the GEM's top side,  $V_{\text{HV}}$ .
2. The GEM's *floating* power supply is connected to it, being the positive connected to the bottom,  $V_{\text{GD}}$ , and the negative to the upper side,  $V_{\text{HV}}$ , with  $V_{\text{GEM}} = V_{\text{GD}} - V_{\text{HV}}$ .

### 3.3. PREVIOUS LIMITATIONS

---

3. The first feedthrough is at the same voltage as the top of the GEM ( $V_{HV}$ ) and, from there, a series of resistors (with value  $R = 22M\Omega$ ) follows until the feedthrough connected to  $V_{Frisch}$ , thus creating a voltage divider throughout the field rings allowing a uniform electric field within the drift region.
  - The resistors' value is irrelevant as long as they all have the same resistance so, a high resistance was chosen to ensure electrical stability in case of discharge and to avoid leakage currents.
4. The collection grid is then connected to the feedthrough that is isolated from the others and which is connected to a pre-amplifier. The pre-amplifier collects all the accumulated charge on the grid and generates a proportional electrical signal, which is then read by an oscilloscope.

### 3.3 Previous limitations

The first measurements of positive ion mobilities, performed using the upper part of the chamber [69], were not accurate as we can see in a table 3.1.

**Table 3.1:** Table of the first ion mobility values obtained with the DP-IDC. Results retrieved from [69].

Gas	$V_{GEM}$ (V)	E/N (Td)	Experimental Mobility	Previous work
CF <sub>4</sub>	35	30	$0.654 \pm 0.001$	$1.072 \pm 0.006$
N <sub>2</sub>	35	20	$1.36 \pm 0.06$	$2.37 \pm 0.01$
N <sub>2</sub>	25	25	$1.32 \pm 0.06$	$2.36 \pm 0.01$
N <sub>2</sub>	35	30	$1.43 \pm 0.06$	$2.36 \pm 0.01$

This section explores the possible causes of the low accuracy obtained for these results and is followed by a section in which the modifications and optimizations introduced, to improve the detector's performance, are illustrated (see section 3.4).

#### 3.3.1 Lamp signal

The first aspect that characterizes the measurement is the Xe lamp UV flash which enables the creation of photoelectrons from the CsI photocathode that, while crossing the GEM's holes, ionize the gas or attach to it. Since the initial lamp's flash indicates the initial time ( $t_0$ ) of the ion creation, the lamp signal becomes a rather important feature of the measurement. For this reason, it is important to understand how the final signal is affected by it and if there are any limitations imposed by the lamp.

Assuming an initial pulse width of 500 ns (characteristic of the lamp used), no ion mobility signal should appear overlapped in this pulse. In the first version of the DP-IDC, the signal induced by the lamp proved to be around 200 times larger ( $\sim 100 \mu s$ ). This is, most likely,

### 3.3. PREVIOUS LIMITATIONS

one of the error sources that culminated in the inaccurate results presented above (table 3.1): having such a large initial signal resulted in the drift time signals obtained being within this large peak, i.e., overlapped with the lamp signal. Figure 3.4 shows the large width of the lamp's signal.

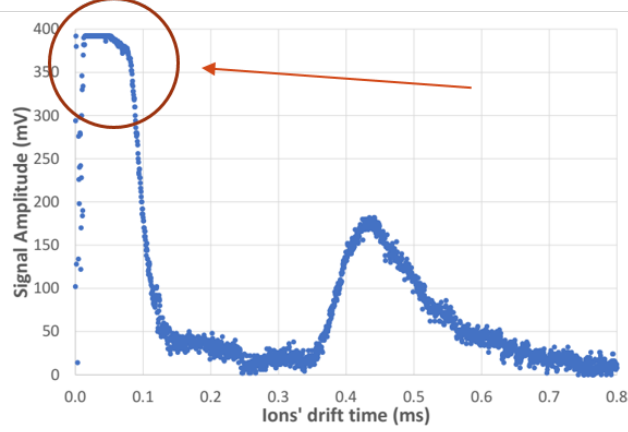


**Figure 3.4:** Measurement of an ion's time of arrival spectrum. It is visible that the initial peak caused by the lamp is as broad as, almost,  $100 \mu\text{s}$ , when the expected width was  $500 \text{ ns}$ . Spectrum retrieved from [69].

The nature of this problem was addressed with great care as it was one of the main contributors for the initial low performance of the system. The studies performed in this matter and their respective outcomes are presented in section 3.5.1.

#### 3.3.2 Electric field

Other crucial task necessary to achieve accurate results is assuring a nearly perfect electric field uniformity. Several simulations were carried out by Miguel Santos to verify the field's uniformity. These simulations are presented in figure 3.5.

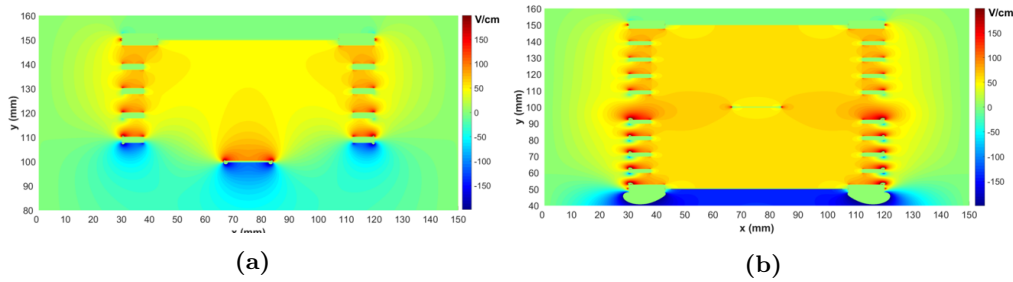


**Figure 3.5:** Simulations performed to analyse the electric field inside the chamber. It is presented the (a) vertical electric field when only half of the detector is biased and (b) when it is fully biased. Retrieved from [69].

As it can be seen in figure 3.5a, the electric field is far from being uniform when only the top part of the chamber is biased (configuration used to measure positive ion mobilities).

On the other hand, when the full detector is biased (3.5b), the electric field appears to be rather uniform, being the central part (next to the GEM) the only part with slight non-uniformities. In order to reach clear and unbiased results, a very uniform electric field within both drift regions is strictly necessary.

For this reason, a new central piece - which holds the GEM - was projected, designed and produced and, later, tested for its performance. This is shown in the following section.

## 3.4 Optimizations performed

In order to overcome the limitations shown in section 3.3, several studies and simulations were carried out which later resulted in a few important technical improvements. Along the way, all the proper vacuum and electrical tests were performed to ensure that each modification was behaving as expected and no other problem (such as gas leaks or bad connections) was introduced in the setup. These tests involved, for instance, regular gas leak tests with alcohol and acetone and the measurement of absolute voltages in critical points of the system.

### 3.4.1 Development of a new GEM base

As discussed, one of the main limitations was the electric field as it wasn't as uniform as expected (figure 3.5), both when working entirely and by modules.

Since the electric field non-uniformities are more visible at the central part (where the GEM is positioned), the improvement was focused in creating a component that could both hold the GEM and maintain the electric field uniformity along the chamber.

As we believed that the problem was the fact that the central disk that held the GEM was made of an insulator material (Teflon) which does not allow the precise definition of the electric potential, we considered that the solution was to place the GEM between two metal plates separated by a Kapton foil and with a small square-hole in the middle so that the ion formation processes enunciated in section 3.1 could still occur. Before designing the new piece, simulations of the electric field with this modification were conducted.

#### a. Electric field simulation

The simulations of the electric field inside the chamber were carried out before the design of the final version of the GEM holding piece to ensure a near perfect tuning of all the aspects of this component. These simulations, performed using the software Maxwell [72], were designed to represent the real detector as close as possible in a two dimensional view: in the middle, there is the GEM and a continuous line (not perceptible) from it to the borders, representing the 2 metal plates. On the sides, there are small squares, representing the field rings, separated by Teflon. On the top and bottom, there are 2 grids

### 3.4. OPTIMIZATIONS PERFORMED

- Frisch and collecting grid. All the components were biased matching the real setup. The results of the simulation are shown in figure 3.6.

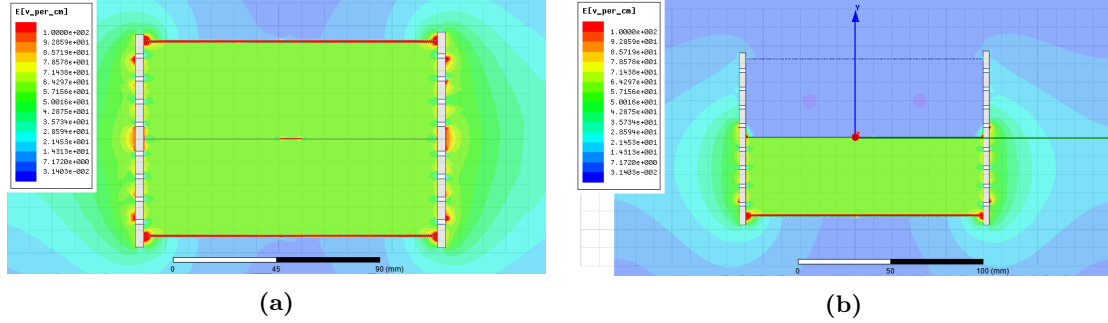


**Figure 3.6:** Electric field polarizing (a) the whole chamber and (b) only the bottom part of the chamber and with the top part with null electric field.

Analysing figure 3.6a, one can see that the electric field is now very uniform in the whole sensitive area (within the field rings). At the right (3.6b), one can see that the chamber also works very well when using/biasing only one of the halves (bottom, in this case).

#### b. Design and production

After confirming that, by substituting the GEM's Teflon holder for a double-plate metallic holder, it is possible to substantially improve the electric field within the whole chamber, the new central piece was finally designed and assembled. This piece was designed using the software SolidWorks [73] and manufactured in the laboratory's mechanical workshop by experienced professionals. Figure 3.7 shows the different steps of this component's evolution.

To ensure that the GEM was properly biased, each of the metallic plates was electrically connected to either the upper or the lower part of the GEM and, then, these were interlocked to a larger Teflon ring that holds this structure to the chamber to keep everything static and fixed, assuring, at the same time, electrical insulation to the chamber walls.

#### 3.4.2 GEM characterization

As explained above, the GEM's objective in this setup is only to accelerate the electrons enough for them to create one ion-electron pair (ionization), or to attach to an atom/molecule of the gas. In terms of size, in general, a bigger GEM area would imply a greater number of ions being created which usually is always beneficial. On the other hand, a bigger GEM would require a greater maneuvering care and substantially bigger costs. For these reasons, the GEM used for this application had an area of  $1 \text{ cm}^2$  and a Kapton thickness of  $50 \text{ }\mu\text{m}$ .

An example of the GEM used is visible in figure 3.8 as well as a microscope observation of such GEM using the facilities and expertise of TAIL group, at University of Coimbra.

### 3.4. OPTIMIZATIONS PERFORMED

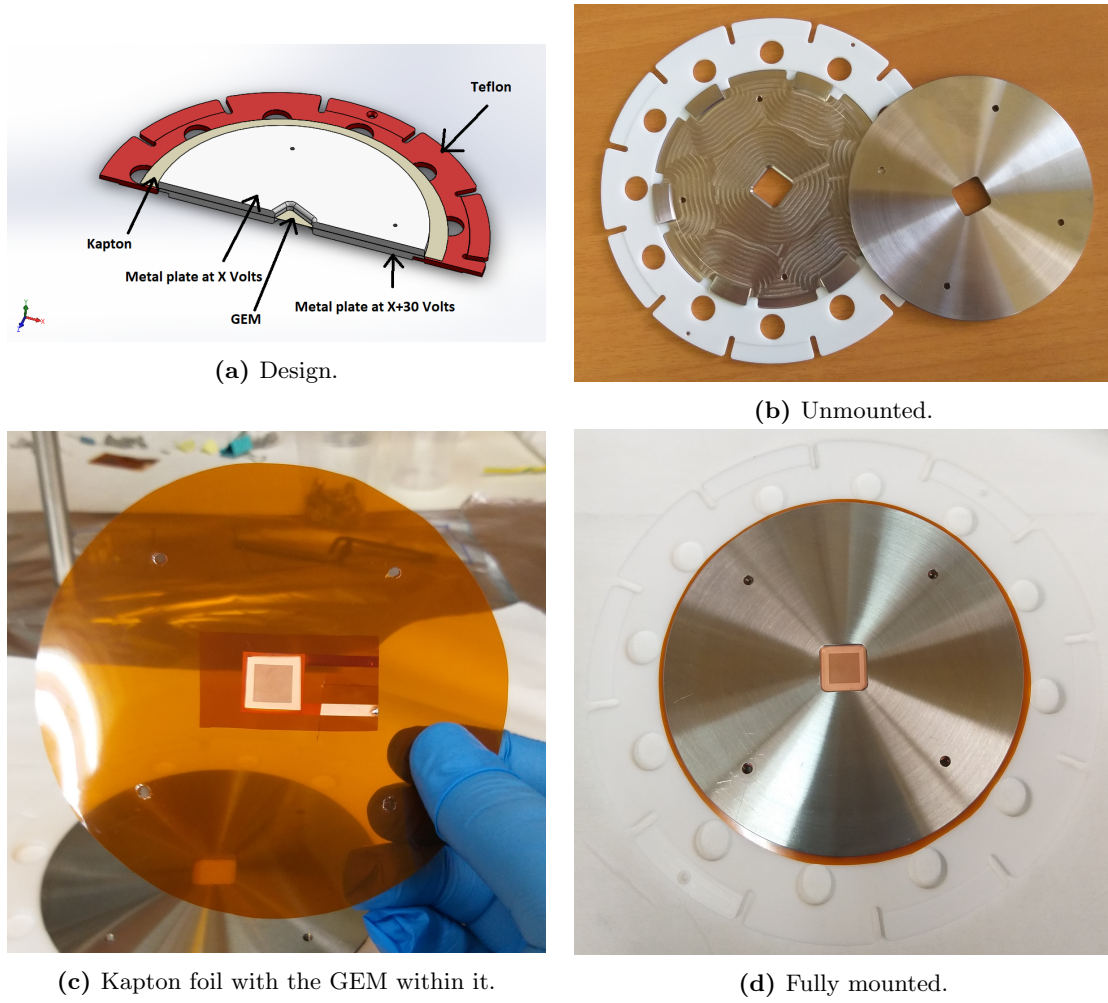


**Figure 3.7:** (a) Design of the central piece used to hold the GEM and to ensure the electric field's uniformity. (b) The manufactured component. (c) GEM's electrodes separated by the bigger Kapton foil. (d) The central part fully mounted, with the Kapton excess around the plates to prevent electrical discharges. Small holes along the Teflon ring were also foreseen for this component to ease the gas flowing within the chamber.

#### 3.4.2.1 Leakage current

Leakage current is a parameter broadly used in physics to assess the quality of the GEM. This parameter can be measured with a simple setup where a high voltage<sup>1</sup> is applied between its two copper layers. Usually, to improve electronic stability and safety, the lowest potential layer is grounded.

Moreover, the GEM's leakage current also depends on the GEM's size and insulator's thickness making the acceptable value linked to the experiment's needs. Nevertheless, one

<sup>1</sup>High voltage in this context refers to a voltage of about hundreds of Volts. Moreover, the values used depend entirely on the application: depending on the gas and pressure in which the GEM is placed, discharges will be seen at different voltages.



### 3.4. OPTIMIZATIONS PERFORMED

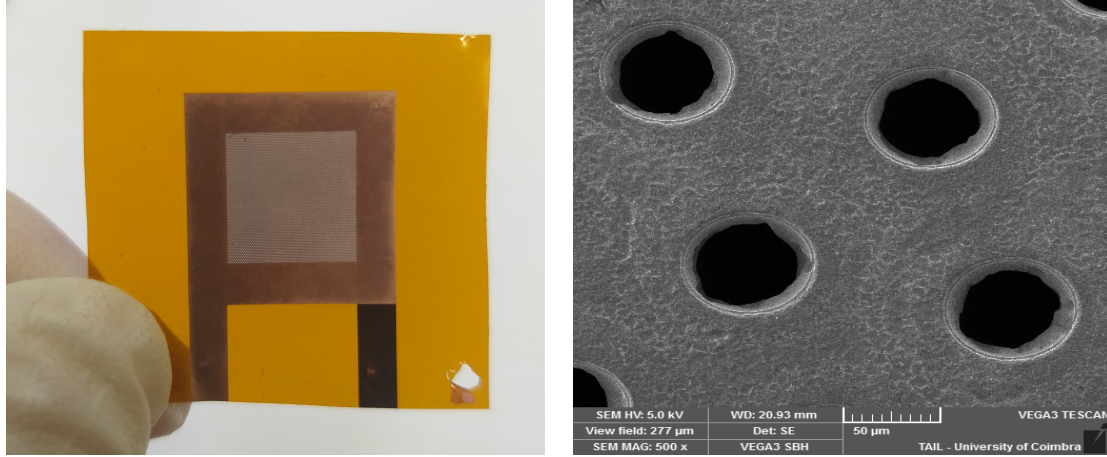


**Figure 3.8:** Example of a  $1 \times 1 \text{ cm}^2$  GEM with (left) naked eye and (right) an electronic microscope.

can use, as reference, the value of 200 nA as acceptable for a voltage of 500 V [74].

The measurement of the GEM's leakage current was performed in two different situations:

1. GEM stand-alone
2. GEM mounted in the central piece

The values presented in figure 3.9 were obtained by sweeping the voltage applied on the GEM both when standing alone (directly on its electrodes) and when mounted on the new central piece where the voltage is applied on the metal disks which make electrical contact with the GEM's electrodes.

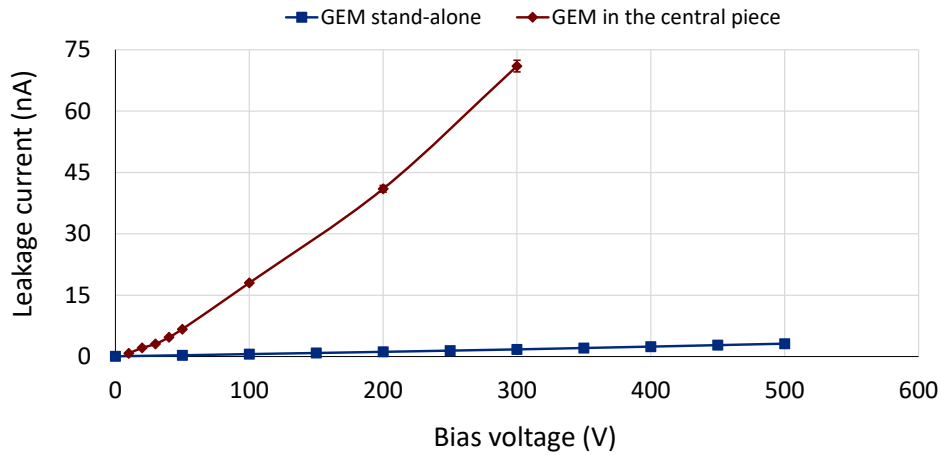


**Figure 3.9:** GEM's leakage current when standing alone and when mounted in the central piece. These values have a reading error of 2 %.



### 3.4. OPTIMIZATIONS PERFORMED

---

Considering the values obtained, this GEM, when used alone, was considered very acceptable for the setup as the maximum leakage current obtained, 3.15 nA, is well below the roughly set threshold (200 nA).

For the second case, where a greater leakage current is observed, it should be noted that there are two round metal plates with an electrical potential difference, with just a thin (50  $\mu\text{m}$ ) Kapton foil separating both. The leakage current measured initially for the whole central part with the GEM was of  $\sim 600$  nA. This value was well above the acceptable. The resistance measured between the two plates was of 2,3 G $\Omega$ .

This problem was quickly solved by replacing the existing Kapton foil between the plates by a thicker one with 125  $\mu\text{m}$  thickness. This proved to be enough to increase the resistance between the foils (therefore, reducing the leakage current) from 2,3G $\Omega$  to 155,3 G $\Omega$ . The values obtained with the thicker Kapton foil are plotted in figure 3.9 in red.

In conclusion, comparing both cases, one can observe than once the full central component is assembled, the leakage current raises to much higher values (71 nA at 300 V). Despite this, the current measured is still under the imposed threshold and, since the the voltage to be applied on the GEM when operating in the experimental setup will be, at maximum, 50 Volts, the leakage current will correspond to an even lower value (6.7 nA).

#### 3.4.2.2 Cesium-iodide deposition

To proceed with the measurements, a CsI film had to be deposited on the GEM. This was done using the thermal evaporation technique with an existing evaporation plant in the laboratory facilities. Thermal evaporation is a vacuum technique used to make thin film depositions on surfaces. In this case, the CsI film was used as a photocathode inside the detector to originate photoelectrons. Figure 3.10 shows a simplified schematic of a thermal deposition.

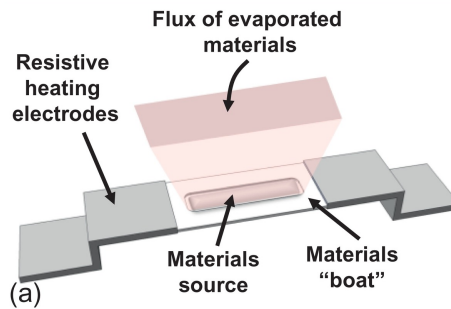


**Figure 3.10:** Schematic of a thermal deposition. The *boat*, by the flowing of a strong electric current, is heated to a temperature where the materials melt and, consequently, evaporate. The materials then condensate and form a thin film deposit on the surface that they hit. Image from [75].

Due to the hygroscopic nature of CsI, its quantum efficiency largely diminishes when in contact with air. To avoid this, the film was deposited on the GEM with it already locked

### 3.4. OPTIMIZATIONS PERFORMED

---

between the metal plates. Everything besides the GEM was covered with a mask for the process. After the CsI evaporation, this component was quickly assembled on the detector ready to go into vacuum.

A 300 nm film thickness was chosen as this value is typically used for reflective photocathode applications [76]. To achieve this, the CsI mass required was calculated: knowing the distance between the GEM and the boat where the CsI crystals are held for evaporation ( $d = 17.65$  cm), the CsI's density ( $\rho_{\text{CsI}} = 4.51 \text{ g} \cdot \text{cm}^{-3}$  [77]) and considering the area subtended by the solid angle of the boat ( $A = \Omega \cdot r^2 = 2\pi r^2$ ), the deposited volume ( $V$ ) at the surface of the GEM can be calculated as:

$$V = 2\pi d^2 t \quad (3.1)$$

where  $t$  is the deposit's thickness. The necessary CsI mass is, then, easily deduced with:

$$M = V \rho_{\text{CsI}} \quad (3.2)$$

If equations 3.1 and 3.2 are merged together,  $M$  becomes:

$$M = 2\pi d^2 t \rho_{\text{CsI}} \quad (3.3)$$

Then, substituting the values, it is possible to obtain  $M = 0,265\text{g}$  as the mass of CsI needed to create a 300 nm thickness deposit.

#### 3.4.3 Vacuum monitoring

A good vacuum is necessary in all gas detectors that do not operate with gas fluxing, i.e., with constant gas flow through the chamber. With the DP-IDC, the different measurements are performed by evacuating all the gas inside the detector until a high vacuum ( $\sim 10^{-6}$  Torr) is reached, with posterior filling with the gas in study.

Studying the vacuum (pressure) evolution over time is a good assessment of the detector's capability of maintaining the gas purity over short and long periods of time.

There are two main contributors for the ultimate vacuum<sup>2</sup> reachable: outgassing<sup>3</sup> from the detector's walls and small gas leaks. What differs in these two is that, while a gas leak continuously contributes for the absolute pressure of a detector (limiting the reachable vacuum), the detector's outgassing stabilizes over time (as long as the detector is not opened).

---

<sup>2</sup>Ultimate vacuum is defined as the lowest pressure that is repeatedly reached in a vacuum system [78].

<sup>3</sup>Outgassing is the release of a gas that was frozen, trapped or dissolved into a given material.

Since several modifications were applied to this detector, there was the need to re-open it several times thus spoiling the overall cleanness achieved inside it. For this reason (and other time constraints), a detailed study evaluating the detector's cleanness over time could not be performed. Nonetheless, while doing measurements, the best vacuum achieved and time needed to reach such value was monitored.

It was found that the detector would reach lower pressures and at a faster rate day after day which indicates a satisfying cleaning over day and the absence of major gas leaks. While measuring the pressure raise during the night (when the vacuum pumps are turned off with the detector remaining closed), it was noticed that the pressure would grow less and less everyday. This means that the pressure raise was mainly caused by the detector's outgassing, which tends to stabilize. After several weeks, the pressure increase during the night stabilized to a few tenths of Torr. At this point, the detector's limit is presumably reached and better conditions would only be possible with great improvements in all the vacuum system and detector's components.

Still concerning the ultimate vacuum, it should be noted that several precautions were taken in order to enhance this value such as frequently tightening all the system's screws (as they usually get looser with extended periods of time and common maneuver) and general search for small gas leaks with acetone and alcohol in several connections.

## 3.5 Preparatory studies

Before starting to take relevant data, it was important to study several of the setup's parameters to avoid retaking data or unnecessarily using resources and time. However, it was not possible to predict all the important factors that influence the signal before taking data, causing some of these factors to be tuned along the way.

This preparatory studies consisted in the examination of not only parameters such as the voltage applied on the GEM but also, for instance, the investigation of the gas quality evolution with time or the impact of pressure variations on the time of arrival spectra.

The results of these tests were often compared with the ones obtained with the previous detector designed by the group [70] and used in the last few years for the measurement of positive ion mobilities, as the design of both detectors is very similar. For this reason, the behaviour of this new detector is also expected to be very similar to the previous one.

Several of these tests were carried out using  $\text{SF}_6$  (as electronegative gas) as this was the most important gas being studied in this thesis thus making it the obvious gas to be used for the chamber's characterization.

#### 3.5.1 Lamp signal

The lamp signal, as referred in sections 3.1 and 3.3.1, plays a crucial role in the development of the acquired signal by acting as a trigger to the oscilloscope and, consequently, working as starting point ( $t = 0$ ) for the time of arrival spectra.

The lamp, itself, has a pulse duration of around 500 ns but the signal acquired by the oscilloscope is always bigger than this value. This happens because what is seen in the oscilloscope is actually an electronic response of the detector and pre-amplifier circuit to the electrical discharge in the lamp when it emits the Xe UV photons. This induced signal is, very likely, affected by several components of the whole system, including geometry factors.

Nonetheless, to have a better understanding of the lamp signal's behaviour, several tests were performed to identify the differences in this signal when using either the top or the bottom part of the detector. The results were then compared to the ones previously obtained with this prototype (section 3.3.1) and to the ones obtained in the chamber used for positive ions [70] in order to single out which elements would indeed affect this signal.

It is presented, in figure 3.11, two raw spectra of the lamp signal using the top and bottom parts of the detector. The spectra shown were obtained in vacuum and with a very low electric field to avoid electric discharges since the chamber was empty. The features shown were observed to be present in all the measurements for different gases, reduced electric fields and pressures. This further confirms the intrinsic nature of the lamp induced signal in the setup.

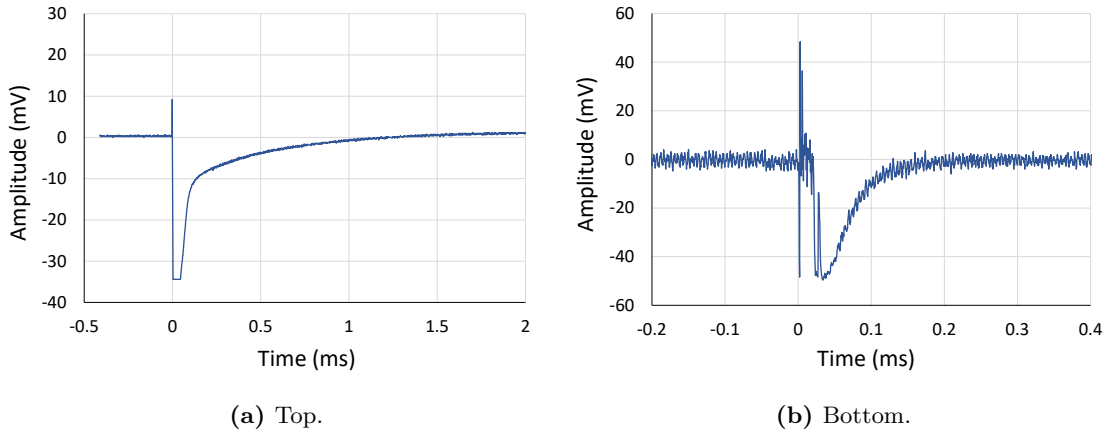


**Figure 3.11:** Spectra of the lamp signal obtained when using either the (a) top or (b) bottom part of the detector.

As we can see in figure 3.11, while, in the bottom side, the lamp induces a signal of around 100  $\mu$ s, in the top part, it induces a signal of almost 1000  $\mu$ s.

The signal produced by the arrival of the ions to the collection grid is expected to be of the order of hundreds of microseconds. This means that if one wants to use the top part

### 3.5. PREPARATORY STUDIES

of the detector, the ions' signal will be superimposed on the lamp's induced signal which will make the measurement very hard to perform (visible in figure 3.12a) while if one uses the bottom side of the detector, this issue will not affect the measurements so strongly.

Another aspect that reinforces the good performance of the bottom part versus the upper one is that the ions induce a signal with different polarity depending on the side of the detector that is used since the ions themselves have different polarity. In this case, the negative ions, which are collected in the bottom part, generate a positive signal while the positive ions (collected in the top) generate a negative signal, i.e., with the same polarity as the lamp's induced signal. This can be seen in figure 3.12.

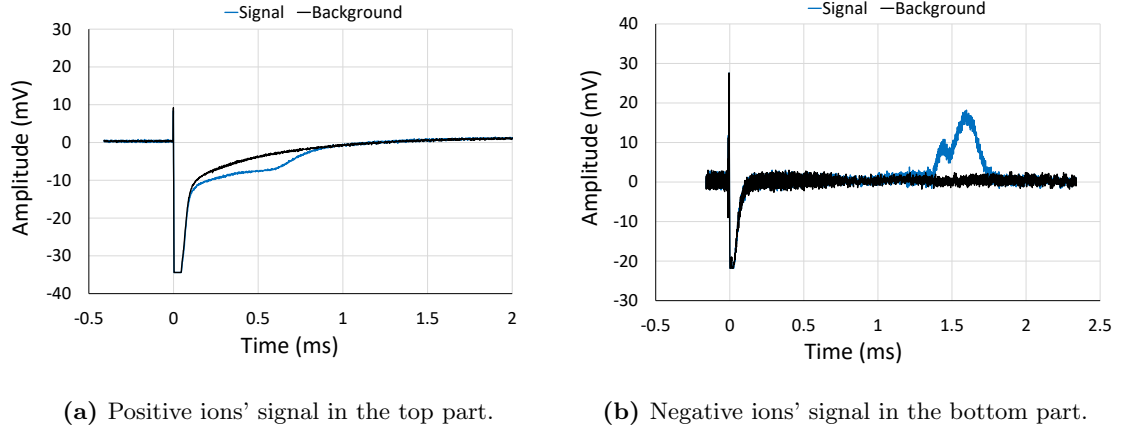


**Figure 3.12:** Two generic spectra of an ions' time of arrival signal using the upper (for positive ions) and bottom (for negative ions) parts of the detector.

Considering that, for all the measurements, the background is subtracted to the signal, one could expect that this issue would not be significant but, as it can be seen in figure 3.12a, the signal for positive ions will always bring a "tail" from the background which makes the measurement less reliable than in figure 3.12b.

Since the nature of this signal is still not fully understood, the next step was to compare these values with the group's previous positive ion chamber: this system usually presents a lamp signal with a width of  $\approx 40 \mu\text{s}$ . The main differences between both detectors is the way how the collection and Frisch grids are assembled. While in the dual polarity detector these two grids have the same area and are separated by a thin Kapton foil of  $50 \mu\text{m}$ , in the single polarity detector the two grids have a smaller coincident area and are separated by a bigger distance.

This led to the belief that this induced signal is a capacitive electronic response of the two grids to the signal emitted by the lamp thus increasing with area and the inverse of distance, following the capacitance formula for a parallel-plate capacitor:

$$C = \epsilon * A/d \quad (3.4)$$

with  $C$  being the capacitance,  $\epsilon$  the medium's permittivity,  $A$  the area and  $d$  the distance between the plates.

Since positive ions have already been thoroughly studied by the group, a deeper study of this capacitance hypothesis was postponed and it was decided that analysing the detector's performance with electronegative gases would be the best course to take, benefiting also from a better background signal which leads to more reliable data. Positive ions were briefly studied only as a tool to evaluate the detector's performance.

#### 3.5.2 Evolution of the spectra with time

A measurement with this system is usually carried out by making vacuum in the chamber, filling it with a specific gas or mixture, applying electric fields both in the drift region and in the GEM, and finally acquiring the signal obtained in the oscilloscope for posterior analysis. After this, the gas inside the chamber is typically evacuated again until a vacuum of the order of  $\sim 10^{-6}$  Torr is reached. This procedure is repeated several times for different pressures and reduced electric fields.

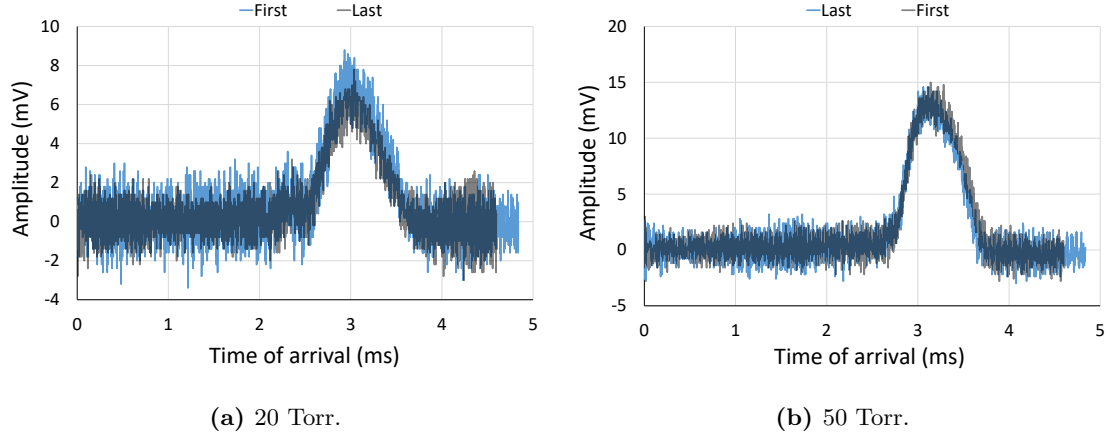
This gas exchange is a regular executed practice in order to ensure a good gas quality as the gas purity is expected to degrade after sometime due to outgassing from the detector's walls and other components. This might be a reasonable procedure when working with only low pressures but, at higher pressures, this method should be revised as unnecessary spending of resources should always be avoided.

For this reason, and since an extensive amount of tests and measurements were performed, a few analysis were carried out to assess the evolution of the signal with time, i.e., understand if the gas purity remains acceptable after the gas being inside the detector for a not negligible (few minutes) period of time, in several different conditions.

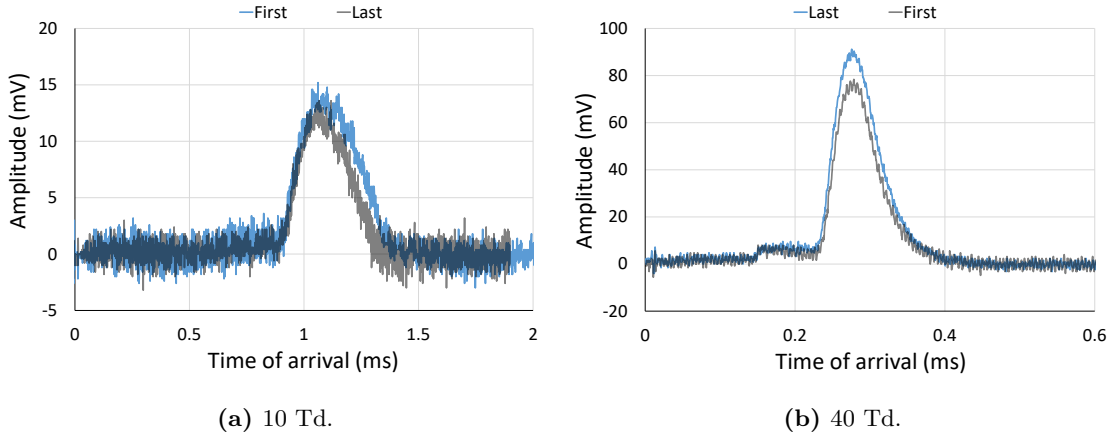
In figures 3.13, 3.14 and 3.15, it is possible to see the analysis made in three different configurations exploring, respectively, different pressures, reduced electric fields and timings.

Figure 3.13 intends to show the difference in the signal when the detector is consecutively filled or evacuated with gas (in this case pure  $\text{SF}_6$ ) following the ranges 20→50 Torr and 50→20 Torr, respectively. The series show the signals obtained for 20 and 50 Torr when these pressures were either the first or the fourth (last) measurement of the run. The consecutive filling or evacuation of the chamber took around 15 minutes.

The same procedure as for the pressure was carried out but for different reduced electric fields and the gas mixture  $\text{SF}_6:\text{N}_2$ . Figure 3.14 shows the results obtained for 10 Td and 40 Td when increasing and decreasing the voltages applied thus making 10 Td either the first or the last (4<sup>th</sup>) measurement of the run and vice-versa for 40 Td. The consecutive increase or decrease of the fields applied took around 5 minutes.



**Figure 3.13:** Two spectra of negative ions' time of arrival signals using pure  $\text{SF}_6$  at two different pressures when these pressures were either the first or the last measurement of the run while, respectively, filling or evacuating the chamber. The grey series has a transparency factor so that the coincidence is more visible.



**Figure 3.14:** Two spectra of negative ions' time of arrival signals using the mixture  $\text{SF}_6:\text{N}_2$  in the ratio 10:90 at 10 Torr and at different reduced electric fields when these values were either the first or the last measurement of the run. The grey series has a transparency factor so that the coincidence is more visible.

Figure 3.15 shows the differences in the signals when taken in different instants after the chamber is fully filled to the requested pressure. For this test, all the components (including electric field, GEM and Xe UV lamp) were turned on during the whole trial. Once again, the detector was filled with 20 Torr of pure  $\text{SF}_6$ .

After carefully analysing figures 3.13, 3.14 and 3.15, one can see that the results remain practically unchanged for considerable amounts of time. It is possible to see a few differences in the signal's amplitude, especially in figure 3.14b, but this difference is not relevant as the interest in these spectra is not the amplitude but rather the  $x$  axis (time that the ions took to travel through the detector from the point where they were created (GEM) until they reach the collection grid) and it is possible to see that the peaks are always

### 3.5. PREPARATORY STUDIES

---

centered in the same values.

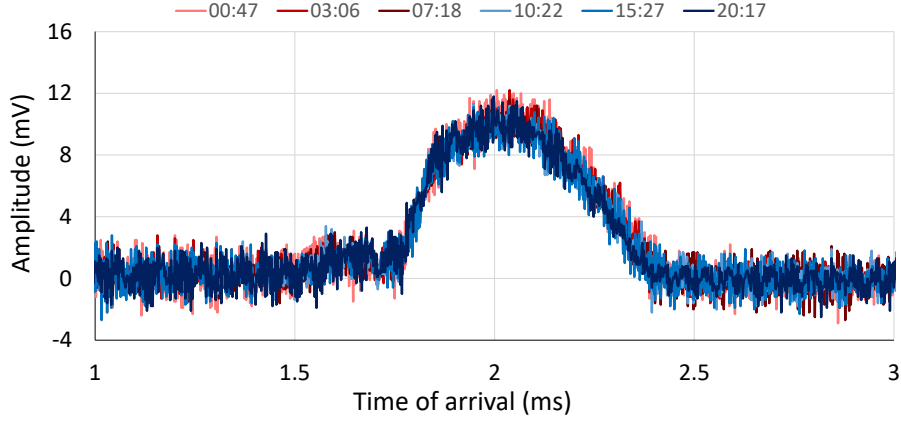


**Figure 3.15:** Spectra of negative ions' time of arrival signals using pure  $\text{SF}_6$  at 20 Torr. The different series represent several signals taken at different instants (mm:ss) without evacuating the chamber and with  $t = 0$  being the moment when the detector's filling was complete.

Although all these different tests were carried out with the same purpose (searching for any dependence of the signal with time), by exploring all these different configurations we also ensured that none of these parameters influence the gas purity or bring any kind of hysteresis to the results.

After these studies, it is possible to conclude that the gas can be maintained in the detector for periods of time up to 30 minutes instead of needing to be constantly replaced. This quick study was rather useful as, from this point onward, the gas was maintained inside the detector for different measurements thus substantially reducing the amount of gas wasted and the time needed for different studies with the detector. However, the procedure of changing the gas was kept in several occasions to ensure good statistical relevance in the measurements. Moreover, the procedure of sequentially raising and lowering the pressure and the reduced electric field was also adopted to, once again, improve the statistical quality of all the tests.

#### 3.5.3 Pressure study

Ion mobilities are often presented normalized to the total number of particles inside the chamber so, when measuring the velocity of ions in a specific uniform reduced electric field, the values obtained should, in theory, be very similar for a wide range of pressures. This is true for a reasonable range of pressures since the main differences arise when comparing low pressures (tens of Torr) to atmospheric (760 Torr) or even higher pressures. The problem of working with higher pressures is the occurrence of secondary reactions between the drifting ions and the gas molecules. These interactions originate ions species different from the originally formed ones and are behind the appearance of ion clusters as it is easier for the ions to bundle together if the number of particles inside the chamber is larger. A



### 3.5. PREPARATORY STUDIES

thorough study on this subject for the gas  $\text{SF}_6$  can be read in [79] where ion clusters up to  $(\text{SF}_6)_9^-$  were found.

The Dual-Polarity Ion Drift Chamber was built to withstand several bars of pressure but the amount of voltage needed to create reduced electric fields usually applied in gas detectors (such as 20 Td) at these pressures would be of the order of tens<sup>4</sup> of kV, being difficult to have such voltages applied without having electrical discharges in the chamber. For this reason, the actual pressures that the whole system can endure fall in the tens of Torr. Moreover, the formation of ion clusters in  $\text{SF}_6$  is expected for gas pressures above 100 Torr [79] so, by working at pressures bellow 100 Torr, the presence of ion clusters drifting in the chamber is not expected.

A study concerning the effects of the pressure in the overall signal was conducted to infer if the signal could be improved by rising the pressure up to 50 torr. Figure 3.16 shows the results obtained when using pure  $\text{SF}_6$  with 10 Td for different pressures and at a constant temperature.

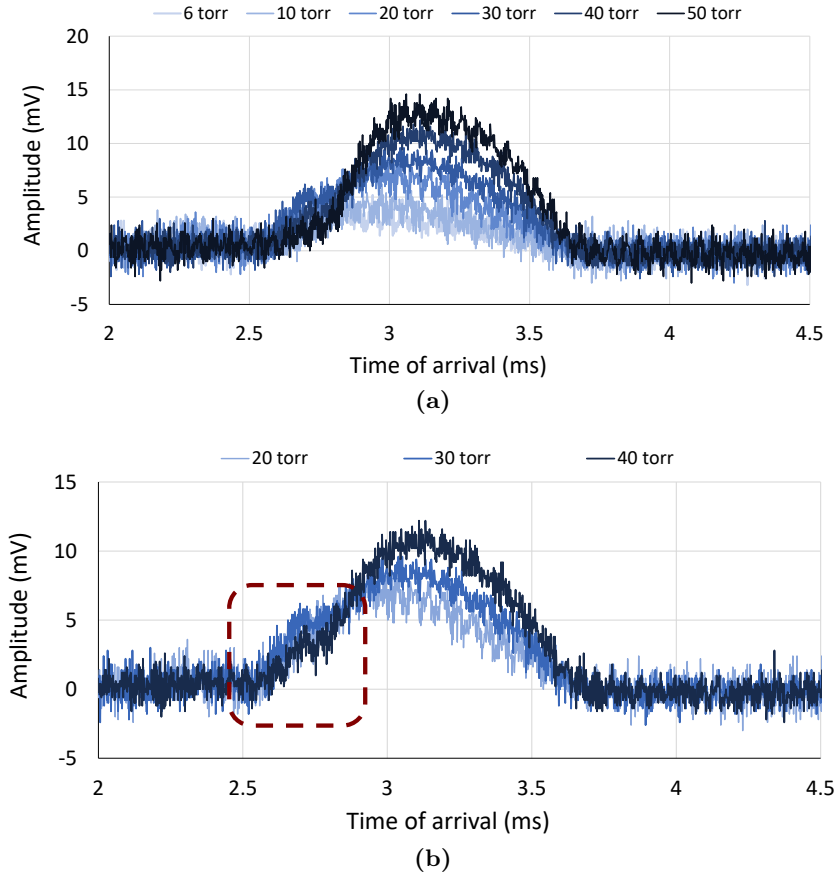


**Figure 3.16:** Time of arrival spectra obtained for (a) different pressures and (b) three specific pressures where a secondary peak (marked in red) appears. These measurements were performed within the same conditions - pure  $\text{SF}_6$  and 10 Td.

<sup>4</sup>25 kV are needed for 20 Td at 1 bar and 5 cm of drift.

It can be seen, in figure 3.16a, that increasing the pressure favours the formation of ions as the signal grows, in amplitude and area, with the pressure. This matches the theory since it is clear that if there are more molecules inside the chamber, the creation of ions will be easier thus leading to a larger (in width and amplitude) signal.

Moreover, since the reduced electric field was kept equal for all the pressures, the peak's centroid remains the same which leads to similar ion mobilities, as expected. This feature will be further addressed in the following sections where the results of the ion mobilities obtained are expressed.

Comparing figures 3.16a and 3.16b, it can also be seen that in the mid range pressures (20, 30 and 40 Torr) there is a smaller peak to the left of the main one that is not visible for higher pressures (50 torr) and lower pressures (below 20 Torr), whose origin will be explained later in section 3.5.4. For further studies with  $\text{SF}_6$ , it was decided that the pressures to be used would be 20 and 30 Torr. Pressures above 40 Torr were discarded for the moment as they would require much higher voltages for the same reduced electric fields.

#### 3.5.4 GEM study

As mentioned before (in section 3.1), the GEM in this setup is not meant to work as a gas electron multiplier but rather as an ion producer. Furthermore, the voltage applied to the GEM should be enough to originate ions, but not high enough to trigger charge and ion multiplication processes that would originate space charge effects, usually resulting in the degradation of the signal.

So, it was important to verify the effects of the voltage applied across the GEM on the signal. The first test, shown in figure 3.17, was conducted with pure  $\text{SF}_6$  at a pressure of 10 Torr and a reduced electric field of 20 Td.

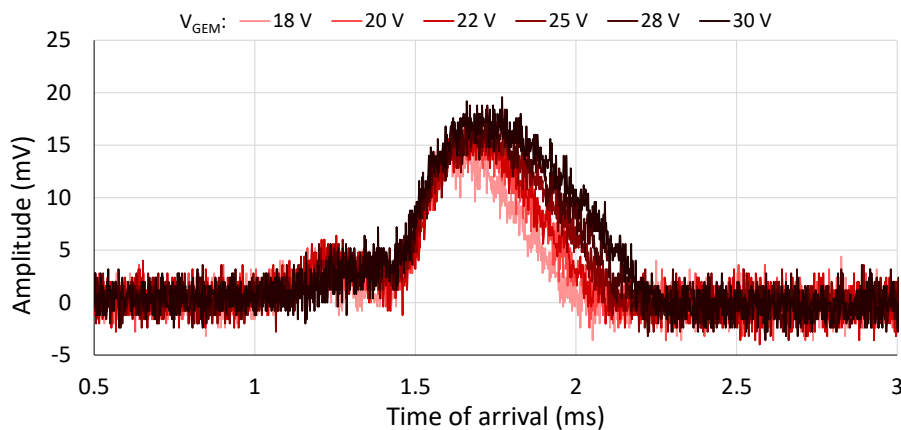


**Figure 3.17:** Time of arrival spectra obtained for different voltages applied across the GEM and with 10 Torr of pure  $\text{SF}_6$  at 20 Td.

### 3.5. PREPARATORY STUDIES

Figure 3.17 shows an expected behaviour: with the increase of the voltage across the GEM, the signals become wider but their centroids remain unaffected. Since having a higher electric field in the GEM's holes increases the probability of ions being created, we believe that the space charge effect due to the accumulation of ions near the GEM could distort the electric field in this region leading to a broader ion time of arrival spectrum.

A wider signal does not bring any usefulness as we are mostly interested on the peaks' centroids and a wider signal means a poorer resolution on these centroids. So, a voltage of 22 V across the GEM was chosen.

Following this study and with the knowledge of the pressure effect on the signal, a similar test was carried out but now with 20 Torr of pressure and a reduced electric field of 20 Td. The results of this test can be seen in figure 3.18. The same test was performed with a pressure of 30 Torr but no significant difference was found.

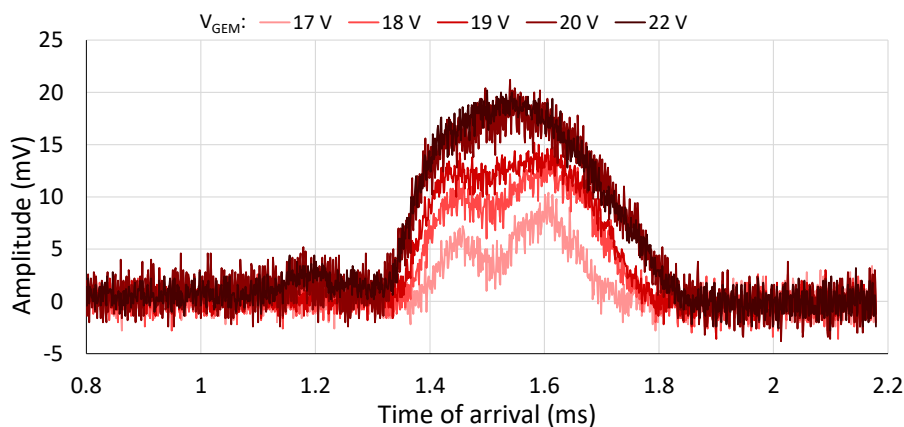


**Figure 3.18:** Time of arrival spectra obtained for different voltages applied across the GEM and with 20 Torr of pure  $\text{SF}_6$  at 20 Td.

Throughout this more precise study (in figure 3.18) it was possible to see that the increase of the voltage across the GEM makes the two peaks merge into only one. This study allowed to clearly identify the two expected peaks from the  $\text{SF}_6$  molecule, i.e., the  $\text{SF}_6^-$  and  $\text{SF}_5^-$  ions. This revealed to be a major breakthrough because it allowed for the explicit confirmation of the preliminary expectations that the peak observed in previous studies was indeed composed by two individual peaks.

While doing this study, higher voltages across the GEM were also explored to detect eventual new features. The results are presented in a different chart (figure 3.19) for better visualization.

As it can be seen in figure 3.19, for smaller voltages (brighter colors), there seems to be a new peak appearing while the main one remains equal in size. This suggested a new and unexpected species of ion being formed within the detector which was later analysed and found to be, most likely,  $\text{SF}_4^-$ .

### 3.5. PREPARATORY STUDIES

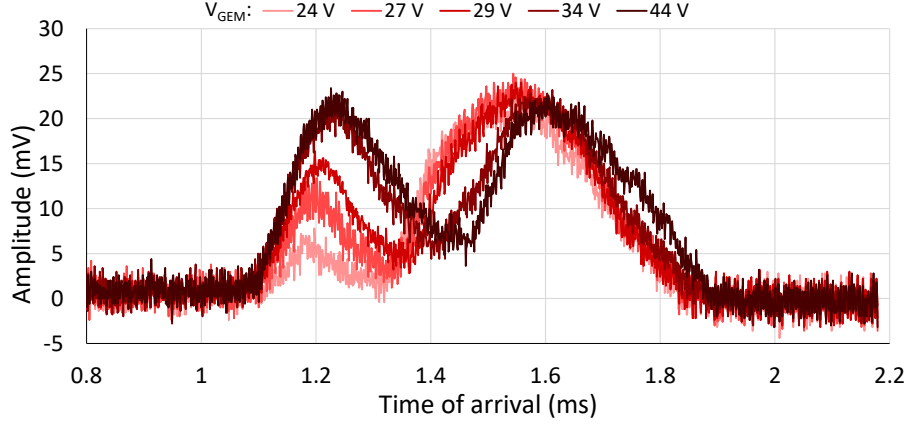


**Figure 3.19:** Time of arrival spectra obtained for different voltages applied across the GEM with 20 Torr of pure  $\text{SF}_6$  at 20 Td.

One can also notice that for much higher voltages (34 and 44 V), the first (and new) peak becomes much bigger while our previous main peak becomes smaller in area and even changes in shape. This leads to the thought that this new physical process is overcoming and replacing the creation of the ion  $\text{SF}_5^-$ .

To have a numerical comprehension of the relation between the several identified peaks' areas with the growth of the voltage applied, a quick analysis with the data presented in the previous charts was carried out. The results of this analysis can be seen in figure 3.20.

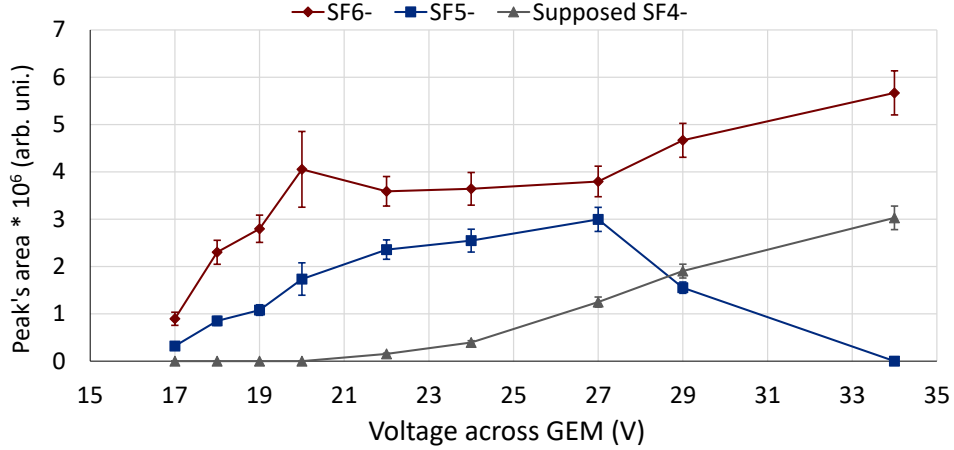


**Figure 3.20:** Evolution of the 3 ion peak's areas with the voltage applied on the GEM.

As it can be seen in figure 3.20, when starting to raise the voltage, both peaks corresponding to the  $\text{SF}_6^-$  and  $\text{SF}_5^-$  ions start to grow evenly. Between 22 and 27 V, a new peak (supposed to be  $\text{SF}_4^-$ ) starts to appear and the other two keep growing. At 29 V there is a sharp change: at this point, the physical process that creates  $\text{SF}_4^-$  overcomes the processes

that form  $\text{SF}_5^-$  while not affecting the spawn of  $\text{SF}_6^-$  ions. This effect persists up to all the greater voltages tested.

Looking at figure 3.21, it is possible to see that  $\text{SF}_6$  has a very low energy threshold for the formation of its main negative ions: 0.001 and 0.0001 eV for, respectively,  $\text{SF}_5^-$  and  $\text{SF}_6^-$ . However, the cross-sections for the creation of these anions by electron attachment rapidly decrease with the increasing electron energy.

For higher electron energies, figure 2.13 shows that, at  $\sim 3.5$  eV, the cross section of the formation of  $\text{SF}_6^-$  and  $\text{SF}_5^-$  tends to very low values while for cross sections for the formation of  $\text{F}^-$  and  $\text{SF}_4^-$  start to be significant. This could partially explain the appearance of a new peak in the spectra of figure 3.19. This is further explored in section 4.3.

The changes observed in the areas of the identified peaks in figure 3.20 show that, besides a new peak appearing, the area of the  $\text{SF}_5^-$  ion also starts to decrease. To understand this feature, one needs to look at equations shown in section 2.7.4.1 and studies such as [68]. Although no clear explanation for this feature is given, one could guess that, due to collisional processes at higher electron voltages, a certain amount of  $\text{SF}_5^-$  ions could be converted into  $\text{SF}_4^-$ . Deeper studies in this matter should be carried with the DP-IDC to better understand this feature and the overall underlying processes of ion formation in  $\text{SF}_6$ .

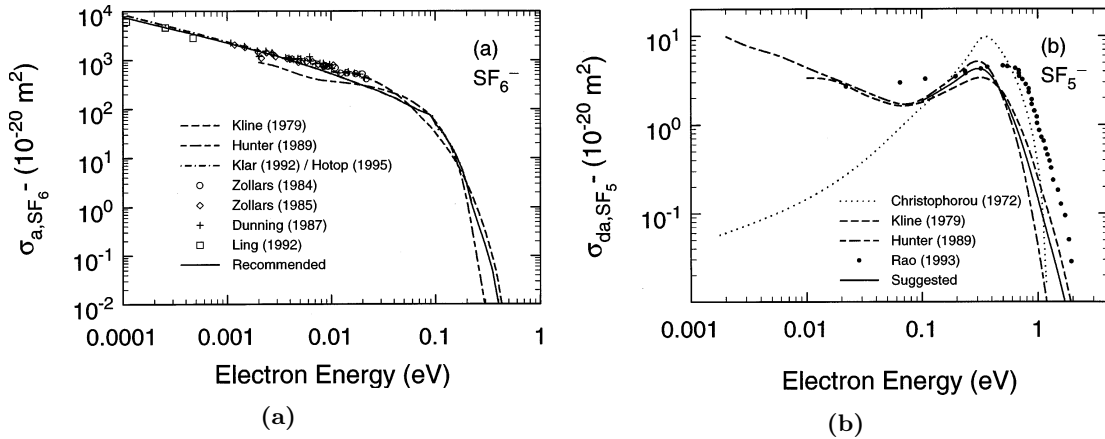


**Figure 3.21:** Electron attachment and dissociative electron attachment cross sections for the formation of, respectively,  $\text{SF}_6^-$  (a) and  $\text{SF}_5^-$  (b), as a function of the electron's energy. Retrieved from [68].

In sum, this study allowed for the understanding of the great impact that the voltage applied on the GEM brings to the measurements. On one hand, it influences the detector's resolution by either widening or narrowing the signals obtained. On the other hand, it affects the ion species created within the chamber. For these reasons, the choice of the voltage to be applied on the GEM will depend on the gas used and the physics case of the experiment/study.

### 3.5.4.1 Importance of the electric field in the GEM

The voltage applied on the GEM is one of the most important aspects influencing the processes that occur in the holes of the GEM since it is directly related with the energy gained by the electrons in these holes. When applying 30 V on a GEM, an electron crossing its holes would gain an energy of 30 eV if it crossed the whole hole without interacting/colliding with any gas atom/molecules, which does not happen. In fact, what will actually happen is that electrons will gradually accelerate until the point where they have enough energy to interact with the gas thus losing its current energy before reaching the end of the GEM.

By considering the particular case of  $\text{SF}_6$  (see section 2.7.4.1) and looking at figure 3.21, we could be led to believe that only a very low voltage across the GEM is needed to originate these negative ions. This is not in agreement with the spectra obtained and presented in figure 3.18. We concluded that, if there is not a sufficient voltage across the GEM, the electric field in its holes will not be strong enough to pull the electrons released by the CsI photocathode on top of the GEM thus restraining the consequent ion formation. So, lowering the voltage across the GEM too much would result in a very suppressed signal which would not be visible with this system. Hence, an optimal operating voltage should be studied for each particular case.

### 3.5.5 Drift distance and error bars

As mentioned in the beginning of the chapter, one of the interesting aspects of using ions instead of electrons as information carriers is the fact that ions thermalize much faster than electrons. This means that ions reach an equilibrium state (*steady-state*) between collisions and acceleration (due to the electric field) in smaller distances than electrons do. At this steady-state, ions closely follow the field lines of the electric field at an approximately constant speed, being this velocity the parameter we intend to measure.

For this reason, this detector was built symmetrically to the point where the GEM is placed in order to ensure a 5 cm drift for each side. With 5 cm, we expect the ions to reach a steady-state as the authors in [79], for slightly higher pressures ( $\sim 200$  Torr), concluded that a minimum distance of 3 cm is needed to obtain a mobility independent of the drift distance for  $\text{SF}_6$  ions.

After the modifications performed in the detector (section 3.4), the drift distance was changed to 4.8 cm for negative ions (bottom part) and 5.2 cm for positive ions (top part). In fact, after several measurements, it was found that this difference embodies a significant source of error in the calculation of the ions reduced mobility as a slight change in the drift distance originates meaningful differences in the results obtained for the ion mobility. This was solved by correcting the drift distance for each case in the analysis software.

The error of the reduced ion mobilities obtained was calculated through the error propagation formula where, for a given ion mobility  $K_0(d, \Delta t, \Delta V, P, T)$  obtained with equation

2.18, the uncertainty in the measurement ( $\delta K_0$ ) is given by equation 3.5 :

$$\delta K_0 = \sqrt{\sum_i^n \left( \frac{\partial K_0}{\partial x_i} \delta x_i \right)^2} = K_0 \sqrt{\left( \frac{2 \cdot \delta d}{d} \right)^2 + \left( \frac{\delta \Delta t}{\Delta t} \right)^2 + \left( \frac{\delta \Delta V}{\Delta V} \right)^2 + \left( \frac{\delta P}{P} \right)^2 + \left( \frac{\delta T}{T} \right)^2} \quad (3.5)$$

with  $d$  being the drift distance,  $\Delta t$  the centroid of the Gaussian fit applied to the time of arrival spectrum,  $\Delta V$  the voltage applied to create the electric field,  $P$  the pressure and  $T$  the temperature.

For the calculation of  $\delta K_0$ , the following uncertainties were assumed:

- $\delta d = 1$  mm - measurement error.
- $\delta \Delta t = 1\text{-}10\%$  of  $\Delta t$ , depending on the signal. This assumption is based on the reliability of the Gaussian fitting program which, in some cases, would produce significantly different fits for different initial parameters.
- $\delta \Delta V = 1$  V - instrument error.
- $\delta P = 0.02$  Torr. This is not the instrument error but rather the pressure error allowed in each measurement since the gas input procedure is performed manually.
- $\delta T = 0.1$  K - instrument error.

From the calculation of  $\delta K_0$  in several different configurations of pressures and reduced electric fields, it was found that  $\delta d$  and  $\delta \Delta t$  are the major contributors for the error in the ion mobilities obtained with the other uncertainties being practically negligible.

Another possible source of error could be the *electron capture mean-free-path* which is the distance travelled by the electron before being captured by the  $\text{SF}_6$  molecule. This value was found to be about 1 to 10 micrometers for a setup similar to the one presented in this thesis [12]. Considering that the GEM used has a  $50 \mu\text{m}$  Kapton thickness, a capture mean-free-path of  $10 \mu\text{m}$  can be dismissed for the error estimation as it represents only a small fraction (1 %) of the uncertainty in the drift distance (1 mm) and 0.02 % of the total drift distance ( $\sim 5$  cm).

#### 3.5.6 Conclusions of the preparatory studies

To summarize all the tests carried out, it was found that the lamp's induced signal is clearly wider in the top part of the detector (used for positive ions) compared to the bottom part (used for negative ions) which reinforced the idea of focusing the work on the study of negative rather than positive ions, in an initial stage.

### 3.5. PREPARATORY STUDIES

---

It was also found that the gas purity does not significantly degrade inside the detector in periods of time up to around 30 minutes which allowed faster data taking.

The pressure influence was also found to not be entirely crucial for the measurements but it was decided that pressures above 20 Torr should be used as the signals obtained with these pressures are significantly better.

Concerning the voltage applied on the GEM, this value should be studied for each individual gas or mixture as the signal obtained might significantly differ with the voltage. Nonetheless, in a broader sense, one can point to voltages between 15 and 30 V as being acceptable as it guarantees electrons with enough energy to ionize a wide range of gases since the first ionization energies are, usually, below 30 eV. It also ensures that there is a sufficiently strong electric field in the GEM to pull the electrons released from the CsI photocathode.



## Chapter 4

# Experimental results

After the efforts dedicated to the enhancement of the signal obtained with the DP-IDC, the next phase was to test its behaviour and performance in different gas mixtures containing  $\text{SF}_6$ , for different pressures and electric fields. To do this, studies were carried out to infer if the detector could acquire the correct time of arrival spectra that would, later, give the reduced mobilities of the ions in several gases and mixtures. This chapter presents the experimental results obtained for these studies and the subsequent analysis and discussion, together with the comparison between these results and the ones previously obtained for these gases. With these studies, it was possible to access the accuracy of the experimental setup.

### 4.1 Data analysis process

Before presenting the final results obtained with this detector, it is important to briefly explain the analysis process. This process can be subdivided in two steps: *Time of arrival spectrum acquisition* and *Ion identification*.

#### 1. Time of arrival spectrum acquisition

- (a) After the ions are created, drifted and collected on the grids, the electric signal originated is passed to the oscilloscope through a pre-amplifier. The signal obtained - which corresponds to an average of 128 time of arrival spectra - is saved. Right after the measurement, the GEM is turned off and the background is also recorded. Both signals are then analysed by a script which subtracts the background to the signal and plots the result.
- (b) Possible peaks in the spectrum are identified. For instance, in figure 3.17, the shape of the peak leads to the assumption that there are actually two peaks merged together. This assumption comes from the fact that the peak does not show the expected symmetry of a Gaussian shape, with the rising being much faster than the falling.

- (c) After identifying the possible peaks, the user suggests parameters for the script to fit Gaussian curves to the spectrum. After the script finishes the analysis, a fit is presented for the given spectrum with the identified peaks and the corresponding parameters. An example of these fits can be seen in figure 4.1.
- (d) The most important parameter obtained is the centroid of the peak which corresponds to the *average drift time* of the ions. With these values and following equation 2.18, it is possible to calculate the reduced mobility of the ions.

## 2. Ion identification

- (a) With the values of the reduced ion mobilities for the different identified peaks, the possible ion candidates are determined. This is done by studying which are the expected processes between the gas molecules and consulting the cross-sections for these processes. With this, it is possible to understand and determine which are the possible formed ions within the gas and their relative proportions. For this, the voltage across the GEM also needs to be known to understand the range of energies acquired by electrons while they cross it and collide with the gas molecules.
- (b) Knowing the candidates, it is now possible to calculate the theoretical mobility of such ions resorting to the Langevin Limit and Blanc's law (equations 2.21 and 2.23).
- (c) Then, it is only necessary to portray all the information gathered in a single plot and it should be possible to precisely identify which ions are being created and collected by the detector.

Note: In the whole ion identification process, the literature should also be consulted whenever it is possible as it usually contains important information regarding ion formation processes and ion mobilities. Additionally, it is rather crucial to look into the validity of the Langevin Limit for the gas in study as it often diverges from the experimental values obtained. This will be clearer once the results are shown and compared with the theoretical values.

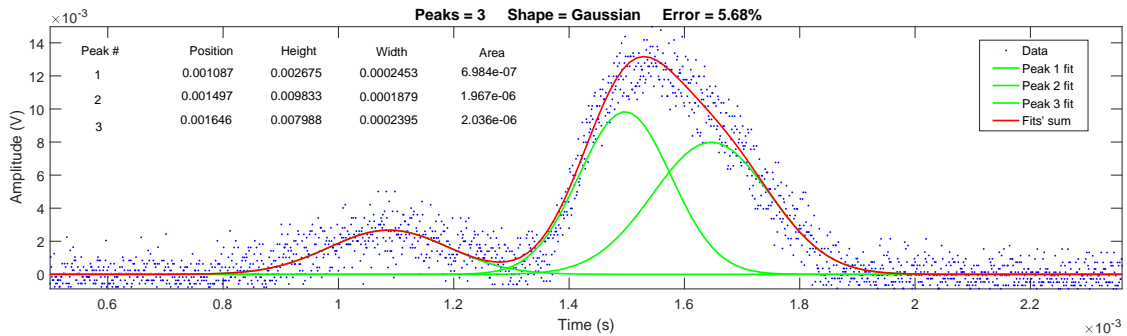


**Figure 4.1:** Example of the analysis performed in a raw acquired signal (*Data*, in blue). The red line (*Fits' sum*) is the sum of the Gaussian fits performed (3 in this case). A good fit is achieved when the red line closely follows the blue dots. In this case, 3 Gaussian curves - corresponding to 3 different ion species - were found.

## 4.2 Ne-CF<sub>4</sub> Mixture

During the course of this thesis, besides improving and testing the DP-IDC, I have also put a considerable amount of time and effort in the study of positive ion mobilities with the detector that was being used by the group during the last few years [70], here designated IDC (Ion drift chamber). This allowed me to better understand important features of the IDC which granted me the expertise needed to upgrade the DP-IDC and obtain the first results with negative ion drift that match the literature.

While working with the IDC, the mobility of the positive ions present in the mixture Ne-CF<sub>4</sub> was measured, in the pressure range of 8-12 Torr and reduced electric fields between 15 and 25 Td. This ultimately resulted in a published work [80].

Since the DP-IDC was build with the intention of being an upgrade of the IDC, the first measurements with the DP-IDC were focused in obtaining the same results as the IDC by measuring positive ion mobilities. In order to do this, the first mixture used was Ne-CF<sub>4</sub>, in several ratios and similar pressures and reduced electric fields. The mobilities obtained with both detectors were then directly compared. The results of these two studies are shown in figure 4.2.

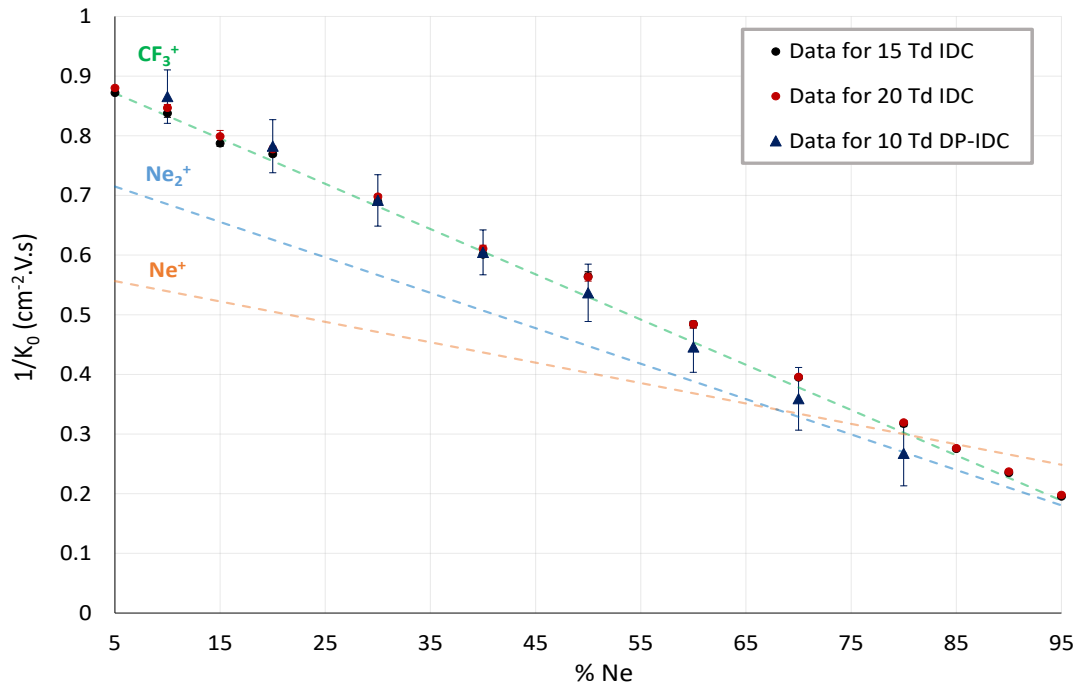


**Figure 4.2:** Reduced mobility of the positive ions observed in Ne-CF<sub>4</sub> in different ratios for 15 Td (black) and 20 Td (red) at pressure of 8 Torr, obtained with the IDC [80]. In blue, the results obtained with the DP-IDC for 10 Td and 20 Torr with the same gas. The dash lines represent the expected ions that can be formed within the mixture and their expected mobilities throughout Blanc's law.

Figure 4.2 shows several features regarding the measurement of the positive ions in Ne-CF<sub>4</sub>:

- For the mixture Ne-CF<sub>4</sub>, the main ion created is CF<sub>3</sub><sup>+</sup> as the mobilities obtained closely follow the Blanc’s law prediction for this ion. This is further confirmed in table 4.1 where it is shown that the most probable reaction in this gas results in the creation of CF<sub>3</sub><sup>+</sup>. The results obtained with the DP-IDC are also in agreement with this hypothesis for percentages of Neon up to 60 %. For higher percentages, although still within the error bars, the results are inconclusive for the determination of the ions created within the chamber.
- Using different pressures (8 against 20 Torr) and different reduced electric fields (10/15 against 20 Td) in the measurements with the two detectors, we can observe that these did not show any significant difference in the mobilities acquired thus confirming the assumption that the ion mobility is independent of these factors in the ranges studied.
- The increase of the ion mobility with the increase of the percentage of Ne used in the mixture, visible in the results presented, was also expected due to the lower mass of Ne compared to the CF<sub>4</sub> molecule.
- At last, the results obtained with the DP-IDC closely follow the published results obtained with the IDC up to 50 % on Ne in the mixture, with the major discrepancy being of 18.4 % at 80 % of Ne. The substantially large error bars are attributed to the overlap of the ion’s time of arrival signals with the lamp induced signal, feature explored in section 3.5.1, that is more pronounced as the %Ne increases in the mixture, since the drift time decreases. This overlap hardens the process of fitting Gaussian curves to the spectra which, in return, produces large fluctuations on the determination of the fit’s centroid.

**Table 4.1:** Reactions involving the Ne<sup>+</sup> ion and the molecule CF<sub>4</sub> and their ionization product distribution and respective rate constants. Adapted from [81].

Reaction	Prod. dist.	Rate const. (10 <sup>-10</sup> cm <sup>3</sup> · s <sup>-1</sup> )
Ne <sup>+</sup> + CF <sub>4</sub> → CF <sub>3</sub> <sup>+</sup> + F + Ne	0.955	1.34 ± 0.40
Ne <sup>+</sup> + CF <sub>4</sub> → CF <sub>2</sub> <sup>+</sup> + 2F + Ne	0.045	

### 4.3 Pure SF<sub>6</sub>

As referred in section 2.7.4.1, SF<sub>6</sub> is one of the most used gases for the study of negative ions as information carriers for several reasons with one of them being its very high electronegativity which makes it very easy to create negative ions from this gas. The fact that this is big a molecule also strongly reduces the possibility of sparks within the detector in comparison to noble gases as it works as "its own" quenching gas (see section 2.6).

### 4.3. PURE SF<sub>6</sub>

From figure 2.13, it is expected that the main ions present are SF<sub>6</sub><sup>-</sup> and SF<sub>5</sub><sup>-</sup> in a similar proportion but with SF<sub>6</sub><sup>-</sup> being slightly more dominant, for the electrons' energies used. This is well reported in [12] where it is also mentioned that changes in parameters such as the temperature and electron energies might invert this ratio.

Other ions originated from SF<sub>6</sub> such as SF<sub>n</sub><sup>-</sup> (n=4,3,2) and F<sup>-</sup> could also be considered [68] but, due to their much lower cross-sections and higher energy thresholds, these are not expected at the applied GEM voltages. Furthermore, as we progressively accelerate the electrons from rest energy to a maximum of  $\approx 30$  eV (voltage applied on the GEM), the electrons, while gaining energy, will most likely interact with SF<sub>6</sub> producing SF<sub>6</sub><sup>-</sup> and SF<sub>5</sub><sup>-</sup> before acquiring enough energy to trigger any other process.

Although high pressures are preferred in most common applications, as already referred, the first measurements performed with pure SF<sub>6</sub> were focused on very low pressures (6 - 10 Torr) since the experimental system is not, yet, prepared to go to higher (hundreds of Torr) pressures.

In all the measurements, several reduced electric fields were explored ranging from 10 to 40 Td and the temperature of the room was established to around 24 °C. Figure 4.3 shows a typical spectrum obtained with pure SF<sub>6</sub> at a pressure of 20 Torr and an E/N of 25 Td, where the two main ions produced are visible. Figure 4.4 shows the results of this first experiment, conducted for different reduced electric fields (E/N) and for pressures ranging from 6 to 10 Torr.

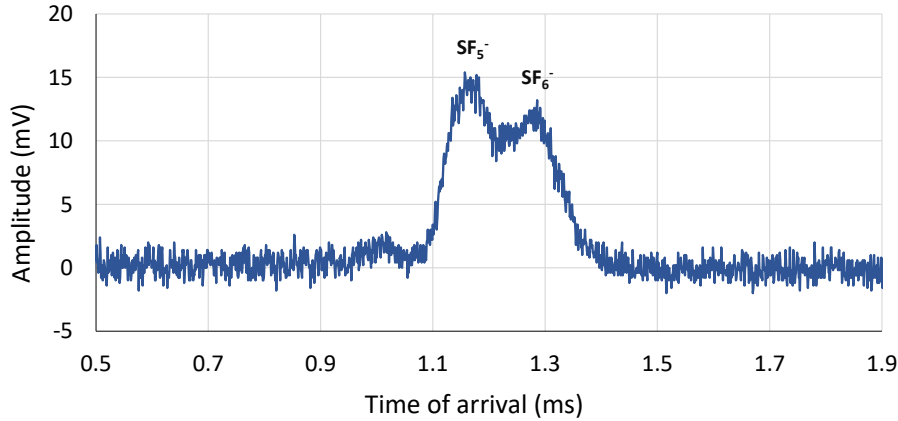


**Figure 4.3:** Typical spectrum obtained when using pure SF<sub>6</sub>. The two main ions produced (SF<sub>5</sub><sup>-</sup> and SF<sub>6</sub><sup>-</sup>) are visible and identified. This spectrum was obtained at a pressure of 20 Torr and an E/N of 25 Td.

As referred, higher pressures were proved to enhance the signal obtained. For this reason, a follow-up study was carried out but with higher pressures (20 and 30 Torr). Within this study, a new time of arrival peak was found thus a new negative ion species possibly identified. The results of this study are presented in figure 4.5.

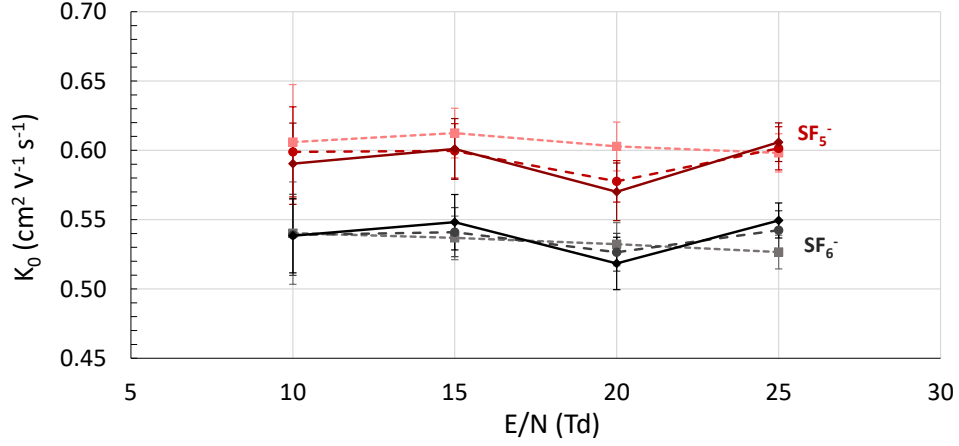


**Figure 4.4:** Ion mobility values obtained for several reduced electric fields and pressures: 6 Torr (■), 8 Torr (●) and 10 Torr (◆). The two colors (red and gray) represent the two separate time of arrival peaks identified in each spectrum and for which the ions  $\text{SF}_5^-$  and  $\text{SF}_6^-$  were attributed. The voltage applied on the GEM was of 22 V.

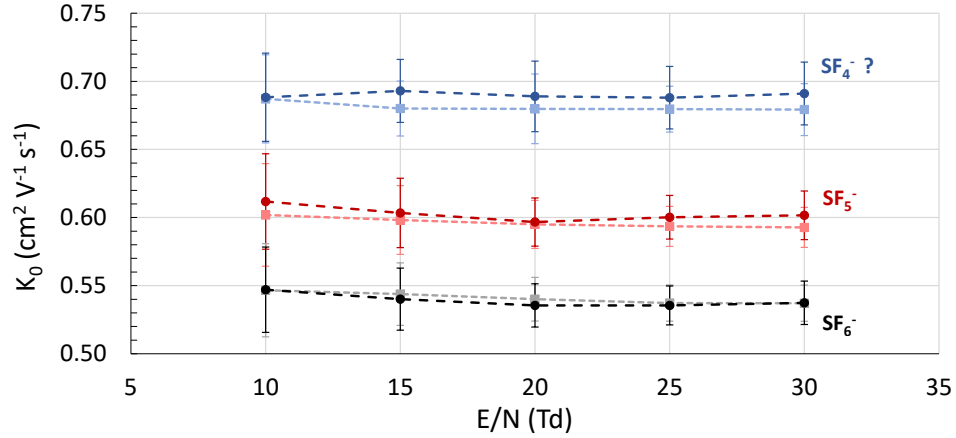


**Figure 4.5:** Ion mobility values obtained for several reduced electric fields and pressures: 20 Torr (■) and 30 Torr (●). As in figure 4.4, the two same ions ( $\text{SF}_5^-$  and  $\text{SF}_6^-$ ) are represented. These values were obtained with a voltage across the GEM of 18 V. In blue, the new peak identified, possibly corresponding to  $\text{SF}_4^-$ , is shown. The data for this ion was obtained using a higher voltage across the GEM (35 V).

In both cases shown (figures 4.4 and 4.5), there are several notable aspects: on one hand, the mobility of all the ion species identified do not substantially change in the pressure range considered as expected from the theory and confirmed in the literature [79]. On the other hand, the mobility of these ions also does not change in the range of reduced electric fields studied, fact also in agreement with existing results in the literature [82, 83].

#### 4.4. SF<sub>6</sub>-CF<sub>4</sub> MIXTURE

---

Since this setup does not comprehend an absolute ion identification method (such as, for example, a mass spectrometer), the ion species were identified to be SF<sub>5</sub><sup>-</sup> and SF<sub>6</sub><sup>-</sup> by cross checking the results obtained with several available sources ([12, 82, 83, 84, 85, 86]) where the reported values for the mobilities of the ions SF<sub>5</sub><sup>-</sup> and SF<sub>6</sub><sup>-</sup> are, on average, respectively, 0.595 and 0.542 cm<sup>2</sup> V<sup>-1</sup> s<sup>-1</sup>. These values are well within the error margin of the results obtained with the DP-IDC thus supporting an initial satisfactory performance.

Furthermore, these values differ substantially from the theoretical ones: when using the Langevin Limit (eq. 2.21), an ion mobility for SF<sub>6</sub><sup>-</sup> in SF<sub>6</sub> of 0.635 cm<sup>2</sup> V<sup>-1</sup> s<sup>-1</sup> is obtained. This happens due to the fact that the Langevin Limit is strictly applicable to mono-atomic systems solely under the influence of point-charge induced dipole interaction potentials and well below 300 K [83].

As for the ion represented in blue in figure 4.5 and visible in the spectra of figure 3.19, its nature was not fully disclosed. As we can see in figure 2.13, there are several ion species that could be generated from a system with pure SF<sub>6</sub>, but after the ones already confirmed, the ions F<sup>-</sup> and SF<sub>4</sub><sup>-</sup> are the most likely ones to be formed with F<sup>-</sup> having the greatest cross section. F<sup>-</sup>, due to its very low mass, is expected to show much higher mobilities, fact also confirmed by the literature [85]. Although SF<sub>4</sub><sup>-</sup> (and other ions with lower number of Fluorine atoms) is a possible product of SF<sub>6</sub>, the mobility of the SF<sub>4</sub><sup>-</sup> was not found to be reported in the literature. For this reason, the expected mobility value for SF<sub>4</sub><sup>-</sup> was calculated resorting to the Langevin Limit formula (eq. 2.21). The value obtained for the low-field mobility of SF<sub>4</sub><sup>-</sup> in SF<sub>6</sub> was 0.688 cm<sup>2</sup> V<sup>-1</sup> s<sup>-1</sup> (using a dipole polarizability of 6.55 Å<sup>3</sup> [87] for the SF<sub>6</sub> molecule). This falls very well within the results obtained in this experiment although it is not possible, at this point, to indisputably confirm the presence of SF<sub>4</sub><sup>-</sup>.

#### 4.4 SF<sub>6</sub>-CF<sub>4</sub> Mixture

With the spectra of pure SF<sub>6</sub> already studied, the next step was to test the detector with gas mixtures which include SF<sub>6</sub>. For this and the following study, only the two very well known peaks (SF<sub>6</sub><sup>-</sup> and SF<sub>5</sub><sup>-</sup>) were studied as these two are, with high degree of certainty, known to be present when SF<sub>6</sub> is used. Furthermore, the spectra obtained was, in most cases, very similar to the one presented in figure 4.3.

For this test, the mixture SF<sub>6</sub>-CF<sub>4</sub> was used in several ratios (10, 20, 40 and 60 % of SF<sub>6</sub>), different reduced electric fields (15-30 Td) and at a constant pressure of 20 Torr and temperature of ≈ 24 °C. The GEM's voltage found to grant the best signal was 15 V. The main intent of this study was to confirm the results of [88]. Figure 4.6 shows the results obtained with DP-IDC as well as the results obtained in [88].

In figure 4.6, it is possible to see that, when using 60% of SF<sub>6</sub> (green), the data obtained follows quite closely the published results. This match between the two data is not so visible for other percentages of SF<sub>6</sub>: for 40% of SF<sub>6</sub> (blue), there is a relative average deviation of 3.73% whereas for 20% of SF<sub>6</sub> (red), an average relative deviation of 6.05% is found.

#### 4.4. SF<sub>6</sub>-CF<sub>4</sub> MIXTURE

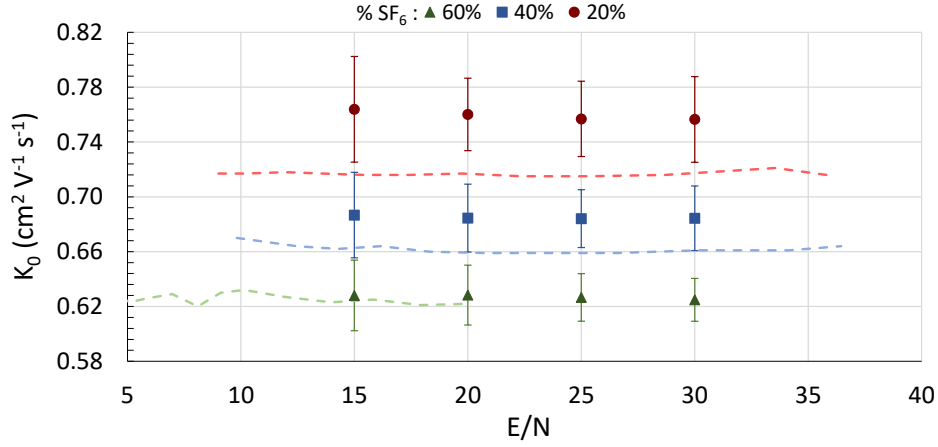


**Figure 4.6:** Ion mobility of  $\text{SF}_6^-$  obtained for several different percentages of  $\text{SF}_6$  and reduced electric fields, at 20 Torr. The points ( $\bullet$ ,  $\blacksquare$  and  $\blacktriangle$ ) represent the data obtained. The dashed lines represent the data in the literature [88], with the colors corresponding to the same %  $\text{SF}_6$  studied.

To understand the source of this difference, the same results were plotted against the Blanc's law prediction (equation 2.23). To do this, the values of the low-field mobilities of  $\text{SF}_6^-$  in  $\text{CF}_4$  and in  $\text{SF}_6$  used were, respectively, 0.825 [88] and 0.542  $\text{cm}^2 \text{V}^{-1} \text{s}^{-1}$ . For the  $\text{SF}_5^-$  ion, its low-field mobility in  $\text{CF}_4$  is not reported so it was calculated using the Langevin limit (equation 2.21) with which a value of 0.980  $\text{cm}^2 \text{V}^{-1} \text{s}^{-1}$  was obtained. When in  $\text{SF}_6$ , the ion  $\text{SF}_5^-$  has a mobility of 0.595  $\text{cm}^2 \text{V}^{-1} \text{s}^{-1}$ . The results of the comparison between the data obtained and Blanc's prediction can be seen in figure 4.7.

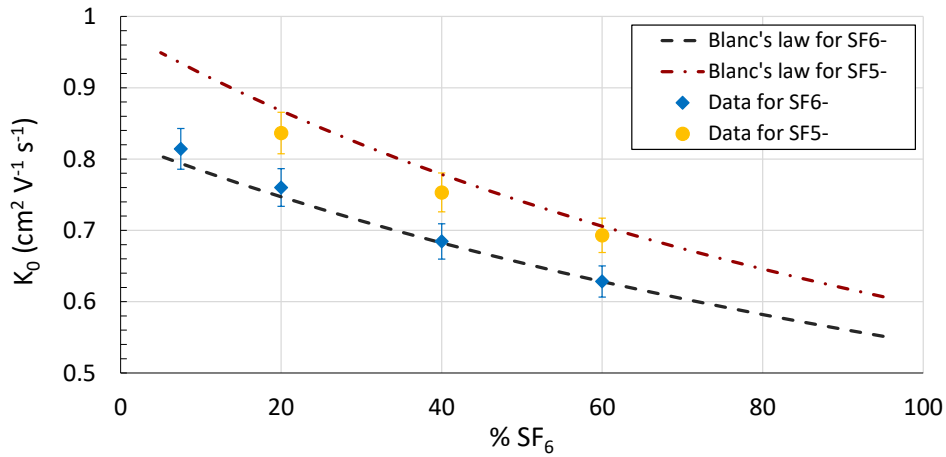


**Figure 4.7:** Ion mobility of  $\text{SF}_6^-$  and  $\text{SF}_5^-$  obtained for several different percentages of  $\text{SF}_6$  at 20 Torr and a  $E/N$  of 20 Td. The points ( $\blacklozenge$  and  $\bullet$ ) represent the data obtained. The dashed lines represent the Blanc's law prediction for the mobilities of  $\text{SF}_6^-$  and  $\text{SF}_5^-$  in the mixture  $\text{SF}_6\text{-CF}_4$ .

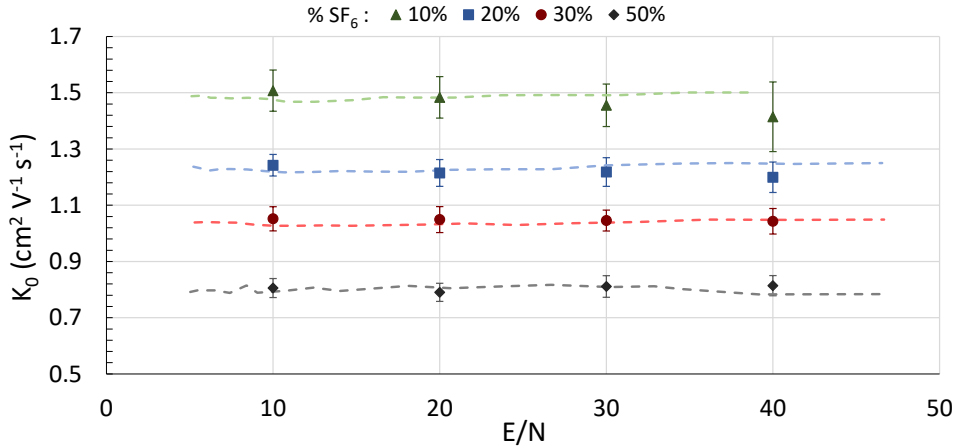


Figure 4.7 shows that, although the absolute mobilities obtained differ from the literature, they follow with great agreement the expected values by Blanc's law, with the major deviation observed being 3.7% for the ion SF<sub>6</sub><sup>-</sup> at 20% of SF<sub>6</sub>. For this reason, this experiment was considered to be successful with the detector achieving results very close to the expected ones.

## 4.5 SF<sub>6</sub>-N<sub>2</sub> Mixture

Similarly, another study was conducted but using a much smaller molecule, i.e., using N<sub>2</sub> instead of CF<sub>4</sub>. Just by comparing both molecules, it is already possible to conclude that the mobilities to be found will be considerably greater as N<sub>2</sub> is much lighter and smaller than CF<sub>4</sub>.

This test complied reduced electric fields in the range 10 to 40 Td and percentages of SF<sub>6</sub> from 10 to 50 %. The pressure was set to 10 Torr with the temperature settling at  $\approx 25$  °C. The voltage applied to the GEM was 22 V. Likewise with CF<sub>4</sub>, the objective was to compare the results with the ones presented in [89]. Figure 4.9 shows the results of this study.



**Figure 4.8:** Ion mobility of SF<sub>6</sub><sup>-</sup> obtained for several different percentages of SF<sub>6</sub> and reduced electric fields, at 10 Torr. The points (●, ■, ▲ and ◆) represent the data obtained. The dashed lines represent the data present in the literature [89], with the colors corresponding to the same % SF<sub>6</sub> studied.

With the mixture SF<sub>6</sub>-N<sub>2</sub> (figure 4.8), the results obtained follow closely the results published proving a very good detector performance. Only when using 10 % of SF<sub>6</sub>, the results seem to start diverging from the expected ones with a maximum relative error of 5.7% being found at 40 Td. This noticeable discrepancy is attributed to the fact that very low quantities of SF<sub>6</sub> are much harder to guarantee as a slight error in the gas input will considerably change the ratio between the gases inside the chamber thus the larger error

bars in the 10% SF<sub>6</sub> series. Another visible feature found in these (green series) particular spectra was a large tail in the signals which forces the Gaussian fit to be centered more to the right, i.e., at longer times of arrival which, in return, results in a lower ion mobility that can explain the decrease seen in the figure for 40 Td. This feature also enlarged the error bars.

To increase the level of confidence of the values obtained, Blanc's law prediction was again calculated for SF<sub>6</sub><sup>-</sup> and SF<sub>5</sub><sup>-</sup>. The value used for the low-field mobility of SF<sub>6</sub><sup>-</sup> in N<sub>2</sub> was 1.89 cm<sup>2</sup> V<sup>-1</sup> s<sup>-1</sup> [89]. For SF<sub>5</sub><sup>-</sup> in N<sub>2</sub>, this value was calculated using the Langevin Limit which resulted in a low-field mobility of 2.20 cm<sup>2</sup> V<sup>-1</sup> s<sup>-1</sup>. The mobilities of SF<sub>6</sub><sup>-</sup> and SF<sub>5</sub><sup>-</sup> in SF<sub>6</sub> used were the ones obtained in the previous measurements, i.e., 0.542 and 0.595 cm<sup>2</sup> V<sup>-1</sup> s<sup>-1</sup>, respectively. The results of the comparison between the data acquired and Blanc's law is shown in figure 4.9.

To be noted that the value 1.89 cm<sup>2</sup> V<sup>-1</sup> s<sup>-1</sup> can be approximately obtained by reducing the percentage of SF<sub>6</sub> in the mixture to very low values. This was the procedure followed in [89] where percentages of SF<sub>6</sub> in the range 0.02 to 0.1 % were used. It is important to refer that this precision is not attainable with this setup for the pressures used.

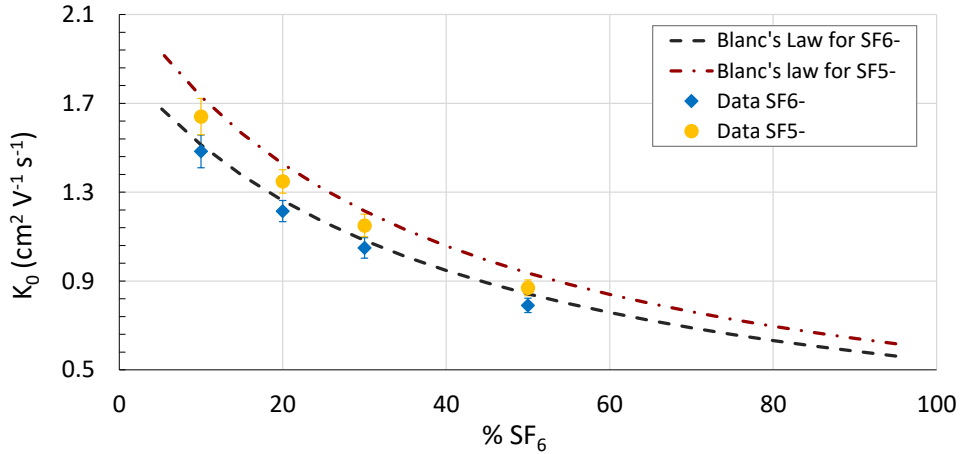


**Figure 4.9:** Ion mobility of SF<sub>6</sub><sup>-</sup> and SF<sub>5</sub><sup>-</sup> obtained for several different percentages of SF<sub>6</sub> for 20 Td at 10 Torr. The points (♦ and ●) represent the data obtained. The dashed lines represent the Blanc's law prediction for the mobilities of SF<sub>6</sub><sup>-</sup> and SF<sub>5</sub><sup>-</sup> in the mixture SF<sub>6</sub>-N<sub>2</sub>.

By analysing figure 4.9, it is possible to see that the ion reduced mobilities obtained for SF<sub>6</sub><sup>-</sup> and SF<sub>5</sub><sup>-</sup> follow the Blanc's law prediction with the major deviation being found for SF<sub>5</sub><sup>-</sup> where an average relative error of 5.81% is present. These results reinforce the ions identification system and the detector's good performance.

## 4.6 Discussion

Within all the spectra analysed, there were always two peaks identified corresponding to  $\text{SF}_5^-$  and  $\text{SF}_6^-$ . Their areas would slightly differ depending on the conditions but  $\text{SF}_6^-$  always showed the greatest area between both peaks thus confirming the initial assumption that the majority drifting ion is, indeed,  $\text{SF}_6^-$  in both mixtures and pure  $\text{SF}_6$ . The detector also proved to be able to distinguish both  $\text{SF}_5^-$  and  $\text{SF}_6^-$  peaks, in the right conditions, which is a major breakthrough as it allows the thorough study of these ions which, in result, will support other studies focused on events fiducialization resorting to  $\text{SF}_6$  mixtures.

An unexpected peak was often seen with a much smaller amplitude. The visualization of this peak was enhanced by raising the voltage applied to the GEM, consequently degrading the previous visible peaks of  $\text{SF}_5^-$  and  $\text{SF}_6^-$ . The nature of this apparent new ion was dubious as data present in the literature did not offer conclusive options or explanations. After taking a more theoretical approach by using the Langevin Limit, it was found that the ion species  $\text{SF}_4^-$  should have a similar reduced mobility to the one obtained thus the assumption that this detected peak was, indeed,  $\text{SF}_4^-$ . To confirm this hypothesis, deeper studies should be conducted in the future exploring the relation between the area of this peak with the voltage applied on the GEM and by trying to observe this peak in mixtures with  $\text{SF}_6$  which will allow the direct comparison of such results with Blanc's Law.

Concerning the comparison of the results obtained with the predicted ones, Blanc's law seems to fit very well for the data obtained thus emphasizing the detector's accuracy and confirming the identity of the ions detected. For the calculation of Blanc's law, experimental values are often preferred in contrast with Langevin Limit as the latter is formulated for very specific conditions and does not take in account phenomena such as the formation of ion clusters and charge transfers between ions and molecules. It is also for this reason that, in both figures 4.7 and 4.9, the data obtained for  $\text{SF}_5^-$  diverges more from Blanc's prediction than  $\text{SF}_6^-$  since, without the values of low-field mobilities of  $\text{SF}_5^-$  in  $\text{N}_2$  and  $\text{CF}_4$ , Blanc's law cannot be applied so accurately. Nonetheless, with an observed deviation of only 3.7% for  $\text{CF}_4$  and 5.81% for  $\text{N}_2$ , it is possible to confirm the presence of both ions in the chamber.

In all the measurements, the ion mobilities are fairly independent of the pressures and reduced electric fields used as expected in the ranges studied.

It was also possible to thoroughly understand the impact of several parameters of the system in the signal acquired which, on one hand, allowed for much faster and accurate measurements and, on the other hand, opened the horizons for the importance of the study of each of these parameters which, in the long run, will allow other interesting and exotic studies.

Concerning the measurement of positive ion mobilities, there are, still, several improvements to be done in order to reduce the width of the lamp's induced signal with the interest of obtaining clear time of arrival signals which will lead to an unambiguously identification of the observed ions. The main changes to be carried out are expected to be focused on

## 4.6. DISCUSSION

---

reducing the capacitance between the Frisch and collection grids. Nonetheless, the cation mobilities obtained are within the expected, although more tests need to be conducted to prove the capability and accuracy of the chamber when measuring positive ion mobilities.

## Chapter 5

# Conclusions

The measurement of ion mobilities has been gaining great relevance in the past few decades since it strongly influences the performance of large volume detectors. The appearance of the Negative Ion Time Projection Chambers has further propelled this interest as, in this detectors, the negative ions are the information carriers, thus making their mobility a key feature of these detectors' performance.

This shift from electron to ion drift is motivated by the much smaller diffusion presented by ions which allows for much better spatial resolutions thus a greater track reconstruction capability. The other great advantage of the use of negative ions as information carriers is the recently discovered ability of determining the absolute  $z$  coordinate of an ionizing event just by analysing the drift time of the different minority ion species created within the chamber. This new method of obtaining a trigger-less measurement is of great interest for rare event experiments such as Dark Matter and neutrinoless double beta decay searches.

For such experiments, although the knowledge of the mobility and diffusion of different negative ions is a key element, others factors that influence ion mobility are also relevant. In these, one can highlight the ion polarizabilities, the effects of the electric field and pressure in the motion of ions, and the formation of ion clusters within the gas or with water molecules, which can reduce the mobility of the ions observed or induce wrong measurements due to their different mass (and mobility).

The Dual-Polarity Ion Drift Chamber was designed to support many of the studies concerning ion motion by being able to measure both positive and negative ion mobilities. Such measurements are achieved by measuring the drift time of the ions under uniform electric fields and in different pressures.

The first prototype revealed some technical issues concerning its performance and the measurement of ion mobilities that did not correspond to the values published in the literature. Such incoherence was attributed to the non-uniform electric field near the GEM and large width of the lamp induced signal. To overcome this issue, a new GEM base was designed and implemented and with which we confirmed, by simulation, that a

very uniform electric field was achieved in the whole sensitive region of the chamber.

Although the constraints found concerning the lamp signal in the upper part of the chamber, a study of the mobility of positive ions in the mixture Ne-CF<sub>4</sub> was carried. To better access the accuracy of these measurements, the same study was performed with a similar chamber developed by P. Neves [70]. The results obtained with both ion drift chambers were compared and found to be in agreement, with the main ion created being CF<sub>3</sub><sup>+</sup> and with its mobility also following the literature fairly well.

The several preparatory studies carried prior to the actual measurements were very important to better understand several features of this chamber: On one hand, it was found that the ion mobilities obtained over long periods of time ( $\sim 30$  minutes) did not change leading to the conclusion that the gas purity remains fairly constant for that period of time. On the other hand, while testing the pressure influence on the signal, it was found that a pressure of 20 Torr is preferred over 50 Torr as a different time of arrival peak was found only at 20 Torr. While changing the voltage applied to the GEM, it was possible to observe an enlargement of the time of arrival peaks to a point where two peaks were no longer distinguishable. This feature is thought to be caused by the accumulation of ions in the GEM holes, distorting the electric field in this region, i.e., space charge effects. For much higher voltages, different ions started to appear within the chamber which later pointed to, possibly, the minority ion SF<sub>4</sub><sup>-</sup>, thus proving the key role of the voltage applied to the GEM in systems like the DP-IDC.

When observing and measuring the mobility of the ions created in gas mixtures containing SF<sub>6</sub>, it was found that these were well within the expected, following closely the theoretical values given by the empirical Blanc's law as well as several studies with the same gases. Such results are a good indication that the modifications introduced in the GEM supporting structure were useful in correcting for the non-uniformities of the electric field in the drift region, that were seen to affect the very first results obtained with the present experimental system.

Considering the results presented in this thesis regarding the performance assessment of the Dual-Polarity Ion Drift Chamber, it is possible to conclude that the detector shows a good performance, with the results standing well within the expected ones comparing both with the theory and with published results. The improved performance achieved with the updated DP-IDC has opened the horizons for many other studies with different gas mixtures comprising different electronegative dopants besides SF<sub>6</sub>, thus further supporting different experiments that exploit negative ion drift in the scope of NITPCs.

## Future work

Despite the promising experimental results here presented, there are some points of concern that should be addressed in the near future and, once corrected, will allow to further improve the performance of this experimental system.

## CONCLUSIONS

---

One of the most important limitations observed in the studies here reported is the lamp induced signal. This signal has proven to negatively affect the detector performance mainly in its upper region, used for the measurement of positive ion mobilities. This issue should be carefully studied in order to better understand its origin: in a first approach, the area and distance between the Frisch and collection grids should be varied in order to verify if the effect observed is, indeed, a capacitance induced signal by the grids or not. A different placement of the lamp, with a better electrical insulation should also be explored. This could easily be the key for a fully functional, wide-range system to assess the different charge transport properties.

The study of other exotic ion species expected to be present should also be pursued since they could affect the performance of large volume detectors. One example is the widely used  $\text{CF}_4$  gas.  $\text{CF}_4$  is expected to generate negative ions by electron attachment [90] but these ions were not seen or measured within the studies carried out with the mixture  $\text{SF}_6$ - $\text{CF}_4$ . This might be due to the fact that the electron attachment threshold energy for  $\text{SF}_6$  is very low (0.1 meV) comparing to  $\text{CF}_4$  ( $\sim 5$  eV [90]) which means that it is very likely for the electron to attach to a  $\text{SF}_6$  molecule while beginning its acceleration before gaining enough energy to attach to the  $\text{CF}_4$  molecule. Further studies with this mixture should be carried out to confirm the presence (or not) of these anions in the chamber.

Another study that might be relevant is the measurement of ion mobilities at higher pressures. This is also being considered within the group as this is of upmost interest for most of the large detector experiments. To increase the pressure, the main difficulty would be the electrical system as higher pressures require higher voltages to maintain the same reduced electric fields. The gas management would also need to be re-thought since high gas purity is essential and operating these kind of detectors in a continuous gas flow would not be viable. This issue can be overcome by using circulatory purification systems or by reinforcing the tightness of the chamber. Moreover, and now under investigation, the use of different feedthroughs is expected to better maintain the gas purity inside the chamber during much longer periods of time, meaning that a higher amount of gas could be maintained inside the chamber without the deterioration of the measurement of ion mobilities due to impurities.

Another possible working method for the DP-IDC would be the *simultaneous* measurement of positive and negative ions. In many studies concerning ion mobility in  $\text{SF}_6$ , both types of ions are found and, with a simultaneous measurement, it would be possible to better understand which ions are being created within the ion drift chamber. Such configuration would only require another pre-amplifier as the DP-IDC electrical system was already designed for this feature.

Furthermore, it is expected that, in the future, longitudinal diffusion studies can also be performed. For that, as an example, a system that allows different drift distances would be needed in order to study the width of the time of arrival spectra obtained for different drift distances. In addition, by replacing the present readout system by a segmented charge readout as, for example, Microstrips, the transverse diffusion could also be accessed. The implementation of an amplification system, such as Micromegas, might also allow the study of the electron strip efficiency of negative ions, which will be essential for NITPCs.

## CONCLUSIONS

---

Besides diffusion, the influence of other factors on the ion mobility such as the presence of impurities (for instance, water vapours), are also of interest and should be attainable with this system.

I believe this system will, with the proper modifications, be an essential tool for the study of many key parameters that influence the motion of ions in gases. This will allow a much better understanding of negative ion drift in different gas mixtures with electronegative dopants, thus pushing forward the use of NITPCs.



# Bibliography

- [1] G. J. Barker, Silicon Vertex Detectors and Particle Identification, Springer Berlin Heidelberg, Berlin, Heidelberg, 2010, pp. 23–35. [doi:10.1007/978-3-642-05279-8\\_2](#).
- [2] H. Tanigawa, K. Adamczyk, H. Aihara, T. Aziz, S. Bacher, S. Bahinipati, G. Batignani, J. Baudot, P. Behera, S. Bettarini, T. Bilka, A. Bozek, F. Buchsteiner, et al., Performance of the Belle II Silicon Vertex Detector, Nuclear Instruments and Methods in Physics Research Section A: Accelerators, Spectrometers, Detectors and Associated Equipment 972 (2020) 164129. [doi:10.1016/j.nima.2020.164129](#).
- [3] F. Sauli, The gas electron multiplier (GEM): Operating principles and applications, Nuclear Instruments and Methods in Physics Research, Section A: Accelerators, Spectrometers, Detectors and Associated Equipment 805 (2016) 2–24. [doi:10.1016/j.nima.2015.07.060](#).
- [4] G. Charpak, J. Derre, Y. Giomataris, P. Rebougeard, MICROMEGAS, a multi-purpose gaseous detector, Nucl. Instrum. Meth. A 478 (2002) 26–36. [doi:10.1016/S0168-9002\(01\)01713-2](#).
- [5] G. Charpak, R. Bouclier, T. Bressani, J. Favier, C. Zupančič, The use of multiwire proportional counters to select and localize charged particles, Nuclear Instruments and Methods 62 (3) (1968) 262 – 268. [doi:10.1016/0029-554X\(68\)90371-6](#).
- [6] C. Martoff, D. Snowden-Ifft, T. Ohnuki, N. Spooner, M. Lehner, Suppressing drift chamber diffusion without magnetic field, Nuclear Instruments and Methods in Physics Research Section A: Accelerators, Spectrometers, Detectors and Associated Equipment 440 (2) (2000) 355 – 359. [doi:10.1016/S0168-9002\(99\)00955-9](#).
- [7] J. Martoff, Negative Ion TPC for WIMP Astronomy, Vol. C0604032, 2006, p. 0188.
- [8] D. R. Nygren, A negative-ion TPC with ultra-high energy resolution for  $0\nu$  double beta decay search in  $^{136}\text{Xe}$ , Journal of Physics: Conference Series 65 (1) (2007). [doi:10.1088/1742-6596/65/1/012003](#).
- [9] C. J. Martoff, R. Ayad, M. Katz-Hyman, G. Bonvicini, A. Schreiner, Negative ion drift and diffusion in a TPC near 1 bar, Nuclear Instruments and Methods in Physics Research, Section A: Accelerators, Spectrometers, Detectors and Associated Equipment 555 (1-2) (2005) 55–58. [arXiv:0406114](#), [doi:10.1016/j.nima.2005.08.103](#).

- [10] E. Daw, A. Dorofeev, J. R. Fox, J. L. Gauvreau, C. Ghag, L. J. Harmon, J. L. Harton, M. Gold, E. R. Lee, D. Loomba, E. H. Miller, A. S. J. Murphy, et al., The DRIFT Dark Matter Experiments (2011). [arXiv:1110.0222](#).
- [11] D. P. Snowden-Ifft, Discovery of Multiple, Ionization-Created Anions in Gas Mixtures Containing CS<sub>2</sub> and O<sub>2</sub> (2013). [arXiv:1308.0354](#).
- [12] N. Phan, R. Lafler, R. Lauer, E. Lee, D. Loomba, J. Matthews, E. Miller, The novel properties of SF<sub>6</sub> for directional dark matter experiments, Journal of Instrumentation 12 (09 2016). [doi:10.1088/1748-0221/12/02/P02012](#).
- [13] CERN, European Council for Nuclear Research, <https://home.cern/>.
- [14] Sergio Armenta and Manel Alcala and Marcelo Blanco, A review of recent, unconventional applications of ion mobility spectrometry (IMS), Analytica Chimica Acta 703 (2) (2011) 114 – 123. [doi:10.1016/j.aca.2011.07.021](#).
- [15] LIP: Laboratory of Instrumentation and Experimental Particle Physics, <http://www.coimbra.lip.pt/>.
- [16] T. N. Collaboration, F. Granena, T. Lux, F. Nova, J. Rico, F. Sanchez, D. R. Nygren, J. A. S. Barata, F. I. G. M. Borges, C. A. N. Conde, et al., NEXT, a HPGXe TPC for neutrinoless double beta decay searches (2009). [arXiv:0907.4054](#).
- [17] Pierre Auger Observatory, <https://www.auger.org/>.
- [18] Chapter 3 - Gas Ionization Detectors, in: Michael F. L'Annunziata (Ed.), Handbook of Radioactivity Analysis (Third Edition), third edition Edition, Academic Press, Amsterdam, 2012, pp. 191 – 231. [doi:10.1016/B978-0-12-384873-4.00003-7](#).
- [19] W. R. Leo, Techniques for Nuclear and Particle Physics Experiments, Springer-Verlag Berlin Heidelberg, 1994.
- [20] D. Malain, P. Kanchana, Evaluation of radiation safety for ionization chamber smoke detectors containing Am-241, Journal of Physics: Conference Series 1285 (2019) 012047. [doi:10.1088/1742-6596/1285/1/012047](#).
- [21] J. M. F. dos Santos, J. A. M. Lopes, J. F. C. A. Veloso, P. C. P. S. Simões, T. H. V. T. Dias, F. P. Santos, P. J. B. M. Rachinhas, L. F. Requicha Ferreira, C. A. N. Conde, Development of portable gas proportional scintillation counters for x-ray spectrometry, X-Ray Spectrometry 30 (6) (2001) 373–381. [doi:10.1002/xrs.510](#).
- [22] C.A.N. Conde and A.J.P.L. Policarpo, A gas proportional scintillation counter, Nuclear Instruments and Methods 53 (1967) 7 – 12. [doi:/10.1016/0029-554X\(67\)91323-7](#).
- [23] P. Rachinhas, P. Simões, J. Lopes, T. Dias, R. Morgado, J. dos Santos, A. Stauffer, C. Conde, Simulation and experimental results for the detection of conversion electrons with gas proportional scintillation counters, Nuclear Instruments and Methods in Physics Research Section A: Accelerators, Spectrometers, Detectors and Associated Equipment 441 (3) (2000) 468 – 478. [doi:10.1016/S0168-9002\(99\)00978-X](#).

- [24] E. Rutherford, H. Geiger, J. Harling, An Electrical Method of Counting the Number of alpha Particles from RadioActive Substances, *Proceedings of The Royal Society A: Mathematical, Physical and Engineering Sciences* 81 (1908) 141–161. [doi:10.1098/rspa.1908.0065](https://doi.org/10.1098/rspa.1908.0065).
- [25] G. F. Knoll, *Radiation detection and measurement*, Wiley, 2010.
- [26] G. D. Chase, J. L. Rabinowitz, *Principles of Radioisotope Methodology*, Burgess Publishing Company, 1967.
- [27] G. Steinhäuser, K. Buchtela, Chapter 2 - Gas ionization detectors, in: M. F. L’Annunziata (Ed.), *Handbook of Radioactivity Analysis (Fourth Edition)*, fourth edition Edition, Academic Press, 2020, pp. 245 – 305. [doi:10.1016/B978-0-12-814397-1.00002-9](https://doi.org/10.1016/B978-0-12-814397-1.00002-9).
- [28] D. A. SCHAUER, A. BRODSKY, J. A. SAYEG, 15 - RADIATION DOSIMETRY, in: M. F. L’Annunziata (Ed.), *Handbook of Radioactivity Analysis (Second Edition)*, second edition Edition, Academic Press, San Diego, 2003, pp. 1165 – 1208. [doi:10.1016/B978-012436603-9/50020-X](https://doi.org/10.1016/B978-012436603-9/50020-X).
- [29] N. Jevtic, V. Drndarevic, Plug and Play Geiger-Muller Detector for Environmental Monitoring, *Instrumentation Science & Technology* 43 (02 2015). [doi:10.1080/10739149.2014.976829](https://doi.org/10.1080/10739149.2014.976829).
- [30] M. E. Rose, S. A. Korff, An Investigation of the Properties of Proportional Counters, *Phys. Rev.* 59 (1941) 850–859. [doi:10.1103/PhysRev.59.850](https://doi.org/10.1103/PhysRev.59.850).
- [31] T. Z. Kowalski, Generalized parametrisation of the gas gain in proportional counters, *Nuclear Instruments and Methods in Physics Research Section A: Accelerators, Spectrometers, Detectors and Associated Equipment* 243 (2) (1986) 501 – 504. [doi:10.1016/0168-9002\(86\)90987-3](https://doi.org/10.1016/0168-9002(86)90987-3).
- [32] A. Winkler, A. Karadzhinova, T. Hilden, F. García, G. Fedi, F. Devoto, E. Brücken, A gaseous proportional counter built from a conventional aluminum beverage can, *American Journal of Physics* 83 (09 2015). [doi:10.1119/1.4923022](https://doi.org/10.1119/1.4923022).
- [33] R. Alfaro, Construction and operation of a small multiwire proportional chamber, *Journal of Physics: Conference Series* 18 (2005) 362–367. [doi:10.1088/1742-6596/18/1/011](https://doi.org/10.1088/1742-6596/18/1/011).
- [34] A Oed, Properties of micro-strip gas chambers (MSGC) and recent developments, *Nuclear Instruments and Methods in Physics Research Section A: Accelerators, Spectrometers, Detectors and Associated Equipment* 367 (1) (1995) 34 – 40, proceedings of the 7th International Wire Chamber Conference. [doi:10.1016/0168-9002\(95\)00657-5](https://doi.org/10.1016/0168-9002(95)00657-5).
- [35] F. Hartjes, B. Hendriksen, J. Schmitz, H. Schuijlenburg, F. Udo, Operation of the microstrip gas detector, *Nuclear Instruments and Methods in Physics Research Section A: Accelerators, Spectrometers, Detectors and Associated Equipment* 310 (1) (1991) 88 – 94. [doi:10.1016/0168-9002\(91\)91003-E](https://doi.org/10.1016/0168-9002(91)91003-E).

- [36] A. Barbosa, C. Rickel, P. Wattecamps, Two-dimensional X-ray detector based on microstrip and multiwire design, Nuclear Instruments and Methods in Physics Research Section A: Accelerators, Spectrometers, Detectors and Associated Equipment 323 (1) (1992) 247 – 251. [doi:10.1016/0168-9002\(92\)90297-H](https://doi.org/10.1016/0168-9002(92)90297-H).
- [37] F. Sauli, GEM: A new concept for electron amplification in gas detectors, Nuclear Instruments and Methods in Physics Research Section A: Accelerators, Spectrometers, Detectors and Associated Equipment 386 (2) (1997) 531 – 534. [doi:10.1016/S0168-9002\(96\)01172-2](https://doi.org/10.1016/S0168-9002(96)01172-2).
- [38] R. Chechik, A. Breskin, C. Shalem, D. Mörmann, Thick GEM-like hole multipliers: properties and possible applications, Nuclear Instruments and Methods in Physics Research Section A: Accelerators, Spectrometers, Detectors and Associated Equipment 535 (1) (2004) 303 – 308, proceedings of the 10th International Vienna Conference on Instrumentation. [doi:10.1016/j.nima.2004.07.138](https://doi.org/10.1016/j.nima.2004.07.138).
- [39] M. Killenberg, S. Lotze, J. Mnich, A. Münnich, S. Roth, F. Sefkow, M. Tonutti, M. Weber, P. Wienemann, Charge transfer and charge broadening of GEM structures in high magnetic fields, Nuclear Instruments and Methods in Physics Research Section A: Accelerators, Spectrometers, Detectors and Associated Equipment 530 (3) (2004) 251 – 257. [doi:10.1016/j.nima.2004.04.241](https://doi.org/10.1016/j.nima.2004.04.241).
- [40] S. Bachmann, A. Bressan, L. Ropelewski, F. Sauli, A. Sharma, D. Mörmann, Charge amplification and transfer processes in the gas electron multiplier, Nuclear Instruments and Methods in Physics Research Section A Accelerators Spectrometers Detectors and Associated Equipment 438 (12 1999). [doi:10.1016/S0168-9002\(99\)00820-7](https://doi.org/10.1016/S0168-9002(99)00820-7).
- [41] P. Bhattacharya, B. Mohanty, S. Mukhopadhyay, N. Majumdar, H. Natal da Luz, 3D Simulation of Electron and Ion Transmission of GEM-based Detectors, Nuclear Instruments and Methods in Physics Research Section A: Accelerators, Spectrometers, Detectors and Associated Equipment 870 (07 2017). [doi:10.1016/j.nima.2017.06.054](https://doi.org/10.1016/j.nima.2017.06.054).
- [42] Y. Giomataris and Ph. Rebourgeard and J.P. Robert and G. Charpak, MICROMEGAS: a high-granularity position-sensitive gaseous detector for high particle-flux environments, Nuclear Instruments and Methods in Physics Research Section A: Accelerators, Spectrometers, Detectors and Associated Equipment 376 (1) (1996) 29 – 35. [doi:10.1016/0168-9002\(96\)00175-1](https://doi.org/10.1016/0168-9002(96)00175-1).
- [43] F. Sauli, A. Sharma, MICROPATTERN GASEOUS DETECTORS, Annual Review of Nuclear and Particle Science 49 (1) (1999) 341–388. [doi:10.1146/annurev.nucl.49.1.341](https://doi.org/10.1146/annurev.nucl.49.1.341).
- [44] J. N. Marx, D. R. Nygren, The Time Projection Chamber, Phys. Today 31N10 (1978) 46–53. [doi:10.1063/1.2994775](https://doi.org/10.1063/1.2994775).
- [45] M. Gai, M. Ahmed, S. Stave, W. Zimmerman, A. Breskin, B. Bromberger, et al., An Optical Readout TPC (O-TPC) for studies in nuclear astrophysics with gamma-ray

- beams at HI $\gamma$ S, *Journal of Instrumentation* 5 (01 2011). [doi:10.1088/1748-0221/5/12/P12004](https://doi.org/10.1088/1748-0221/5/12/P12004).
- [46] E. Aprile, J. Aalbers, F. Agostini, M. Alfonsi, F. D. Amaro, M. Anthony, B. Antunes, F. Arneodo, M. Balata, et al., The XENON1T dark matter experiment, *The European Physical Journal C* 77 (12) (Dec 2017). [doi:10.1140/epjc/s10052-017-5326-3](https://doi.org/10.1140/epjc/s10052-017-5326-3).
- [47] C. E. Aalseth, F. Acerbi, P. Agnes, I. F. M. Albuquerque, T. Alexander, A. Alici, A. K. Alton, P. Antonioli, S. Arcelli, R. Ardito, et al., DarkSide-20k: A 20 tonne two-phase LAr TPC for direct dark matter detection at LNGS, *The European Physical Journal Plus* 133 (3) (Mar 2018). [doi:10.1140/epjp/i2018-11973-4](https://doi.org/10.1140/epjp/i2018-11973-4).
- [48] D. Akerib, et al., The Large Underground Xenon (LUX) Experiment, *Nucl. Instrum. Meth. A* 704 (2013) 111–126. [arXiv:1211.3788](https://arxiv.org/abs/1211.3788), [doi:10.1016/j.nima.2012.11.135](https://doi.org/10.1016/j.nima.2012.11.135).
- [49] J. Alme, Y. Andres, H. Appelshäuser, S. Bablok, N. Bialas, R. Bolgen, U. Bonnes, R. Bramm, P. Braun-Munzinger, R. Campagnolo, et al., The ALICE TPC, a large 3-dimensional tracking device with fast readout for ultra-high multiplicity events, *Nuclear Instruments and Methods in Physics Research Section A: Accelerators, Spectrometers, Detectors and Associated Equipment* 622 (1) (2010) 316–367. [doi:10.1016/j.nima.2010.04.042](https://doi.org/10.1016/j.nima.2010.04.042).
- [50] N. Ishida, J. Kikuchi, T. Doke, M. Kase, Fano factor in xenon, *Phys. Rev. A* 46 (1992) 1676–1679. [doi:10.1103/PhysRevA.46.1676](https://doi.org/10.1103/PhysRevA.46.1676).
- [51] D. F. Bartlett, A. L. Duncan, J. R. Elliott, Afterpulses in a photomultiplier tube poisoned with helium, *Review of Scientific Instruments* 52 (2) (1981) 265–267. [doi:10.1063/1.1136585](https://doi.org/10.1063/1.1136585).
- [52] D. Ferenc, D. F. Šegedin, I. F. Šegedin, M. Šegedin Ferenc, Helium Migration through Photomultiplier Tubes - The Probable Cause of the DAMA Seasonal Variation Effect (2019). [arXiv:1901.02139](https://arxiv.org/abs/1901.02139).
- [53] E. W. McDaniel, *Atomic collisions: electron and photon projectiles*, Wiley, 1989.
- [54] Y. Kalkan, M. Arslanok, A. Cortez, Y. Kaya, İ. Tapan, R. Veenhof, Cluster ions in gas-based detectors, *Journal of Instrumentation* 10 (07) (2015) P07004–P07004. [doi:10.1088/1748-0221/10/07/p07004](https://doi.org/10.1088/1748-0221/10/07/p07004).
- [55] K. Hiraoka, G. Nakajima, S. Shoda, Determination of the stabilities of CO<sub>2</sub><sup>+</sup>(CO<sub>2</sub>)<sub>n</sub> and O<sub>2</sub><sup>+</sup>(CO<sub>2</sub>)<sub>n</sub> clusters with n=1–6, *Chemical Physics Letters* 146 (6) (1988) 535 – 538. [doi:10.1016/0009-2614\(88\)87495-5](https://doi.org/10.1016/0009-2614(88)87495-5).
- [56] A. Deisting, C. Garabatos, A. Szabo, Ion mobility measurements in Ar – CO<sub>2</sub>, Ne – CO<sub>2</sub>, and Ne – CO<sub>2</sub> – N<sub>2</sub> mixtures, and the effect of water contents, *Nucl. Instrum. Meth. A* 904 (2018) 1–8. [arXiv:1804.10288](https://arxiv.org/abs/1804.10288), [doi:10.1016/j.nima.2018.07.008](https://doi.org/10.1016/j.nima.2018.07.008).

- [57] Y. Kalkan, M. Arslanok, A. Cortez, Y. Kaya, I. Tapan, R. Veenhof, Cluster ions gas-based detectors, *Journal of Instrumentation* 10 (07 2015). [doi:10.1088/1748-0221/10/07/P07004](https://doi.org/10.1088/1748-0221/10/07/P07004).
- [58] G. A. Eiceman, Z. Karpas, H. H. Hill, *Ion mobility spectrometry*, CRC Press, Taylor & Francis Group, 2016.
- [59] E. McDaniel, J. Mitchell, M. Rudd, *Atomic collisions: Heavy-particle projectiles*, 1993.
- [60] Blanc, A., Recherches sur les mobilités des ions dans les gaz, *J. Phys. Theor. Appl.* 7 (1) (1908) 825–839. [doi:10.1051/jphysap:019080070082501](https://doi.org/10.1051/jphysap:019080070082501).
- [61] M. P. Dion, C. J. Martoff, M. Hosack, On the mechanism of Townsend avalanche for negative molecular ions, *Astroparticle Physics* 33 (4) (2010) 216–220. [doi:10.1016/j.astropartphys.2010.02.002](https://doi.org/10.1016/j.astropartphys.2010.02.002).
- [62] D. Snowden-Ifft, T. Ohnuki, E. Rykoff, C. Martoff, Neutron recoils in the DRIFT detector, *Nuclear Instruments & Methods in Physics Research Section A-accelerators Spectrometers Detectors and Associated Equipment - NUCL INSTRUM METH PHYS RES A* 498 (2003) 155–164. [doi:10.1016/S0168-9002\(02\)02120-4](https://doi.org/10.1016/S0168-9002(02)02120-4).
- [63] J. Miyamoto, I. Shipsey, C. Martoff, M. Katz-Hyman, R. Ayad, G. Bonvincini, A. Schreiner, GEM Operation in Negative Ion Drift Gas Mixtures, *Physics Research Publications* 526 (07 2004). [doi:10.1016/j.nima.2004.02.018](https://doi.org/10.1016/j.nima.2004.02.018).
- [64] I. Giomataris, R. Oliveira, S. Andriamonje, S. Aune, G. Charpak, et al., Micromegas in a Bulk, *Nuclear Instruments and Methods in Physics Research Section A Accelerators Spectrometers Detectors and Associated Equipment* 560 (01 2005). [doi:10.1016/j.nima.2005.12.222](https://doi.org/10.1016/j.nima.2005.12.222).
- [65] J. Battat, J. Brack, E. Daw, A. Dorofeev, A. Ezeribe, J.-L. Gauvreau, M. Gold, J. Harton, J. Landers, E. Law, E. Lee, D. Loomba, A. Lumnah, et al., First background-free limit from a directional dark matter experiment: Results from a fully fiducialised DRIFT detector, *Physics of the Dark Universe* 9-10 (2015) 1 – 7. [doi:10.1016/j.dark.2015.06.001](https://doi.org/10.1016/j.dark.2015.06.001).
- [66] W. P. Wood, J. Heicklen, Photooxidation of carbon disulfide, *The Journal of Physical Chemistry* 75 (7) (1971) 854–860. [doi:10.1021/j100677a002](https://doi.org/10.1021/j100677a002).
- [67] C. Dass, *Fundamentals of contemporary mass spectrometry*, Wiley-Interscience, 2007.
- [68] L. Christophorou, J. Olthoff, Electron Interactions With SF<sub>6</sub>, *Journal of Physical and Chemical Reference Data* 29 (05 2000). [doi:10.1063/1.1288407](https://doi.org/10.1063/1.1288407).
- [69] M. Santos, Development of a Dual-Polarity Ion Drift Chamber & Study of ion transport properties in gaseous mixtures of interest, Ph.D. thesis, University of Coimbra (2018).
- [70] P. Neves, Studies on the mobility of monoatomic and dimer noble gas ions in their parent gases., Ph.D. thesis, University of Coimbra (2009).

- [71] Xenon Flash Lamp, <https://www.hamamatsu.com/us/en/product/type/L2439/index.html>.
- [72] Ansys Maxwell: Low Frequency Electromagnetic Field Simulation, <https://www.ansys.com/products/electronics/ansys-maxwell>.
- [73] 3D CAD Design Software, SOLIDWORKS, <https://www.solidworks.com/>.
- [74] P. Kumpiranon, K. Kulasri, A. Rittirong, K. Saenboonruang, The current status of the Gas Electron Multiplier (GEM) research at Kasetsart University, Thailand, in: Journal of Physics: Conference Series, Vol. 860, 2017, p. 12019. doi:10.1088/1742-6596/860/1/012019.
- [75] A. Adeyeye, G. Shimon, Chapter 1 - Growth and Characterization of Magnetic Thin Film and Nanostructures, in: R. E. Camley, Z. Celinski, R. L. Stamps (Eds.), Magnetism of Surfaces, Interfaces, and Nanoscale Materials, Vol. 5 of Handbook of Surface Science, North-Holland, 2015, pp. 1 – 41. doi:10.1016/B978-0-444-62634-9.00001-1.
- [76] Y. Xie, H. Liu, A. Zhang, Y. Liu, T. Hu, L. Zhou, Z. An, X. Cai, J. Fang, et al., Quantum efficiency measurement of CsI photocathodes using synchrotron radiation at BSR, Nuclear Instruments and Methods in Physics Research Section A: Accelerators, Spectrometers, Detectors and Associated Equipment 664 (1) (2012) 310 – 316. doi:10.1016/j.nima.2011.09.067.
- [77] W. Haynes, CRC Handbook of Chemistry and Physics, Vol. 94, 2012.
- [78] P. Redhead, The ultimate vacuum, Vacuum 53 (1) (1999) 137 – 149. doi:10.1016/S0042-207X(98)00349-2.
- [79] A. Juarez, J. Urquijo, G. Hinojosa, J. Hernández-Ávila, E. Basurto, Relaxation effects in ionic mobility and cluster formation: Negative ions in SF<sub>6</sub> at high pressures, Plasma Sources Science & Technology - PLASMA SOURCES SCI TECHNOL 19 (06 2010). doi:10.1088/0963-0252/19/3/034005.
- [80] D. Marques, A. Cortez, J. Escada, R. Veenhof, P. Neves, C. Conde, F. Santos, F. Borges, Experimental ion mobility measurements in Ne-CF<sub>4</sub>, Journal of Instrumentation 14 (2019) P04015–P04015. doi:10.1088/1748-0221/14/04/P04015.
- [81] E. R. Fisher, M. E. Weber, P. B. Armentrout, Dissociative charge transfer reactions of Ar<sup>+</sup>, Ne<sup>+</sup>, and He<sup>+</sup> with CF<sub>4</sub> from thermal to 50 eV, The Journal of Chemical Physics 92 (4) (1990) 2296–2302. doi:10.1063/1.457969.
- [82] K. Brand, H. Jungblut, The interaction potentials of SF<sub>6</sub> ions in SF<sub>6</sub> parent gas determined from mobility data, Chemical Physics - CHEM PHYS 78 (1983) 1999–2007. doi:10.1063/1.444946.
- [83] J. Urquijo-Carmona, I. Alvarez, H. Martínez, C. Cisneros, Mobility and longitudinal diffusion of SF<sub>5</sub><sup>−</sup> and SF<sub>6</sub><sup>−</sup> in SF<sub>6</sub>, Journal of Physics D: Applied Physics 24 (2000) 664. doi:10.1088/0022-3727/24/5/004.



## BIBLIOGRAPHY

---

- [84] E. Baracchini, G. Cavoto, G. Mazzitelli, F. Murtas, F. Renga, S. Tomassini, Negative ion Time Projection Chamber operation with SF<sub>6</sub> at nearly atmospheric pressure, *Journal of Instrumentation* 13 (2017). [doi:10.1088/1748-0221/13/04/P04022](https://doi.org/10.1088/1748-0221/13/04/P04022).
- [85] Y. Nakamura, Transport coefficients of electrons and negative ions in SF<sub>6</sub>, *Journal of Physics D: Applied Physics* 21 (2000) 67. [doi:10.1088/0022-3727/21/1/010](https://doi.org/10.1088/0022-3727/21/1/010).
- [86] P. Patterson, Mobilities of Negative Ions in SF<sub>6</sub>, *The Journal of Chemical Physics* 53 (Jul 1970). [doi:10.1063/1.1674047](https://doi.org/10.1063/1.1674047).
- [87] Appendix III: Tables of Properties Useful in the Estimation of Ionneutral Interaction Energies, John Wiley & Sons, Ltd, 2005, pp. 531–539. [doi:10.1002/3527602852.app3](https://doi.org/10.1002/3527602852.app3).
- [88] J. D. Urquijo, F. B. Yousif, Negative ion motion in the mixtures of SF<sub>6</sub> with CF<sub>4</sub> and CH<sub>4</sub>-Ar, *Physical Review E* 68 (4) (2003). [doi:10.1103/physreve.68.046406](https://doi.org/10.1103/physreve.68.046406).
- [89] G. Hinojosa, J. D. Urquijo, Test of Blanc’s law for negative ion mobility in mixtures of SF<sub>6</sub> with N<sub>2</sub>, O<sub>2</sub> and air, *Journal of Physics D: Applied Physics* 36 (20) (2003) 2510–2514. [doi:10.1088/0022-3727/36/20/012](https://doi.org/10.1088/0022-3727/36/20/012).
- [90] I. Iga, M. Rao, S. Srivastava, J. Nogueira, Formation of negative ions by electron impact on SiF<sub>4</sub> and CF<sub>4</sub>, *Zeitschrift für Physik D Atoms, Molecules and Clusters* 24 (02 1992). [doi:10.1007/BF01426694](https://doi.org/10.1007/BF01426694).